

**SIMULATION-DERIVED NEUTRON SCATTERING
FOR LIPID MEMBRANES**

by

Mitchell Dorrell

A dissertation submitted to the Faculty of the University of Delaware in partial fulfillment of the requirements for the degree of Doctor of Philosophy in Physics

Summer 2020

© 2020 Mitchell Dorrell
All Rights Reserved

**SIMULATION-DERIVED NEUTRON SCATTERING
FOR LIPID MEMBRANES**

by

Mitchell Dorrell

Approved: _____

Edmund R. Nowak, Ph.D.

Chair of the Department of Physics and Astronomy

Approved: _____

John Pelesko, Ph.D.

Dean of the College of Arts and Sciences

Approved: _____

Douglas J. Doren, Ph.D.

Interim Vice Provost for Graduate and Professional Education and
Dean of the Graduate College

I certify that I have read this dissertation and that in my opinion it meets the academic and professional standard required by the University as a dissertation for the degree of Doctor of Philosophy.

Signed: _____

Edward R. Lyman, Ph.D.
Professor in charge of dissertation

I certify that I have read this dissertation and that in my opinion it meets the academic and professional standard required by the University as a dissertation for the degree of Doctor of Philosophy.

Signed: _____

Alexander J. Sodt, Ph.D.
Professor in charge of dissertation

I certify that I have read this dissertation and that in my opinion it meets the academic and professional standard required by the University as a dissertation for the degree of Doctor of Philosophy.

Signed: _____

Norman Wagner, Ph.D.
Member of dissertation committee

I certify that I have read this dissertation and that in my opinion it meets the academic and professional standard required by the University as a dissertation for the degree of Doctor of Philosophy.

Signed: _____

Karl M. Unruh, Ph.D.
Member of dissertation committee

I certify that I have read this dissertation and that in my opinion it meets the academic and professional standard required by the University as a dissertation for the degree of Doctor of Philosophy.

Signed: _____

Sandeep Patel, Ph.D.

Member of dissertation committee

TABLE OF CONTENTS

| | |
|--|-------------|
| LIST OF FIGURES | viii |
| LIST OF TABLES | x |
| ABSTRACT | xi |
| Chapter | |
| 1 INTRODUCTION TO BILAYERS AND SIMULATIONS | 1 |
| 1.1 Cell membranes and lipid bilayers | 1 |
| 1.2 Molecular dynamics simulations | 6 |
| 1.3 Molecular simulation of lipid bilayers | 7 |
| 2 SCATTERING | 11 |
| 2.1 Neutron scattering basics | 14 |
| 2.2 Internal structure of an isolated system: the Debye scattering formula | 17 |
| 2.3 Internal structure of infinite, laterally averaged thin fluid sheet | 18 |
| 2.4 A discrepancy between particulate models and continuum models of particulate systems | 21 |
| 2.5 Comparing scattering from flat and spherical samples: the q dependence of the scattering intensity | 22 |
| 3 BEYOND LATERAL AVERAGING | 26 |
| 3.1 Full periodicity: the Dirac Brush method | 26 |
| 3.2 Mean-field treatment of long range structure: the PFFT method | 30 |
| 4 PROOF OF CONCEPT | 40 |
| 4.1 Construction of an example bilayer with lateral substructure | 40 |
| 4.2 Simulation parameters | 42 |
| 4.3 Results: PFFT and Dirac Brush methods predict the signature of nanoscopic heterogeneity | 43 |
| 4.4 Discussion | 48 |

| | |
|---|-----------|
| 5 A HYBRID CONTINUUM APPROACH TO SCATTERING OF CURVED MEMBRANES | 51 |
| 5.1 Introduction | 51 |
| 5.2 Methods | 56 |
| 5.2.1 Coarse-grain Martini modeling | 56 |
| 5.2.2 Material deformation of a planar scattering length density to model curvature | 60 |
| 5.2.3 Continuum modeling | 64 |
| 5.2.4 Evaluating $I(q)$ | 65 |
| 5.3 Results & Discussion | 66 |
| 5.3.1 Deformation of the small-vesicle leaflets | 66 |
| 5.3.2 Comparison of the continuum and coarse-grain modeled intensity | 68 |
| 5.4 Conclusions | 70 |
| 6 INDICATIONS OF NANOMETER-SCALE HETEROGENEITY IN LIQUID-ORDERED BILAYERS | 72 |
| 6.1 Introduction | 72 |
| 6.1.1 Low- q scattering is most sensitive to overall vesicle composition, which determines scattering contrast with solvent | 74 |
| 6.1.2 High- q scattering is most sensitive to transverse structure | 75 |
| 6.1.3 The lateral signal is small compared to that of transverse structure | 76 |
| 6.1.4 Precise modeling of both transverse and lateral scattering is critical | 76 |
| 6.2 Methods | 77 |
| 6.2.1 Deuteration scheme and composition selection | 77 |
| 6.2.2 All-atom simulation | 82 |
| 6.3 Results: The SANS vesicle signal is reconstructed from combined molecular and continuum models | 82 |

| | | |
|----------|--|-----------|
| 6.4 | Intramolecular correlations of deuteration contribute to scattering | 85 |
| 6.4.1 | Experimental distributions of the L _o phase composition and size | 85 |
| 6.4.2 | The best-fit match to molecular simulation indicates nanometer-scale structure | 86 |
| 6.5 | Discussion and conclusions | 88 |
| 7 | CONCLUSION | 90 |
| 7.1 | Lateral scattering contributions to neutron scattering intensity | 90 |
| 7.2 | Adjusting for high curvature | 92 |
| 7.3 | Putting it together: searching for substructure | 93 |
| | BIBLIOGRAPHY | 96 |

LIST OF FIGURES

| | | |
|-----|---|----|
| 1.1 | Molecular Structure Diagrams for DSPC, DPPC, DOPC, and POPC | 2 |
| 1.2 | Molecular Structure Diagram for Cholesterol | 2 |
| 1.3 | Illustrative Phase Diagram for Mixtures of DSPC, DOPC, and Cholesterol | 4 |
| 1.4 | Martini Diagrams for DPPC, DOPC, and POPC | 9 |
| 1.5 | Hexagonal Substructure in the Liquid-Ordered Phase | 10 |
| 2.1 | Demonstration of the Influence of a Roughly Circular Lateral Inhomogeneity on a SANS Signal | 15 |
| 2.2 | Schematic of a SANS Experiment | 15 |
| 3.1 | Illustration of the Scattering Vectors that Satisfy the Constraints of the Dirac Comb Functions | 31 |
| 3.2 | Illustration of the PFFT Cutoff System | 35 |
| 4.1 | “Pseudo-Deuteriation” Patterns for Martini Simulations | 41 |
| 4.2 | Top Views of the Four Martini Systems | 44 |
| 4.3 | Scattering Intensity of the Inhomogeneous Systems, Using Lateral Averaging, the Dirac Brush Method, and the PFFT Method | 46 |
| 4.4 | Identification of Dirac Brush Spikes | 47 |
| 4.5 | Dependence of PFFT Scattering on Cutoff Cylinder Size | 49 |
| 5.1 | Rendering of Ca. 18 nm Diameter POPC/POPE MARTINI Vesicle | 58 |
| 5.2 | Illustration of MARTINI POPC/POPE with Bead Names | 59 |

| | | |
|-----|--|----|
| 5.3 | Illustration of Surface Continuum Model with Scattering Length Density Profile from Molecular Simulation | 61 |
| 5.4 | Geometric Area-Per-Lipids of Martini Sites | 67 |
| 5.5 | Scattering Intensity of a 13nm Diameter Vesicle Vs. the Hybrid Model | 69 |
| 5.6 | Scattering Intensity of an 18nm Diameter Vesicle Vs. the Hybrid Model | 69 |
| 6.1 | Small-Angle X-Ray Scattering Indicates the Boundary Between L_o and L_o/L_d Coexistence | 78 |
| 6.2 | SANS Compositions Used to Determine Optimal L_o Composition . . | 80 |
| 6.3 | Experimental SANS Intensities | 81 |
| 6.4 | Compositions Used for Compositional Fitting | 84 |
| 6.5 | Comparison of Experimental Scattering with PFFT and Lateral Averaging | 86 |
| 6.6 | Comparison of Experimental Liquid-Ordered Scattering with Single-Composition PFFT and Lateral Averaging | 87 |
| 6.7 | Comparison of Experimental Liquid-Ordered Scattering with Multi-Composition PFFT and Lateral Averaging | 87 |

LIST OF TABLES

| | | |
|-----|--|----|
| 4.1 | Martini Scattering Length Assignments | 43 |
| 6.1 | Compositions Used to Determine L_o Tie-Line Endpoint | 77 |
| 6.2 | SANS Compositions Used to Determine Optimal L_o Composition . | 81 |
| 6.3 | Compositions Used for Compositional Fitting | 83 |

ABSTRACT

The integration of molecular dynamics simulation and small-angle neutron scattering can yield new insights about molecular-scale structure within a system. Independently, scattering intensity data may be difficult to interpret, especially when multiple structures exist at similar lengthscales. For molecular dynamics, limited computational resources impose a tradeoff between parameterization accuracy, system dimensions, and simulation duration. The validation of simulations against experimental scattering intensities establishes the appropriateness of the tradeoffs, while simultaneously offering a visual and quantitative aid for interpreting the scattering intensity features. Existing tools computed the scattering intensity using only the transverse structure (i.e., normal to the bilayer surface) from the simulated membrane, but this is a poor approximation when the bilayer has significant lateral (in-plane) structure.

Presented are two new computational techniques to compute the small-angle neutron scattering intensity from a lipid bilayer molecular dynamics simulation. The first method, termed the “Dirac Brush”, computes the exact spectra including spurious artifacts from the simulation’s periodic boundary conditions. The second method, termed “PFFT”, applies a mean-field approximation beyond a tunable cutoff, avoiding the periodicity artifacts of the Dirac Brush. Both methods are validated using a set of coarse-grained molecular dynamics simulations to demonstrate sensitivity to contributions from lateral structure.

An additional technique is then presented to incorporate effects of curvature into the scattering intensity model. Curvature effects from both vesicle size and from dynamic fluctuations are modeled by geometrically deforming the transverse scattering length densities from a molecular dynamics simulation, and then mapping the new density profile over an arbitrary surface to model a larger vesicle. This new strategy

was again validated against coarse-grained molecular dynamics simulations full vesicles of two different sizes. A previously established construction method had been used to relax the tension in each leaflet, but the model fit indicated significant tension was still present in the outer leaflet. With the inclusion of the additional tension in the fit, the overall quality of the curvature model was exceptional.

Finally, the new techniques for modeling lateral contributions and curvature effects were combined to analyze the scattering intensity of vesicles with compositions exhibiting the liquid-ordered phase. Simulation had previously indicated that these compositions may exhibit nanoscale substructure consisting of hexagonally packed saturated lipid chains and cholesterol. PFFT was used to model the lateral scattering contributions, with the curvature effects included separately. The effect of vesicle-size polydispersity was also included in the model, and the overall fit to experimental scattering intensity was compared with and without the lateral contributions from PFFT. The fit with lateral contributions was superior to the fit without lateral contributions, suggesting that the simulation accurately represents the lateral structure within the membranes, confirming the presence of the hexagonally-packed nanoscale substructure.

Chapter 1

INTRODUCTION TO BILAYERS AND SIMULATIONS

1.1 Cell membranes and lipid bilayers

The cell is the fundamental unit of life. One of the most important components of all cells is the cell membrane, which serves as the functional boundary between the interior and exterior of the cell[1]. The cell membrane is directly involved with countless inter- and intracellular processes. For example, nutrients and waste must pass through the membrane on their ways into or out of the cell. Proteins attached to the cell membrane facilitate electrical and chemical communication between the cell and its environment. These processes depend on very specific physical and chemical properties of the membrane, which arise from molecular interactions within the membrane and thus directly rely on its composition.

The basis of the cell membrane is a lipid bilayer: two opposing layers of lipids. Lipids are a class of molecules with both hydrophilic regions and hydrophobic regions. Most membrane lipids are glycerophospholipids, each having a hydrophilic head group and two hydrophobic fatty acid tails. A glycerophospholipid typical of such membranes is palmitoyloleylphosphatidylcholine ([fig. 1.1d](#)), or POPC, in which one tail is an 18-carbon chain with one unsaturated bond, and the other is a fully-saturated 16-carbon chain. Others differ in their headgroup chemistry, the length of their carbon chains, and the number and positions of unsaturated bonds in those chains[2]. In addition to glycerophospholipids, cholesterol comprises 30 to 40 mol% of mammalian membranes, depending on cell type. Unlike glycerophospholipids which have hundreds of different combinations of heads and tails, cholesterol is a single molecule which consists of a chain of four hydrophobic carbon rings with a hydrophilic hydroxyl on one end and a hydrophobic fatty acid tail on the other ([fig. 1.2](#)).

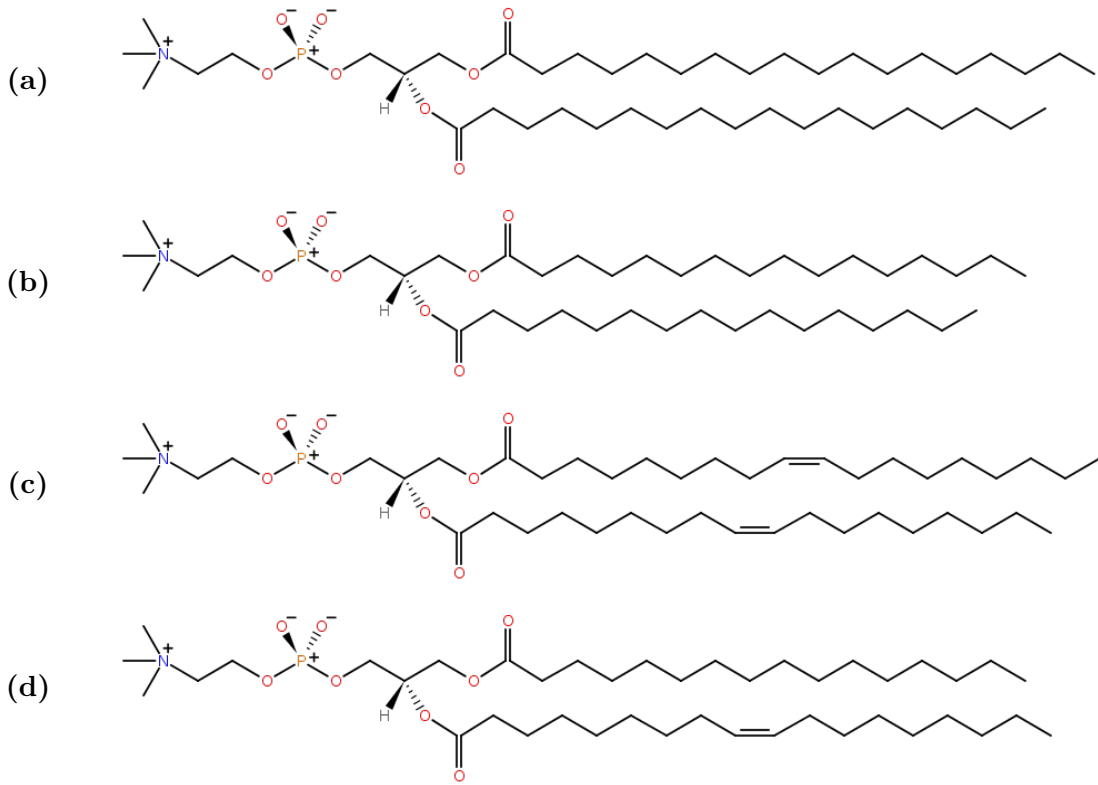


Figure 1.1: Molecular Structure Diagrams for DSPC (a), DPPC (b), DOPC (c), and POPC (d). All four lipids have the same hydrophilic head groups, but have different hydrophobic tails. DSPC has two saturated 18-carbon (stearoyl) tails, DPPC has two saturated 16-carbon (palmitoyl) tails, DOPC has two unsaturated 18-carbon (oleoyl) tails, and POPC has one palmitoyl and one oleoyl tail. Alternative head groups, chain lengths, and unsaturation patterns also exist.

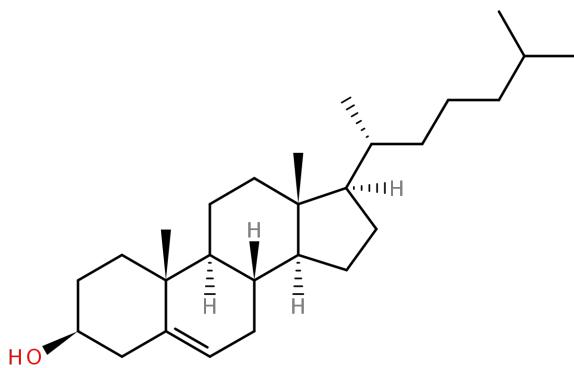


Figure 1.2: Molecular Structure Diagram for Cholesterol. The hydroxyl group is hydrophilic, while the carbon rings and side chain are hydrophobic.

The environment is aqueous both inside and outside the cell, so lipids naturally arrange themselves into a bilayer to shield their hydrophobic tails from the water. The bilayer consists of an inner leaflet and an outer leaflet; the lipids in the inner leaflet are aligned with their hydrophilic heads pointing toward the inside of the cell and the lipids in the outer leaflet are aligned with their heads pointing toward the outside of the cell. This arrangement confines the hydrophobic tails in the middle region between the head groups. Arranged like this, the lipid bilayer behaves like a two-dimensional fluid, with lipids freely flowing and redistributing within each leaflet. The hydrophobic and hydrophilic interactions are responsible for the bilayer's structural integrity, keeping the overall shape of the bilayer while simultaneously allowing the lipids to remain in a liquid state.

Biological membranes consist of hundreds of different kinds of lipids. The ratio of the different components varies from one type of cell to the next, making it very difficult to directly investigate how a membrane's overall physical properties relate to its composition. It is therefore common to use simplified compositions as models for more complex, physiological membranes[3]. Because up to 30 to 40 mol% of the composition of mammalian membranes is cholesterol, it is chosen as one component of the model. The huge diversity of glycerophospholipids is then simplified to two representative glycerophospholipids: one with saturated tails, and the other with unsaturated tails. These three components (cholesterol, the unsaturated lipid, and the saturated lipid) are then mixed in a variety of concentrations to explore the dependence of membrane properties on cholesterol and tail saturation.

When exploring mixtures of three components, it is helpful to indicate the composition on a ternary phase diagram. Ternary plots are triangular in shape and depict the composition space of ternary mixtures by assigning each mixture component to one corner of the triangle, as shown in [fig. 1.3](#). Suppose a ternary plot represents mixtures of components DSPC, DOPC, and cholesterol. DSPC (distearoylphosphatidylcholine, see [fig. 1.1a](#)) has two fully saturated 18-carbon chains and DOPC (dioleoylphosphatidylcholine, see [fig. 1.1c](#)) has two 18-carbon chains with one unsaturation each. The three

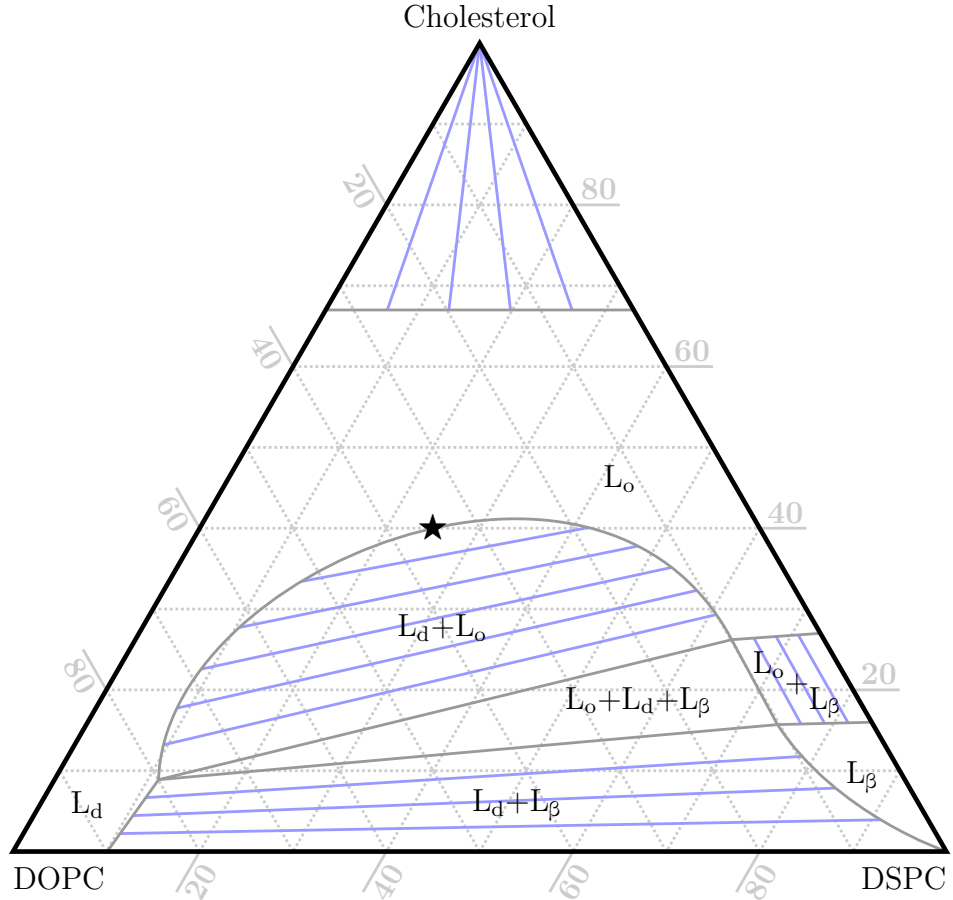


Figure 1.3: Illustrative Phase Diagram for Mixtures of DSPC, DOPC, and Cholesterol. Three distinct three-component phases are shown, L_o (liquid-ordered), L_d (liquid-disordered), and L_β (gel). There are five coexistence regions, one for each pair of three-component phases, one for coexistence between L_o/L_d and crystalline cholesterol, and one for three-phase coexistence of L_o , L_d , and L_β . The L_o and L_d phases become indistinguishable at concentrations exceeding approximately 40% cholesterol, resulting in a critical point (marked with a star). Adapted with permission from Ref. [4]. Copyright 2011 Cold Spring Harbor Laboratory Press.

corners represent pure samples of each component: 100% DOPC, 100% DSPC, or 100% cholesterol. Moving to the right along the bottom edge of the triangle from 100% DOPC toward 100% DSPC, the concentration of DOPC gradually decreases while the concentration of DSPC gradually increases. The three edges therefore represent binary mixtures of DOPC and DSPC at the bottom, DSPC and cholesterol at the right, and DOPC and cholesterol at the left, with the midpoint of each edge representing a 50%-50% mixture. Finally, the interior area of the triangle represents the ternary mixtures, which, like the edges, can be understood by a point's proximity to the three corners. A point in the center of the triangle represents an equal mixture of all three components. Proximity is considered using lines parallel to sides of the triangle, such that mixtures with 10% cholesterol fall on a straight line parallel to the DOPC-DSPC edge, and that line is positioned 10% of the distance from the DOPC-DSPC edge to the cholesterol corner.

A ternary model membrane mixture that has long been used as a standard consists of cholesterol, DOPC, and DPPC (dipalmitoylphosphatidylcholine, see [fig. 1.1b](#))^[5]. Functionally similar to DSPC, DPPC also has two fully saturated chains, but with 16 carbons in each as opposed to DSPC's 18. The ternary phase diagram for this three-component mixture has several distinct regions, depending on sample temperature. At room temperature, high concentrations of cholesterol solidify, as do high concentrations of DPPC. Perhaps counterintuitively, moderate mixtures of DPPC and cholesterol remain in the liquid phase. There is a liquid-solid coexistence region for certain mixtures with little cholesterol, but the region of the phase diagram that corresponds to physiological amounts of cholesterol is occupied by liquid states. These liquid states are studied using dyes that fluoresce at different wavelengths depending on the local environment^[6], or using spectroscopic methods like NMR that are sensitive to tail order^[7]. For this mixture, two distinct liquid states have been identified, along with a liquid-liquid coexistence region near the center of the phase diagram^[5, 4].

At compositions in the liquid-liquid coexistence region, the membrane will phase-separate into two regions of distinct compositions. The two distinct compositions

correspond to points on the edge of the two-phase coexistence region. If a line, known as a “tie-line”, is drawn between those two points (indicated in blue in [fig. 1.3](#)), membranes formed using mixtures along that line will exhibit phase separation into the same two phases, with different points on the line leading only to differences in the relative amounts of one phase compared to the other. If choosing a point within the two-phase coexistence region but not on the tie-line, the two resulting separated regions will have different compositions from the ones from on the tie-line. These phase compositions define a second tie-line, and thus the entire coexistence region is considered to consist of non-intersecting tie-lines.

The two phases (the endpoints of a tie-line) are called the liquid-ordered (L_o) and liquid-disordered (L_d) phases^[8, 9], named for the microscopic behavior of lipids in each phase. The liquid-ordered phase consists primarily of cholesterol and DPPC, while the liquid-disordered phase has higher concentrations of DOPC. In the liquid-ordered phase, lipids are closely packed, with the lipid tails aligning themselves into roughly parallel configurations. In the liquid-disordered phase, lipids are more loosely packed, with the lipid tails more randomly oriented and often transiently kinked. Furthermore, lipids diffuse more quickly in the liquid-disordered phase, and the liquid-disordered phase tends to have a thinner membrane thickness as well. A simpler example of demixing is demonstrated in [chapter 4](#), where a saturated (more ordered) lipid separates from an unsaturated (less ordered) lipid. The two resulting regions have contrasting physical characteristics which are analogous to liquid-ordered and liquid-disordered phases of ternary mixtures.

1.2 Molecular dynamics simulations

To further explore these phases, molecular dynamics simulations have been used to gain insights into microscopic lipid behavior and membrane structure. In such simulations, molecules are represented as their component atoms. An initial configuration is defined for the positions in 3D space of all atoms in both the molecules of interest and in any surrounding solvent. Each atom is assigned an initial velocity

sampled at random from the Boltzmann distribution of the chosen system temperature. Periodic boundary conditions are used to model an infinite 3D volume.

The motion of the atoms is discretized in time. The computer calculates the forces exerted by each atom onto the other atoms in the simulation, then integrates the classical equations of motion using a symplectic integrator to obtain the positions and velocities of every atom after each timestep. To retain numerical stability in the integration, the fastest vibrations in the system require a timestep not exceeding about two femtoseconds.

The forces between atoms are divided into bonded and non-bonded interactions. Non-bonded interactions include the Lennard-Jones potential and Coulombic (electrostatic) interactions. Bonded interactions are modeled using harmonic potentials for the distances between bonded atoms and for the angle between adjacent bonds. Torsional rotations around bonds (dihedrals) are modeled by trigonometric series with the symmetry appropriate for the molecular orbitals. Parameters for the interactions are compiled into forcefields, such as CHARMM[10], Amber[11], and GROMOS[12].

1.3 Molecular simulation of lipid bilayers

Lipid bilayer simulations started in the late 1980s[13] with the first simulations using more biologically relevant lipids published in the early 1990s[14]. Throughout the 1990s, simulation size and duration gradually increased, from tens of lipids for a few hundred picoseconds[15, 16] to over a thousand lipids for up to tens of nanoseconds[17]. Simulations including cholesterol arrived in the late 1990s[18], setting the stage for simulations of mixtures with more complex interactions[19].

Modern simulations of lipid bilayers contain a small membrane patch, typically 100-1000 square nanometers in size, with thousands of lipids and exceeding hundreds of thousands of atoms. With modern commodity supercomputers, typical simulations achieve durations of 1-10 microseconds. They also include a few nanometers of water above and below the membrane, and use periodic boundary conditions to model real membranes via an infinite bilayer sheet. Due to the inherent zero-curvature limitation

of the model, it most directly corresponds to real planar membranes and vesicles (i.e., spherical membranes without the rest of the cell) with low curvature.

Because simulations of large systems for long durations require significant computational resources, “coarse-grained” models are sometimes used; in “coarse-grained” models, the particle count is reduced by grouping several atoms into single interaction sites[20]. In the most popular such model (called “Martini”[21]), four heavy atoms are grouped into a single interaction site, reducing a lipid from about 130 atoms to about 12 coarse-grained sites, as shown in [fig. 1.4](#). This approximation greatly reduces the computational work (via particle count) and permits use of larger timesteps (by omitting the high-frequency vibrations of small atoms), allowing the simulation to run much faster. This makes larger and longer-duration simulations more practical.

Simulations of the liquid-disordered and liquid-ordered phases agree quantitatively with experimental measurements of lipid packing density and membrane thickness[22, 23]. However, simulations of the liquid-ordered phase revealed an additional new structural feature. When a leaflet is rendered using disks to represent the centers of mass of each tail and of cholesterol, large regions of transient hexagonal packing are observed (as shown in [fig. 1.5](#)). The composition of these hexagonally packed regions is almost exclusively DPPC, with DOPC and cholesterol existing in the interstitial regions between hexagonally packed clusters. The existence of the structure could have implications for the biological relevance of liquid-ordered compositions. Molecular dynamics simulations are inherently approximations of real experiments, so it is possible that the observed structure is an artifact of the simulation, but the accuracy of the simulations in other measurable quantities warrants investigation of this unexpected structure. The length scales of the structure are too small (10nm or less) for it to be observed using direct-imaging techniques, but they might be detected using scattering techniques.

However, extracting such short length scale, transient structure from the scattering data requires a new “integrated” analysis of the simulation and experimental data. The development, testing, and application of such an integrated method is the

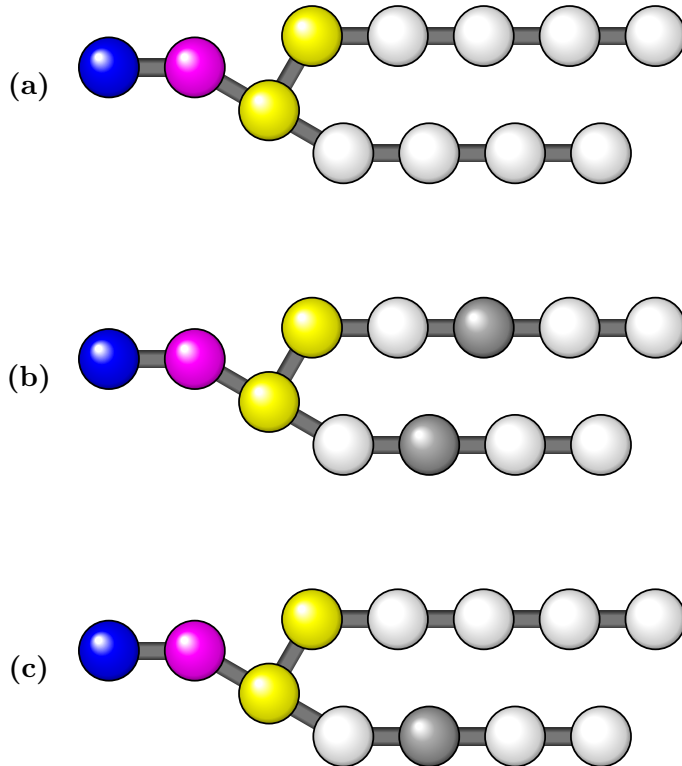


Figure 1.4: Martini Diagrams for DPPC (a), DOPC (b), and POPC (c). In the Martini coarse-grained model, the particle count is reduced by replacing groups of approximately four heavy (non-hydrogen) atoms with one Martini “bead”. Compare these models with the atomic structures in [fig. 1.1](#). The blue, magenta, and yellow beads represent choline, phosphate, and glycerol, respectively. White beads represent fully-saturated chains of four carbon atoms, and gray beads represent unsaturated chains of four carbon atoms. DSPC and DPPC differ only by two carbon atoms in the length of their lipid tails, which is below the resolution of Martini coarse-graining, so both lipids are represented by Martini DPPC (a).

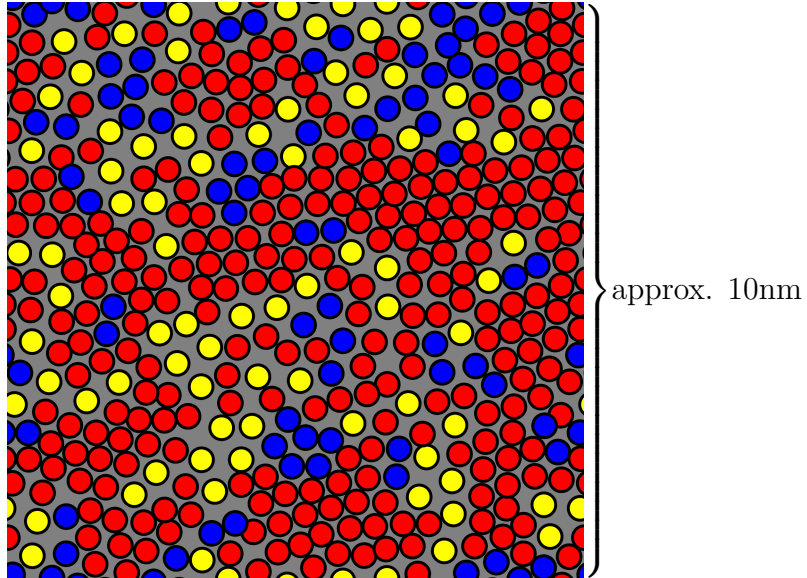


Figure 1.5: Hexagonal Substructure in the Liquid-Ordered Phase. Yellow disks represent the center of mass for Cholesterol. Red disks represent the center of mass of each DPPC tail chain, and blue disks represent the same for DOPC. Notice the large regions of hexagonally-packed red disks, such as in the upper right quadrant.

primary contribution of this work. An introduction to small-angle scattering is given in [chapter 2](#). Then two different approaches to the integrated analysis of molecular dynamics simulation and small-angle scattering are presented in [chapter 3](#): the “Dirac Brush” and “Particle Far-Field Transform (PFFT)” methods. [Chapter 4](#) presents the validation of both methods on simple lipid bilayer simulation data. [Chapter 5](#) investigates using planar molecular dynamics data to model neutron scattering intensities of curved systems, including vesicles, which may be too large to simulate directly. [Chapter 6](#) presents the application to a ternary lipid mixture alongside small-angle neutron scattering data for the same system. Finally, [chapter 7](#) provides a summary of the main results and an outlook.

Chapter 2

SCATTERING¹

Scattering of X-rays[25] and neutrons[26] have been used to determine the atomic and molecular structures of samples for over 100 years and for over 70 years, respectively. Scattering techniques resolve atomic and molecular spacings by aiming a collimated beam of radiation at a sample and collecting the scattered radiation in a two-dimensional detector. The detector converts the incident radiation into electrical impulses which are accumulated using computer software to render the scattering results.

When scattering from crystalline samples, the repeating pattern leads to very consistent separations between atoms, so the scattering measurement indicates those distances with the positions of sharp peaks in the scattered intensity[27]. A typical scattering measurement from a crystalline sample will yield a two-dimensional pattern of dots, each dot representing a peak at that distance in that direction. Patterns in the spacings between peaks can often be recognized as the signature of a specific crystal lattice, at which point measurements of the spacings can be used to determine the lattice constants.

The scattering behavior of crystals comes from the periodic structure, i.e. having a large number of consistently spaced atoms in consistent directions. If the crystals are ground into a powder, the microscopic atomic spacing is maintained, but the directions are randomized, leading to scattering results that look like concentric rings[27]. The spacing between rings correlates to the atomic spacing, but the random orientations of the crystals obscures the directional information. In this case, the results are angularly

¹ Adapted with permission from Ref. [24]. Copyright 2020 American Chemical Society.

averaged, and a one-dimensional chart of radiation intensity (measured radially from the center of the rings) is reported instead.

Soft matter samples and complex fluids lack the long-range order of traditional crystals, but still exhibit some regularity in their molecular structure. Compared to the repeating unit cells of a crystal, molecular structures such as protein complexes and lipidic heterogeneities exist at longer lengthscales and are consequently probed using scattering techniques with smaller deflections, called “small-angle scattering”.

For measuring the structure of membranes, small-angle scattering techniques using both X-rays and neutrons are particularly useful[28]. Small-angle X-ray scattering (SAXS) experiments utilize electromagnetic interactions between X-rays and the atomic electron clouds. Atoms with more electrons scatter more strongly than atoms with few electrons. In biological samples, the scattering signal from hydrogen is very weak compared to heavier atoms.

Small-angle neutron scattering (SANS) experiments utilize interactions between incoming neutrons and the atomic nuclei. The residual strong force is responsible for the nuclear reaction, making it difficult to predict the scattering behavior of a given atom[29]. However, the interactions are consistent and can be characterized using empirically-measured scattering lengths for each isotope. Notably, the scattering signal from lighter atoms is comparable to the scattering signal from heavier atoms, so hydrogens are much more visible than with X-ray scattering. Furthermore, different isotopes of the same element can have very different scattering behaviors. Isotope substitution grants the ability to tune the scattering properties of different parts of the sample without significantly impacting its chemical properties. For example, deuterium can be substituted for hydrogen, which is called “deuteration”. If the scattering properties are tuned such that two adjacent regions of the sample now have the same scattering behavior, the boundary between them becomes invisible to neutron scattering techniques. This is termed “contrast matching”[30] and can be used to make structural features more detectable by reducing the scattering signal from other structures.

In practice, X-ray scattering is much more accessible than neutron scattering. An

X-ray scattering experiment can be conducted using commercially available equipment from multiple vendors. Neutron scattering experiments require access to a neutron source such as a nuclear reactor or a spallation source. Furthermore, when the sample size is small enough to prevent multiple scattering (when an already-deflected wave encounters another nucleus in the sample and scatters a second time), the majority of neutrons pass through the sample without scattering at all. To collect sufficient scattering data, samples are often placed in the neutron beam for many hours, requiring careful scheduling of experiments to maximize beam utilization. In addition to the requirement of a neutron source, the scattering angles relevant to small-angle neutron scattering are shallow, which requires the detectors to be located a great distance away from the sample (up to 15.5 meters for the BIO-SANS instrument at Oak Ridge National Laboratory)[31] in order to achieve sufficient angular resolution. The equipment for neutron scattering experiments requires a relatively large amount of space, compared to X-ray scattering. Together, these factors make neutron scattering equipment much less prevalent in research facilities.

To investigate molecular structures embedded in a membrane, neutron scattering is chosen for its deuteration and contrast matching capabilities. For example, three distinct scattering regions can be enumerated for a membrane with two-phase coexistence: bulk solvent (typically water), the liquid-ordered region, and the liquid-disordered region. The two membrane regions are much more similar to each other than they are to the bulk solvent, but this is undesirable when the objective is to probe the existence and characteristics of the two phases. Through deuteration and contrast matching, the scattering behaviors of the various regions can be altered to optimize the scattering differences between the liquid-ordered and liquid-disordered regions while optionally minimizing the scattering differences between those membrane regions and the bulk solvent[32]. The ability to apply similar strategies to these and other types of membrane structures (aside from coexisting phases) makes small-angle neutron scattering the technique of choice for investigations of in-plane membrane structures, and the technique of focus for the remainder of this work, although the approaches presented are general

to X-ray scattering as well.

Figure 2.1 demonstrates the effect of lateral lipid inhomogeneity on a SANS signal (see chapter 4 for details). Viewed from above (in fig. 2.1a), the inhomogeneity has a lateral extent of approximately 6 nm. In fig. 2.1b, the SANS intensity is computed using two different methods. The first method (grey curve) is the traditional method used to model these systems, which is not sensitive to lateral structure. The second method (blue curve) is a new method, presented in section 3.2, which is sensitive to lateral structure, primarily manifesting it as the shallowing of the valley toward the left side of the graph.

2.1 Neutron scattering basics

Analytical models for the scattering intensity start with an idealized configuration for a SANS experiment, shown in fig. 2.2. The phase relevant to interference at the detector can be computed from two paths. First, from the neutron source to particle \mathbf{r}_1 the neutron accumulates phase $e^{i\mathbf{k}\cdot\mathbf{r}_1}$ before it scatters (relative to a particle at the origin). It then undergoes elastic scattering with the same magnitude of momentum, but in a new direction \mathbf{k}' , with $|\mathbf{k}'| = |\mathbf{k}|$. The scattered neutron travels to the detector, accumulating phase $e^{i\mathbf{k}'\cdot(\mathbf{r}_D - \mathbf{r}_1)}$. The scattering direction \mathbf{k}' is determined by where the neutron registers at the detector, \mathbf{r}_D , so this dependence will be notated using $\mathbf{k}'(\mathbf{r}_D)$. The reported scattering intensity depends only on the difference, $\mathbf{q} = \mathbf{k}'(\mathbf{r}_D) - \mathbf{k}$, and is represented by the symbol, $I(\mathbf{q})$.

The amplitude of the scattered wave depends on the identity of the particle from which it scattered. Each type of nucleus has an empirically measured scattering length, b , and these scattering lengths are tabulated for different isotopes of each element[33]. The behavior of each incident neutron scattering off an atom is dependent upon the internal state of the atom's nucleus. Since these states are not correlated between atoms, this leads to an incoherent contribution to the scattering intensity. This work considers only the coherent scattering contribution, in which each atom's scattering behavior is averaged over its nuclear states and represented by a single (scalar) scattering

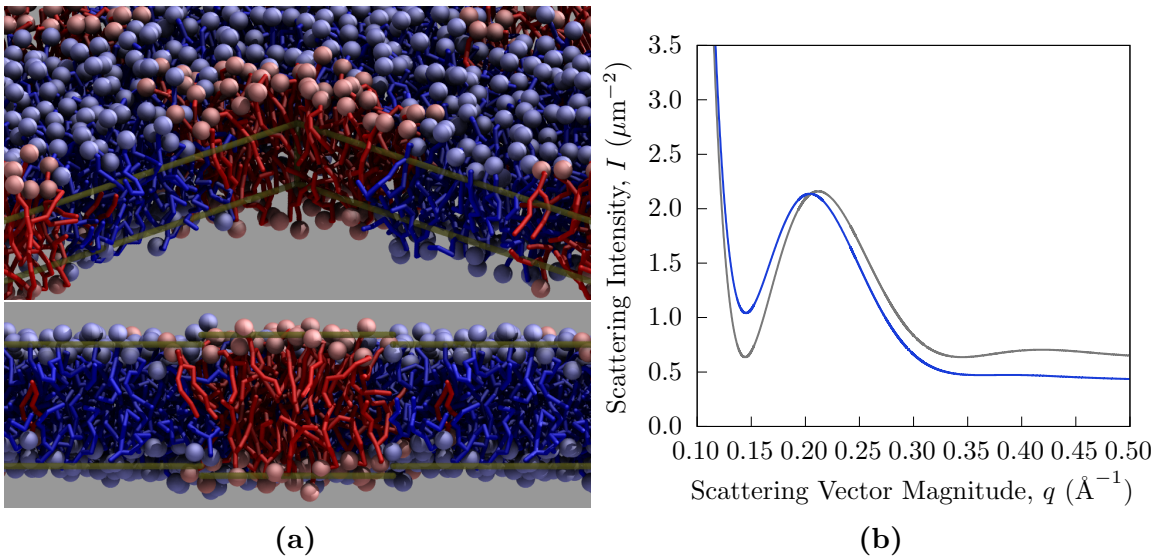


Figure 2.1: Demonstration of the Influence of a Roughly Circular Lateral Inhomogeneity on a SANS Signal. The interior structure of the lipid bilayer is shown from two perspectives (a), by first hiding the foreground quadrant and second by cross-section. DFPC lipids are shown in blue, while DPPC lipids are shown in red. Transparent gold lines indicate edges of the hidden quadrant in the first view, and illustrate the bilayer thickness variation in the second view. The SANS intensities (b) computed by lateral averaging (grey) and a new method (blue), presented in section 3.2, are compared to show the effect of lateral structure, in which the intensity near $q = 0.14\text{\AA}^{-1}$ is increased relative to higher q .

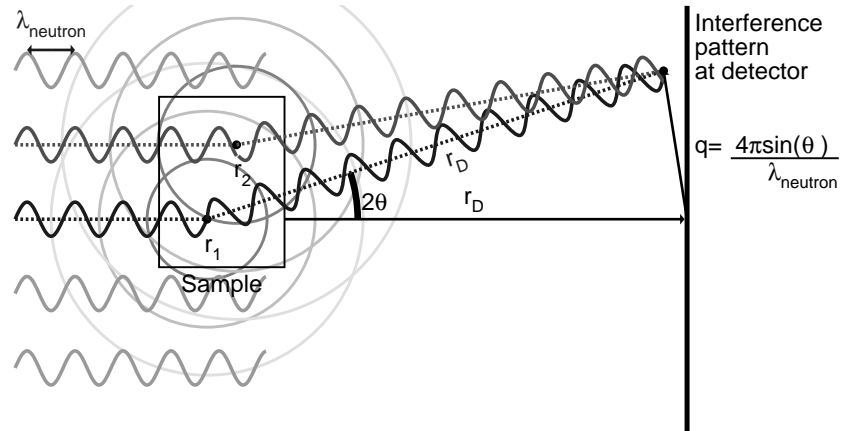


Figure 2.2: Schematic of a SANS Experiment. Not shown is the possibility of the sign of the scattered wave flipping by 180 degrees due to scattering (e.g., in the case of hydrogen).

length, termed the “coherent” scattering length. While classical scattering (e.g. hard sphere scattering) uses scattering lengths which represent physical dimensions of the scattering elements, and thus are always positive, neutron scattering lengths are abstract mathematical quantities which may be negative. A negative neutron scattering length indicates an inverted phase for the scattered neutron wave.

The scattering observed from a typical sample is the sum of the waves scattered from each atom in the sample. The contribution from each atom, i , at a point on the detector, \mathbf{r}_D , can be written as $\psi_i(\mathbf{r}_D)$, expressed in terms of the scattering length and the accumulated phase:

$$\psi_i(\mathbf{r}_D) = b_i e^{i\mathbf{k} \cdot \mathbf{r}_i} e^{i\mathbf{k}'(\mathbf{r}_D) \cdot (\mathbf{r}_D - \mathbf{r}_i)}. \quad (2.1)$$

The total amplitude, $\psi(\mathbf{r}_D)$, is then given by the sum over the atoms in the sample,

$$\psi(\mathbf{r}_D) = e^{i\mathbf{k}'(\mathbf{r}_D) \cdot \mathbf{r}_D} \sum_i b_i e^{-i(\mathbf{k}'(\mathbf{r}_D) - \mathbf{k}) \cdot \mathbf{r}_i}. \quad (2.2)$$

The measurable quantity is the intensity, or the absolute square of the total amplitude, which removes the dependence on the distance to the detector (recall that \mathbf{k}' only depends upon the direction of \mathbf{r}_D , not its magnitude):

$$I(\mathbf{r}_D) = \left| \sum_i b_i e^{-i(\mathbf{k}'(\mathbf{r}_D) - \mathbf{k}) \cdot \mathbf{r}_i} \right|^2. \quad (2.3)$$

For brevity, this is then re-expressed in terms of the scattering vector, \mathbf{q} ,

$$I(\mathbf{q}) = \left| \sum_i b_i e^{-i\mathbf{q} \cdot \mathbf{r}_i} \right|^2, \quad (2.4)$$

where each \mathbf{q} maps to a unique point on the detector, \mathbf{r}_D .

The intensity of the scattered signal is described by [eq. \(2.4\)](#). When generalized to a continuum model, the scattering length is replaced with a scattering length density, β , and the summed contributions from all points in the sample are then represented by an integral, as shown in [eq. \(2.5\)](#):

$$I(\mathbf{q}) = \left| \int d^3\mathbf{r} \beta(\mathbf{r}) e^{-i\mathbf{q} \cdot \mathbf{r}} \right|^2, \quad (2.5)$$

where the particulate form can be recovered using the $\beta(\mathbf{r})$ relation in eq. (2.6):

$$\beta(\mathbf{r}) = \sum_i b_i \delta(\mathbf{r} - \mathbf{r}_i). \quad (2.6)$$

The absolute squares of the particulate and continuum models can be expanded as

$$I(\mathbf{q}) = \sum_{i,j} b_i b_j e^{-i\mathbf{q}\cdot(\mathbf{r}_j - \mathbf{r}_i)}, \quad (2.7)$$

and

$$I(\mathbf{q}) = \int d^3\mathbf{r}_1 \int d^3\mathbf{r}_2 \beta(\mathbf{r}_1) \beta(\mathbf{r}_2) e^{-i\mathbf{q}\cdot(\mathbf{r}_2 - \mathbf{r}_1)}, \quad (2.8)$$

respectively. Both forms will be used in later derivations in this work.

2.2 Internal structure of an isolated system: the Debye scattering formula

The orientationally averaged scattering of a single molecular configuration of a finite system can be computed using the Debye scattering formula. Replacing $(\mathbf{r}_j - \mathbf{r}_i) = \mathbf{r}_{ij}$ in eq. (2.7) yields

$$I(\mathbf{q}) = \sum_{i,j} b_i b_j e^{-i\mathbf{q}\cdot\mathbf{r}_{ij}}. \quad (2.9)$$

Orientational averaging is performed by sweeping the scattering vector, \mathbf{q} , over the spherical polar angles, θ and ϕ . Each term in the summation can be integrated independently, so the coordinate system can be independently chosen for each term such that \mathbf{r}_{ij} always coincides with the pole, where $\phi = 0$. The angle between \mathbf{q} and \mathbf{r}_{ij} is then the polar angle, ϕ , and therefore $\mathbf{q} \cdot \mathbf{r}_{ij} = qr_{ij} \cos(\phi)$. Integrating the solid angle over the sphere yields the orientationally averaged scattering intensity, $I_\Omega(q)$:

$$\begin{aligned} I_\Omega(q) &= \sum_{i,j} b_i b_j \frac{1}{4\pi} \int_0^{2\pi} d\theta \int_0^\pi d\phi \sin(\phi) e^{-iqr_{ij} \cos(\phi)} \\ &= \sum_{i,j} b_i b_j \frac{\sin(qr_{ij})}{qr_{ij}}. \end{aligned} \quad (2.10)$$

An equivalent construction can be made using continuous scattering length density models, starting from eq. (2.8):

$$I_\Omega(q) = \int d^3\mathbf{r}_1 \int d^3\mathbf{r}_\Delta \beta(\mathbf{r}_1) \beta(\mathbf{r}_1 + \mathbf{r}_\Delta) \frac{\sin(q|\mathbf{r}_\Delta|)}{q|\mathbf{r}_\Delta|}, \quad (2.11)$$

where $\mathbf{r}_\Delta = \mathbf{r}_2 - \mathbf{r}_1$.

2.3 Internal structure of infinite, laterally averaged thin fluid sheet

The scattering expressions described thus far have involved sums over the atoms in the sample and integrations over the sample volume. However, membranes in simulation exist as infinite sheets, extending infinitely in two dimensions through the use of periodic boundary conditions. Instead of seeking expressions for the absolute intensity (which would now be infinite), the objective for modeling an infinite system is to derive expressions for the intensity per unit area.

Rather than a discrete set of scatterers $\{b_i\}$, consider instead a density of scatterers that are laterally uniform but which vary along the z -axis; this is the model that underlies existing methods for interpreting the scattering intensity from lipid bilayers.

The laterally averaged density, $\beta_{\text{LA}}(z)$, is computed from a full 3D scattering length density as

$$\beta_{\text{LA}}(z) = \frac{1}{L_x L_y} \int_{-L_x/2}^{L_x/2} dx \int_{-L_y/2}^{L_y/2} dy \beta(\mathbf{r}), \quad (2.12)$$

where x , y , and z are the cartesian components of \mathbf{r} . This laterally averaged density can then be computed from a collection of discrete scatterers by using the $\beta(\mathbf{r})$ substitution from eq. (2.6):

$$\beta_{\text{LA}}(z) = \frac{1}{L_x L_y} \sum_i b_i \delta(z - z_i). \quad (2.13)$$

For an ensemble average, eq. (2.13) is equivalent to eq. (2.12). In computing the scattering intensity, the one-dimensional Fourier transform of $\beta_{\text{LA}}(z)$ is a useful intermediate quantity:

$$\tilde{\beta}_{\text{LA}}(q_z) = \int_{-\infty}^{\infty} dz' e^{-iq_z z'} \beta_{\text{LA}}(z'). \quad (2.14)$$

From this, the three-dimensional Fourier transform can be constructed as

$$\tilde{\beta}_{\text{LA}}(\mathbf{q}) = \int_{-L_x/2}^{L_x/2} dx' e^{-iq_x x'} \int_{-L_y/2}^{L_y/2} dy' e^{-iq_y y'} \tilde{\beta}_{\text{LA}}(q_z), \quad (2.15)$$

where $\tilde{\beta}_{\text{LA}}(q_z)$ is from eq. (2.14), and q_x , q_y , and q_z are the vector components of \mathbf{q} . The Fourier transforms in x' and y' are temporarily using finite bounds, but the infinite- L limit will be considered shortly. The x' and y' terms cannot be reduced directly to

Dirac delta functions (recall that these Fourier transforms will be squared before being orientationally averaged). Instead, their finite-bounded forms evaluate as,

$$\int_{-L/2}^{L/2} dr' e^{-qr'} = 2q^{-1} \sin(Lq/2), \quad (2.16)$$

which leads to a pre-orientationally-averaged scattering intensity of

$$I_{\text{LA}}(\mathbf{q}) = [2q_x^{-1} \sin(L_x q_x/2)]^2 [2q_y^{-1} \sin(L_y q_y/2)]^2 \left| \tilde{\beta}_{\text{LA}}(q_z) \right|^2. \quad (2.17)$$

In the $L \rightarrow \infty$ limit, the absolute intensity grows to infinity, so the intensity per unit area is considered in its place, indicated with a barred symbol as \bar{I} :

$$\bar{I}_{\text{LA}}(\mathbf{q}) = \lim_{\substack{L_x \rightarrow \infty \\ L_y \rightarrow \infty}} \frac{1}{L_x L_y} [2q_x^{-1} \sin(L_x q_x/2)]^2 [2q_y^{-1} \sin(L_y q_y/2)]^2 \left| \tilde{\beta}_{\text{LA}}(q_z) \right|^2. \quad (2.18)$$

Returning to the squared sinusoidal factors, their behavior can be understood by integrating them in the large- L limit against a well-behaved test function (defined and differentiable at zero),

$$\lim_{L \rightarrow \infty} \int_{-\infty}^{\infty} dq \frac{4 \sin^2(Lq/2)}{Lq^2} f(q) \quad (2.19)$$

In the region of the integration domain where $q \neq 0$, the L in the denominator brings the integrand to zero. Therefore, the integral can be constrained to an arbitrarily small region around $q = 0$ without changing its value:

$$\lim_{L \rightarrow \infty} \int_{-\delta}^{\delta} dq \frac{4 \sin^2(Lq/2)}{Lq^2} f(q). \quad (2.20)$$

In this domain, the value of the test function is limited to be within $\delta f'_{\max}$, where f'_{\max} is the maximum value of the derivative of $f(q)$ on the domain $|q| < \delta$. For any given test function, δ can be chosen small enough to bound the value of $f(q)$ within any arbitrarily small range around $f(0)$, therefore in this extremely limited domain, $f(q) \approx f(0)$ and can be treated as a constant. The rest of the integral evaluates to

$$\lim_{L \rightarrow \infty} 4f(0) \left(\text{Si}(L\delta) + \frac{\cos(L\delta) - 1}{L\delta} \right), \quad (2.21)$$

where $\text{Si}(q)$ is the Sine Integral, defined by $\text{Si}(q) = \int_0^q dq' \sin(q')/q'$, which converges to $\pi/2$ in the limit as q approaches infinity. The other term has a bounded numerator

and unbounded denominator, and thus does not contribute to the value of the integral. The final result is that integrating the square of the Fourier transform against a test function reveals a behavior similar to a Dirac delta function,

$$\lim_{L \rightarrow \infty} \int_{-\infty}^{\infty} dq \frac{4 \sin^2(Lq/2)}{Lq^2} f(q) = 2\pi f(0), \quad (2.22)$$

therefore, in the context of orientational averaging, the following substitution will be made:

$$\lim_{L \rightarrow \infty} \frac{1}{L} [2q^{-1} \sin(Lq/2)]^2 = 2\pi\delta(q), \quad (2.23)$$

leading to a pre-orientationally-averaged intensity expression of

$$\bar{I}_{\text{LA}}(\mathbf{q}) = [2\pi\delta(q_x)][2\pi\delta(q_y)] \left| \tilde{\beta}_{\text{LA}}(q_z) \right|^2. \quad (2.24)$$

The intensity can then be orientationally averaged by computing

$$\bar{I}_{\text{LA},\Omega}(q) = \frac{1}{4\pi} \int d\Omega [2\pi\delta(q'_x)][2\pi\delta(q'_y)] |\tilde{\beta}_{\text{LA}}(q'_z)|^2, \quad (2.25)$$

where q'_x , q'_y and q'_z are primed because as dummy integration variables they are not explicitly components of \mathbf{q} as would be consistent with the notation throughout this work. The integral can be directly evaluated by mapping each hemisphere of radius q onto the q_x - q_y plane and integrating over a disk of radius q instead:

$$\begin{aligned} \bar{I}_{\text{LA},\Omega}(q) &= \frac{1}{4\pi q^2} \int_{-q}^q dq'_x \int_{-\sqrt{q^2 - q'^2}}^{\sqrt{q^2 - q'^2}} dq'_y \frac{q[2\pi\delta(q'_x)][2\pi\delta(q'_y)]}{\sqrt{q^2 - q'^2 - q'^2}} |\tilde{\beta}_{\text{LA}}(+\sqrt{q^2 - q'^2 - q'^2})|^2 \\ &\quad + \frac{1}{4\pi q^2} \int_{-q}^q dq'_x \int_{-\sqrt{q^2 - q'^2}}^{\sqrt{q^2 - q'^2}} dq'_y \frac{q[2\pi\delta(q'_x)][2\pi\delta(q'_y)]}{\sqrt{q^2 - q'^2 - q'^2}} |\tilde{\beta}_{\text{LA}}(-\sqrt{q^2 - q'^2 - q'^2})|^2, \end{aligned} \quad (2.26)$$

where the additional $1/q^2$ accounts the change from averaging over a unit sphere to averaging over a sphere of radius q , the factor of $q/\sqrt{q^2 - q'^2 - q'^2}$ is the Jacobian correcting for the ratio of areas between a differential area unit on the sphere and a differential area unit on the disk, and the positive and negative terms in the Fourier transform accomplish sampling both hemispheres. Since β_{LA} is real-valued, its Fourier

transform has the property $\tilde{\beta}_{\text{LA}}(-q) = \tilde{\beta}_{\text{LA}}^*(q)$, which indicates that $|\tilde{\beta}_{\text{LA}}(q)|$ is an even function, so the two terms are equivalent. Furthermore, the Dirac deltas choose the points where $q'_x = q'_y = 0$, thereby dramatically simplifying the expression:

$$\bar{I}_{\text{LA},\Omega}(q) = 2\pi q^{-2} |\tilde{\beta}_{\text{LA}}(q)|^2. \quad (2.27)$$

2.4 A discrepancy between particulate models and continuum models of particulate systems

There is a critical distinction between a scattering length density continuum (represented by $\beta(\mathbf{r})$) and a scattering length density continuum approximation of an atomic system. The difference becomes important due to the definition of the coherent scattering intensity, which implicitly includes the fictitious scattering of a particle with itself (notice that the $i = j$ case is not excluded from eq. (2.7)). In the case of a particle scattering with itself, the internal nuclear state will always correlate with itself, so a different scattering length should be used (known as the “incoherent scattering length”). For comparison to experiments, the definition of the incoherent scattering intensity normally compensates for this when it is summed with the coherent contribution.

Consider an ensemble average of scattering intensities of randomly distributed particles with no spatial correlations. The random phases from each $i \neq j$ term in eq. (2.7) will destructively interfere, averaging to zero for all $q > 0$. The $i = j$ terms will always add constructively, resulting in a q -independent background intensity of $\sum_i b_i^2$. When using a continuum model, the scattering intensity can be constructed from eqs. (2.16) and (2.23), which leads to a scattering intensity of $(2\pi)^3 V \delta(\mathbf{q})$, where V is the volume of the sample (in the large volume limit). The Dirac delta brings the scattering intensity of the continuum to zero for all $q > 0$, which contradicts the $\sum_i b_i^2$ result for atomic scattering.

To rectify this discrepancy, the self-scattering contribution must be separately added to a continuum-model intensity for comparison to atomic systems. As an example,

the corrected scattering intensity of a laterally averaged model is

$$\bar{I}_{\text{LA},\Omega}(q) = 2\pi q^{-2} |\tilde{\beta}_{\text{LA}}(q)|^2 + \frac{1}{L_x L_y} \sum_i b_i^2, \quad (2.28)$$

where the summation is over each atom in the atomic system represented by the continuum approximation, and $L_x L_y$ is the projected area of the atomic system into the x - y plane.

2.5 Comparing scattering from flat and spherical samples: the q dependence of the scattering intensity

At low q , $\tilde{\beta}_{\text{LA}}(q)$ in eq. (2.27) can be replaced by the scattering length per unit area, \bar{b} , that is, a two dimensional approximation. At low q , the scattering of a vesicle will reflect its shape (radius), precluding a direct comparison between the planar and spherical geometries. Rather, the scattered intensity can only be compared at q values where both systems can be considered planar. While the primary goal of this work is to model the orientationally averaged three-dimensional scattering intensity, an approximation has recently been proposed relating the in-plane (two dimensional) scattering of spherical and planar systems[34]. The relations below briefly describe the form of scattering from a thin sphere at low q to establish the regime where planar and spherical systems can be compared.

SANS experiments of lipid membranes are usually applied to a sample of vesicles of a given radius, R . Consider a spherical shell of thickness ϵ with uniform scattering length density \bar{b}/ϵ . To compute the SANS intensity, one must integrate over all scattering elements in the shell. This can be performed using eq. (2.5) in spherical polar coordinates, with the pole defined to be aligned with \mathbf{q} :

$$I(\mathbf{q}) = \left| \int_{R-\frac{\epsilon}{2}}^{R+\frac{\epsilon}{2}} dr \int_0^{2\pi} d\theta \int_0^\pi d\phi \left[\frac{\bar{b}}{\epsilon} e^{-iqr \cos(\phi)} r^2 \sin(\phi) \right] \right|^2 \quad (2.29)$$

$$= \left| \frac{4\pi \bar{b} R}{q} \left(\frac{\sin(q\epsilon/2)}{q\epsilon/2} \sin(qR) + \frac{1}{qR} \frac{\sin(q\epsilon/2)}{q\epsilon/2} \cos(qR) - \frac{1}{qR} \cos(q\epsilon/2) \cos(qR) \right) \right|^2, \quad (2.30)$$

where q is the magnitude of the scattering vector, \mathbf{q} .

The scattering intensity inevitably has strong features indicating the vesicle dimensions at q values near R^{-1} . To avoid the scattering contributions of the vesicle size, consider only $q \gg \frac{1}{R}$. These larger values of q correspond structural features short enough that the surface of the vesicle is approximately planar at these lengthscales. With $q \gg \frac{1}{R}$, the $\frac{1}{qR}$ factors make the second and third terms of eq. (2.30) negligible compared to the first term. With this approximation,

$$I(\mathbf{q}) = \left| \frac{4\pi\bar{b}R \sin(q\epsilon/2)}{q} \sin(qR) \right|^2. \quad (2.31)$$

Since there is no dependence on the direction of \mathbf{q} , this is also the orientationally averaged scattering intensity, which can then be divided by the area of the sphere to obtain the scattering intensity per unit area,

$$\bar{I}_\Omega(q) = \frac{4\pi\bar{b}^2}{q^2} \left(\frac{\sin(q\epsilon/2)}{q\epsilon/2} \right)^2 \sin^2(qR). \quad (2.32)$$

The intensity in eq. (2.32) oscillates rapidly, with period $\frac{\pi}{R}$. For a sample of normally distributed vesicle sizes with variance $\sigma^2 \ll R^2$, the intensity can be approximated by

$$\bar{I}_\Omega(q) = \int_{-\infty}^{\infty} dr \frac{4\pi\bar{b}^2}{q^2} \left(\frac{\sin(q\epsilon/2)}{q\epsilon/2} \right)^2 \sin^2(qr) \frac{1}{\sqrt{2\pi\sigma^2}} e^{-\frac{1}{2}(r-R)^2/\sigma^2}, \quad (2.33)$$

which evaluates to

$$\bar{I}_\Omega(q) = \frac{2\pi\bar{b}^2}{q^2} \left(\frac{\sin(q\epsilon/2)}{q\epsilon/2} \right)^2 \left(1 - \cos(2qR)e^{-2q^2\sigma^2} \right). \quad (2.34)$$

The second term in this expression rapidly approaches zero for $\sigma \gg \frac{1}{q}$, so for a sufficiently broad distribution of vesicle sizes, the oscillations in q will average out and the intensity converges to

$$\bar{I}_\Omega(q) = \frac{2\pi\bar{b}^2}{q^2} \left(\frac{\sin(q\epsilon/2)}{q\epsilon/2} \right)^2. \quad (2.35)$$

Compare this to the planar case. Based on the result from eq. (2.27),

$$\bar{I}_{\text{LA},\Omega}(q) = 2\pi q^{-2} |\tilde{\beta}_{\text{LA}}(q)|^2, \quad (\text{eq. (2.27), revisited})$$

the scattering intensity for a uniform slab can be computed directly, starting with $\tilde{\beta}_{\text{LA}}(q)$:

$$\tilde{\beta}_{\text{LA}}(q) = \int_{-\epsilon/2}^{\epsilon/2} dz' \left(\frac{\bar{b}}{\epsilon} \right) e^{-iqz'} = \frac{\bar{b} \sin(q\epsilon/2)}{q\epsilon/2}. \quad (2.36)$$

By inserting this into eq. (2.27), the expression agrees exactly with the $q \gg \frac{1}{R}$ approximation of the spherical shell:

$$\bar{I}_{\Omega,\text{planar}}(q) = \frac{2\pi\bar{b}^2}{q^2} \left(\frac{\sin(q\epsilon/2)}{q\epsilon/2} \right)^2. \quad (2.37)$$

This correspondence thus serves as a convenient normalization procedure for comparing planar simulations to experiments on large vesicles; for large enough values of q , where $q \gg \frac{1}{\sigma} \gg \frac{1}{R}$, planar membrane simulations and experiments on large vesicles (i.e., where $R \gg \sigma \gg \frac{1}{q}$) will have approximately equivalent scattering intensities. Additionally, if there is a regime where q is sufficiently large for the comparison, but still much less than $\frac{1}{\epsilon}$, then the scattering intensity takes a simpler form because $\frac{\sin(q\epsilon/2)}{q\epsilon/2}$ converges to unity,

$$\bar{I}_{\Omega}(q) = \frac{2\pi\bar{b}^2}{q^2}. \quad (2.38)$$

Since the scattering intensity in this range of q -values is proportional to q^{-2} and \bar{b}^2 , the scattering intensities (per unit area) of similar vesicle samples and planar models will match within this region, providing a useful reference quantity for normalization. The intensities of differing samples and/or models can be normalized by first weighting their intensities against \bar{b}^2 .

Note that it is the scattering length density per unit area, \bar{b} , that is taken into account in the case of a phase-separated mixture, as normalization depends on the scattering length density per unit area of the phases. For example, suppose a sample has vesicles with f_o area-percent L_o and f_d area-percent L_d . An independent simulation is run for each phase, where the averaged scattering length density per unit area of each composition is \bar{b}_o and \bar{b}_d , and the intensities predicted by each simulation are \bar{I}_o and \bar{I}_d . The normalized intensities for the two simulations would be \bar{I}_o/\bar{b}_o^2 and \bar{I}_d/\bar{b}_d^2 , which can be combined with the appropriate weights to simulate the mixture. For comparison to

the experimental result, the combination should be re-weighted with the combined \bar{b}_c , which will be $\bar{b}_o f_o + \bar{b}_d f_d$. The final expression for the combined intensity per unit area for comparison to a sample will be

$$\bar{I}_c = (\bar{b}_o f_o + \bar{b}_d f_d) \left(f_o \frac{\bar{I}_o}{\bar{b}_o^2} + f_d \frac{\bar{I}_d}{\bar{b}_d^2} \right). \quad (2.39)$$

Chapter 3

BEYOND LATERAL AVERAGING¹

There are two new methods that produce scattering intensities comparable to the methods described in Chapter 3. However, these new methods include contributions from lateral correlations. First, the Dirac Brush method models scattering by including the full periodicity of the simulated system. The scattering profile includes periodic artifacts that appear systematically in the scattered intensity. The derivation follows that in [section 2.3](#). Alternatively, the second method, PFFT, borrows the laterally averaged scattering length density only to model the scattering at long lengthscales, while using full 3D particle positions at short lengthscales; this is a mean-field approximation. Orientational averaging is accomplished by using the Debye scattering formula.

Source code for the PFFT and Dirac Brush methods is available on GitHub[[35](#)].

3.1 Full periodicity: the Dirac Brush method

The orientationally averaged scattering intensity of the simulated system, with its z images (above and below the bilayer) replaced by a uniform solvent density, can be computed exactly. The replacement of the z images with bulk solvent is handled first. A scattering length density with no spatial dependence can be freely added to or subtracted from the system $\beta(\mathbf{r})$ without affecting the scattering intensity, because the Fourier transform of the constant will only yield a Dirac delta function at $\mathbf{q} = 0$, which is not a point of interest. If the scattering length density of the bulk solvent, β_w , is subtracted from all space, the scattering length density in regions above and below the simulation box becomes exactly zero. The scattering amplitude of the volume

¹ Adapted with permission from Ref. [[24](#)]. Copyright 2020 American Chemical Society.

within the simulation box is calculated normally as given in [eq. \(2.4\)](#), but the scattering amplitude accounting for the absence of solvent in the simulation box must be integrated separately and subtracted:

$$\sum_i b_i e^{-\imath \mathbf{q} \cdot \mathbf{r}_i} - \beta_w \int_{-L_x/2}^{L_x/2} dx' e^{-\imath q_x x'} \int_{-L_y/2}^{L_y/2} dy' e^{-\imath q_y y'} \int_{-L_z/2}^{L_z/2} dz' e^{-\imath q_z z'}. \quad (3.1)$$

Each Fourier transform can be computed independently, which results in a solvent-compensated scattering intensity of

$$I_1(\mathbf{q}) = \left| \sum_i b_i e^{-\imath \mathbf{q} \cdot \mathbf{r}_i} - \frac{8\beta_w}{q_x q_y q_z} \sin(L_x q_x/2) \sin(L_y q_y/2) \sin(L_z q_z/2) \right|^2, \quad (3.2)$$

where the subscript in $I_1(\mathbf{q})$ indicates that this is the scattering intensity of a single image of the simulation box.

To find the scattering intensity for the infinite replicated system, consider “copying-and-pasting” the system boxes laterally, where the duplicated scatterers’ coordinates are shifted by \mathbf{r}_{rep} :

$$\beta(\mathbf{r}) = \sum_i b_i \delta(\mathbf{r} - \mathbf{r}_i) + \sum_i b_i \delta(\mathbf{r} - \mathbf{r}_i - \mathbf{r}_{\text{rep}}). \quad (3.3)$$

Each replicated simulation box contributes a phase term ($e^{-\imath \mathbf{q} \cdot \mathbf{r}_{\text{rep}}}$) according to the \mathbf{q} value under consideration:

$$\int d^3\mathbf{r} \beta(\mathbf{r}) e^{-\imath \mathbf{q} \cdot \mathbf{r}} = \sum_i b_i e^{-\imath \mathbf{q} \cdot \mathbf{r}_i} + \sum_i b_i e^{-\imath \mathbf{q} \cdot (\mathbf{r}_i + \mathbf{r}_{\text{rep}})}, = (1 + e^{-\imath \mathbf{q} \cdot \mathbf{r}_{\text{rep}}}) \sum_i b_i e^{-\imath \mathbf{q} \cdot \mathbf{r}_i}. \quad (3.4)$$

The sum of exponential terms can be reduced in closed form as a partial sum of a geometric series. For example, applying M replications along the positive x -axis and M replications along the negative x -axis, with a box width of L_x , yields:

$$e^{\imath M q_x L_x} + \dots + e^{\imath q_x L_x} + 1 + e^{-\imath q_x L_x} + \dots + e^{-\imath M q_x L_x} = \sum_{m=-M}^{+M} e^{-\imath m q_x L_x}, \quad (3.5)$$

$$= \frac{\sin((M + 1/2) q_x L_x)}{\sin(q_x L_x/2)}, \quad (3.6)$$

where q_x is the x component of \mathbf{q} . This factor is multiplied against the scattering amplitude of a single simulation box to represent the scattering amplitude of the

periodically replicated system. The scattering intensity, therefore, depends on the square of this factor, which can be understood using similar arguments to those used in the derivation of the laterally averaged intensity.

First, consider that since every term in [eq. \(3.5\)](#) is periodic, and since the period of each term is an integer division of $2\pi/L_x$, then the square of [eq. \(3.6\)](#) will also have period $2\pi/L_x$ (or an integer division thereof). A single period of the squared form can then be integrated against a well-behaved test function, mirroring the earlier derivation:

$$\lim_{M \rightarrow \infty} \left[\frac{1}{L_x(2M+1)} \int_{-\pi/L_x}^{\pi/L_x} dq \frac{\sin^2((M+1/2)q_x L_x)}{\sin^2(q_x L_x/2)} f(q) \right], \quad (3.7)$$

where the $1/L_x(2M+1)$ factor is introduced to incorporate the per-unit-area specification of the final intensity. Excluding the region where q is near zero, the squared sine function in the denominator will be positive and bounded. The squared sine function in the numerator is also bounded, implying that the value of the integral over portions of the domain excluding $q = 0$ will be finite. Finite values do not scale with M , so they do not contribute to the per-unit-area average. The next part of the derivation follows ??: the integration domain can be reduced to an arbitrarily small domain around $q = 0$, tightly constraining the value of the test function to $f(0)$. However, in this case, the rest of the integrand is not trivially integrated over this restricted domain. Since it has already been established that there are no contributions away from $q = 0$, the domain can be restored to the full period with test function evaluated as $f(0)$ outside of the integral:

$$\lim_{M \rightarrow \infty} \frac{f(0)}{L_x(2M+1)} \int_{-\pi/L_x}^{\pi/L_x} dq \frac{\sin^2((M+1/2)q_x L_x)}{\sin^2(q_x L_x/2)}. \quad (3.8)$$

This integral is most easily evaluated in a different form. Returning to [eq. \(3.5\)](#), the squared sum can be expanded as the product of two sums over m_1 and m_2 , which will yield $(2M+1)^2$ terms, but which can be recollected and summed from the minimum combination, $m_1 + m_2 = -2M$, to the maximum combination, $m_1 + m_2 = 2M$:

$$\sum_{m_1=-M}^{+M} e^{-im_1 q_x L_x} \sum_{m_2=-M}^{+M} e^{-im_2 q_x L_x} = \sum_{m=-2M}^{+2M} (2M+1-|m|) e^{-im q_x L_x}, \quad (3.9)$$

where $2M + 1 - |m|$ counts the number of terms with $m_1 + m_2 = m$. With the $m = 0$ term considered separately, the negative m values and the positive m values can be paired, which differ only in the sign of the exponent,

$$(2M + 1 - 0)e^{-\imath(0)q_x L_x} + \sum_{m=1}^{2M} (2M + 1 - m)(e^{-\imath mq_x L_x} + e^{\imath mq_x L_x}), \quad (3.10)$$

and this can then be simplified into a trigonometric form, which recall is still equivalent to the square of [eq. \(3.6\)](#):

$$\frac{\sin^2((M + 1/2)q_x L_x)}{\sin^2(q_x L_x / 2)} = 2M + 1 + 2 \sum_{m=1}^{2M} (2M + 1 - m) \cos(mq_x L_x). \quad (3.11)$$

This new form can be inserted into the [eq. \(3.8\)](#) and integrated trivially:

$$\begin{aligned} & \lim_{M \rightarrow \infty} \frac{f(0)}{L_x(2M + 1)} \int_{-\pi/L_x}^{\pi/L_x} dq \left[2M + 1 + 2 \sum_{m=1}^{2M} (2M + 1 - m) \cos(mq_x L_x) \right] \\ &= \lim_{M \rightarrow \infty} \frac{f(0)}{L_x(2M + 1)} \left[\frac{2\pi}{L_x}(2M + 1) + 2 \sum_{m=1}^{2M} (2M + 1 - m) \frac{2}{mL_x} \sin(m\pi) \right]. \end{aligned} \quad (3.12)$$

Since $\sin(m\pi) = 0$ for all integers m , all terms $m = 1$ through $m = 2M$ are zero, leaving just the $m = 0$ term to combine with the constants at the beginning of the expression,

$$\lim_{M \rightarrow \infty} \frac{f(0)}{L_x(2M + 1)} \left[\frac{2\pi}{L_x}(2M + 1) \right] = 2\pi L_x^{-2} f(0). \quad (3.13)$$

This exhibits Dirac-delta behavior again, except now this is part of a periodic function which repeats every $2\pi/L_x$. A periodic array of Dirac delta function is also known as a Dirac comb, $\text{III}_T(q)$, where T is the period between Dirac delta functions:

$$\lim_{M \rightarrow \infty} \frac{1}{L_x(2M + 1)} \left(\sum_{m=-M}^{+M} e^{-\imath mq_x L_x} \right)^2 = \frac{2\pi}{L_x^2} \text{III}_{2\pi/L_x}(q_x). \quad (3.14)$$

Here the comb selects wavevectors compatible with the periodicity of the simulation box, e.g. anywhere $q_x L_x$ is an integer multiple of 2π . For the two-dimensional replications which represent the entire infinite simulated system, an analogous factor is introduced for q_y . These factors are applied to the single-box scattering intensity, $I_1(\mathbf{q})$, to yield the full scattering intensity of the periodic simulation,

$$\bar{I}(\mathbf{q}) = \frac{2\pi}{L_x^2} \frac{2\pi}{L_y^2} \text{III}_{2\pi/L_x}(q_x) \text{III}_{2\pi/L_y}(q_y) I_1(\mathbf{q}). \quad (3.15)$$

The orientational average is constructed as before, integrating over the projection of each hemisphere into the q_x - q_y plane, and takes the form

$$\bar{I}_\Omega(q) = \frac{1}{4\pi q^2} \int_{-q}^q dq'_x \int_{-\sqrt{q^2-q'^2}}^{\sqrt{q^2-q'^2}} dq'_y \frac{q \left[\frac{2\pi}{L_x^2} \text{III}_{\frac{2\pi}{L_x}}(q'_x) \right] \left[\frac{2\pi}{L_y^2} \text{III}_{\frac{2\pi}{L_y}}(q'_y) \right]}{\sqrt{q^2 - q'^2_x - q'^2_y}} (I_1(\mathbf{q}^+) + I_1(\mathbf{q}^-)), \quad (3.16)$$

where \mathbf{q}^\pm is used for brevity to indicate the vectors sampling the upper and lower hemispheres, having the components, $\{q'_x, q'_y, \pm\sqrt{q^2 - q'^2_x - q'^2_y}\}$.

The product of two Dirac combs in perpendicular dimensions yields a hairbrush-like two-dimensional array of Dirac delta functions, termed a “Dirac Brush”, and illustrated in [fig. 3.1](#). The integration over the Dirac brush is evaluated in a similar way to integration over a Dirac delta. The integration becomes a sum over the integrand evaluated at each point that satisfies the selection condition of the brush, resulting in

$$\bar{I}_\Omega(q) = \frac{\pi}{q L_x^2 L_y^2} \sum_{\left\{ q'_x, q'_y : \sqrt{q'^2_x + q'^2_y} < q, q'_x \in \frac{2\pi}{L_x} \mathbb{Z}, q'_y \in \frac{2\pi}{L_y} \mathbb{Z} \right\}} \frac{I_1(\mathbf{q}^+) + I_1(\mathbf{q}^-)}{\sqrt{q^2 - q'^2_x - q'^2_y}}, \quad (3.17)$$

where \mathbb{Z} is the set of all integers and hence $(2\pi/L_x)\mathbb{Z}$ is the set of all integer multiples of $2\pi/L_x$. With both the replications and the orientational average handled analytically, this expression is not computationally intensive to evaluate. The discontinuities in the scattering length density at the boundaries of the simulation cell are completely averted, although periodicity artifacts are introduced, as will be demonstrated in [chapter 4](#).

3.2 Mean-field treatment of long range structure: the PFFT method

Lateral averaging neglects all lateral correlations, while the Dirac Brush method exhaustively includes them, including the artificial long-range order resulting from periodic boundary conditions. A typical modeling target of a simulation will have short-ranged order, but the finite size of the simulation precludes long-ranged correlations from being accessible to the model. While periodic boundary conditions effectively avoid short-range consequences of finite simulation sizes, their use does not (and is not

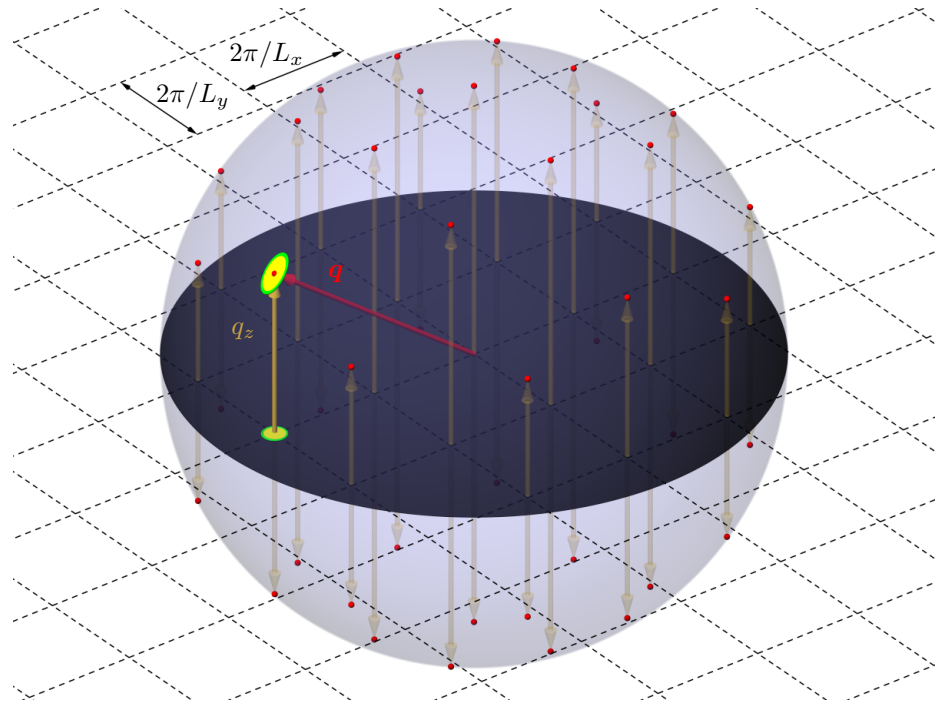


Figure 3.1: Illustration of the $\{q_x, q_y, q_z\}$ Scattering Vectors, with Magnitude $|\mathbf{q}|$, that Satisfy the Constraints of the q_x and q_y Dirac Comb Functions. The grid lines cutting through the middle of the sphere at $q_z = 0$ show the values of q_x or q_y selected by the respective Dirac comb functions. The intersection of q_x and q_y grid lines are the points for which both comb functions are satisfied. Projecting each point vertically up or down onto the sphere of radius q provides the value of q_z . Additionally, the ratio between the area of the yellow disk on the sphere to the area of the yellow disk on in the q_x - q_y plane is given by q/q_z , illustrating the source of the Jacobian used in [eqs. \(2.26\)](#) and [\(3.16\)](#).

meant to) accurately model long-range properties. Our Particle Far-Field Transform technique, or PFFT, bridges the gap between lateral averaging and the Dirac Brush method by employing a mean-field model for far-field correlations.

The scattering intensity represents correlations of scattering length density that are described by:

$$I_\Omega(q) = \int d^3\mathbf{r}_1 \int d^3\mathbf{r}_\Delta \beta(\mathbf{r}_1)\beta(\mathbf{r}_1 + \mathbf{r}_\Delta) \frac{\sin(q|\mathbf{r}_\Delta|)}{q|\mathbf{r}_\Delta|} \quad (\text{eq. (2.11), revisited})$$

Instead of squaring the Fourier transform (e.g., [eq. \(2.4\)](#)), the PFFT method uses the Debye scattering formula ([eq. \(2.11\)](#)) that sums over pairs of scatterers. The fundamental concept behind PFFT is the decomposition of the $\beta(\mathbf{r}_1)\beta(\mathbf{r}_1 + \mathbf{r}_\Delta)$ products used to represent pairs of scatterers with either particle or continuum models. If the lateral distance between scattering elements is within a cutoff r_c , then the particulate model of the scattering length density is used ($\beta_{\text{part}}(\mathbf{r})$). The lateral cutoff forms a cylindrical region around each scattering element, with the cylinder oriented orthogonal to the plane of the bilayer. If, however, the lateral distance is greater than the cutoff (i.e., one scattering element is positioned outside of the other element's cylinder), then a laterally-averaged continuum model is used instead ($\beta_{\text{LA}}(z)$), thus preserving the transverse bilayer structure but omitting the undesirable long-range lateral structure. Additionally, the continuum model is convenient for other mathematical constructions where there is no lateral dependence, since it is equivalent to the particulate model in those circumstances.

Special consideration is necessary for the bulk solvent regions above and below the simulation box. Like before in [section 3.1](#), the direct approach is to assign the solvent scattering length density to the regions above and below of the simulation box. The solvent scattering length density can then be subtracted from all space without affecting the scattering intensity, which brings the scattering length density to zero above and below of the simulation box, while maintaining a smooth transition across box boundaries. Because the integrand is zero above and below of the simulation box, these regions can be excluded from the scattering integrals, simplifying the necessary

computations. The difference is in the lateral bounds of integration. In eq. (3.1), the lateral bounds were constrained to a single simulation box because replications accounted for the integration over the remainder of lateral space. In this case, mathematical replications are not being used, so the integration domain must initially extend to infinity in all lateral directions.

$$I_\Omega(q) = \int_{\substack{x_1 \in (-\infty, \infty) \\ y_1 \in (-\infty, \infty) \\ z_1 \in \text{box}}} d^3 \mathbf{r}_1 \int_{\substack{x_\Delta \in (-\infty, \infty) \\ y_\Delta \in (-\infty, \infty) \\ z_1 + z_\Delta \in \text{box}}} d^3 \mathbf{r}_\Delta (\beta(\mathbf{r}_1) - \beta_w)(\beta(\mathbf{r}_1 + \mathbf{r}_\Delta) - \beta_w) \frac{\sin(q|\mathbf{r}_\Delta|)}{q|\mathbf{r}_\Delta|} \quad (3.18)$$

Furthermore, because the simulated system is periodic in the x and y directions, each box contributes equally to the total scattering. The averaged scattering intensity *per unit area* can be expressed by constraining one of the integration domains to a single box and weighting by $L_x L_y$, the area of the box. However, the second integration domain must remain infinite, because the pairwise scattering contributions between different boxes on the periodic lattice are not identical.

With these considerations, the scattering integral can be rewritten as:

$$\bar{I}_\Omega(q) = \frac{1}{L_x L_y} \int_{\mathbf{r}_1 \in \text{box}} d^3 \mathbf{r}_1 \int_{\substack{x_\Delta \in (-\infty, \infty) \\ y_\Delta \in (-\infty, \infty) \\ z_1 + z_\Delta \in \text{box}}} d^3 \mathbf{r}_\Delta (\beta(\mathbf{r}_1) - \beta_w)(\beta(\mathbf{r}_1 + \mathbf{r}_\Delta) - \beta_w) \frac{\sin(q|\mathbf{r}_\Delta|)}{q|\mathbf{r}_\Delta|}. \quad (3.19)$$

Moreover, the cross-terms are expanded and handled separately as:

$$\begin{aligned} \bar{I}_\Omega(q) = & \frac{1}{L_x L_y} \int_{\mathbf{r}_1 \in \text{box}} d^3 \mathbf{r}_1 \int_{\substack{x_\Delta \in (-\infty, \infty) \\ y_\Delta \in (-\infty, \infty) \\ z_1 + z_\Delta \in \text{box}}} d^3 \mathbf{r}_\Delta \left(\underbrace{\beta(\mathbf{r}_1)\beta(\mathbf{r}_1 + \mathbf{r}_\Delta)}_{\mathbf{I}} - \right. \\ & \left. \underbrace{\beta_w \beta(\mathbf{r}_1)}_{\mathbf{II}} - \underbrace{\beta_w \beta(\mathbf{r}_1 + \mathbf{r}_\Delta)}_{\mathbf{III}} + \underbrace{\beta_w^2}_{\mathbf{IV}} \right) \frac{\sin(q|\mathbf{r}_\Delta|)}{q|\mathbf{r}_\Delta|}. \end{aligned} \quad (3.20)$$

Each term corresponds to a specific correlation between two regions.

- **I** Correlations between a single simulation box and the infinite bilayer model (both particulate and continuum models contribute to this term).

- **II** Correlations between a single simulation box and the infinite solvent background.
- **III** Correlations between a single box of solvent background and the infinite bilayer model.
- **IV** Correlations between a single box of solvent background and the infinite solvent background.

Term **I** is further split into terms **Ia** and **Ib**, as illustrated in [fig. 3.2](#), where the domain of the \mathbf{r}_Δ integral is divided into two regions. Term **Ia** covers the region where \mathbf{r}_Δ is within the cylindrical cutoff, where particulate representations are used for the short-range correlations, and Term **Ib** covers the region where \mathbf{r}_Δ is outside of the cylindrical cutoff, where the continuum representation is used. The full scattering intensity calculation is performed by computing the contributions from each of the five terms (**Ia**, **Ib**, **II**, **III**, and **IV**) independently and summing them.

Starting with term **Ia**, the particulate form given by [eq. \(2.6\)](#) is substituted for both scattering length density factors:

$$\bar{I}_\Omega^{\text{Ia}}(q) = \frac{1}{L_x L_y} \int_{\mathbf{r}_1 \in \text{box}} d^3 \mathbf{r}_1 \int_{\substack{\mathbf{r}_\Delta \in \text{cyl} \\ z_1 + z_\Delta \in \text{box}}} d^3 \mathbf{r}_\Delta \sum_i b_i \delta(\mathbf{r}_1 - \mathbf{r}_i) \sum_j b_j \delta(\mathbf{r}_1 + \mathbf{r}_\Delta - \mathbf{r}_j) \frac{\sin(q|\mathbf{r}_\Delta|)}{q|\mathbf{r}_\Delta|}, \quad (3.21)$$

where both i and j iterate over all (infinitely many) atoms in the system, because the integration bounds are responsible for constraining them. When the integration over the Dirac delta functions is performed, the resulting sums are now constrained appropriately, yielding

$$\bar{I}_\Omega^{\text{Ia}}(q) = \frac{1}{L_x L_y} \sum_{i \in \text{box}} \sum_{j \in \text{cyl}} b_i b_j \frac{\sin(qr_{ij})}{qr_{ij}}, \quad (3.22)$$

where $r_{ij} = |\mathbf{r}_j - \mathbf{r}_i|$.

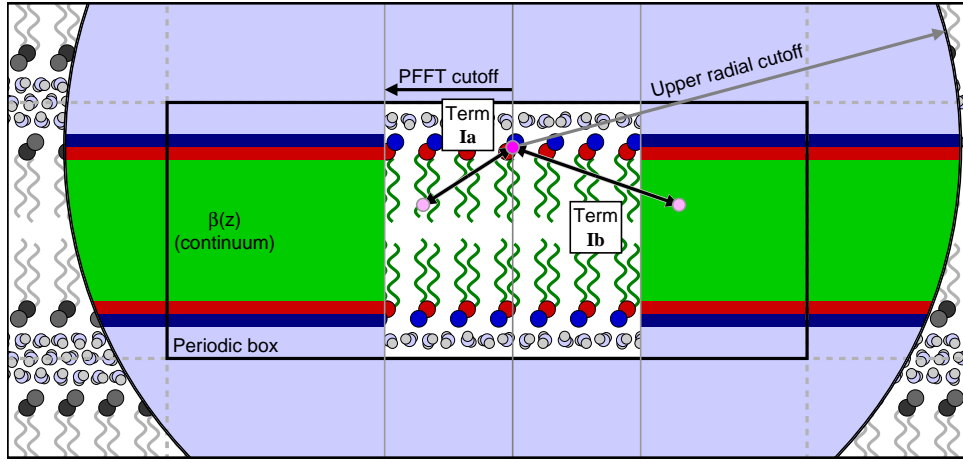


Figure 3.2: Illustration of the PFFT Cutoff System, Including the Terms **Ia** and **Ib**. When computing the scattering, every particle (for illustration purposes, one head group particle was arbitrarily chosen and marked with bright magenta) sees full particulate detail within a cylindrical region centered on its position, shown as a white rectangular region in the center of the figure. This region has a radius equal to the PFFT cutoff and vertically spans the entire simulation box (depicted as a black rectangle, labeled "Periodic box", with periodic image boundaries depicted by dotted grey lines). The **Ia** term represents the scattering between the selected particle (magenta) and the other particles (one illustrated in light pink, left of center) within the cylindrical region (central white rectangular region). Outside of this region, the particle sees only a laterally averaged continuum, illustrated as broad colored stripes. Term **Ib** represents the scattering between the selected particle and all of the volume elements of this continuum (also illustrated using a light pink dot, right of center). This process is iterated over all other particles in the simulation box. The spatial scattering length density correlations are used to numerically compute the weighted pair distribution function for all distances, up to some cutoff, depicted by the large black circle in the graphic.

Term **Ib** is more complex. The particulate form is retained for the $\beta(\mathbf{r}_1)$ factor, but the laterally-averaged continuum form is used for $\beta(\mathbf{r}_1 + \mathbf{r}_\Delta)$, now outside of the cutoff cylinder:

$$\bar{I}_\Omega^{\text{Ib}}(q) = \frac{1}{L_x L_y} \int_{\mathbf{r}_1 \in \text{box}} d^3 \mathbf{r}_1 \int_{\substack{\mathbf{r}_\Delta \notin \text{cyl} \\ z_1 + z_\Delta \in \text{box}}} d^3 \mathbf{r}_\Delta \sum_i b_i \delta(\mathbf{r}_1 - \mathbf{r}_i) \beta_{\text{LA}}(z_1 + z_\Delta) \frac{\sin(q|\mathbf{r}_\Delta|)}{q|\mathbf{r}_\Delta|}. \quad (3.23)$$

The Dirac delta function again resolves the \mathbf{r}_1 integral, and the \mathbf{r}_Δ integral is expressed in cylindrical polar coordinates ($\{s_\Delta, \theta_\Delta, z_\Delta\}$), yielding

$$\bar{I}_\Omega^{\text{Ib}}(q) = \frac{1}{L_x L_y} \sum_{i \in \text{box}} b_i \int_{r_c}^\infty ds_\Delta \int_0^{2\pi} d\theta_\Delta \int_{-\frac{L_z}{2} - z_i}^{\frac{L_z}{2} - z_i} dz_\Delta s_\Delta \beta_{\text{LA}}(z_i + z_\Delta) \frac{\sin(q\sqrt{s_\Delta^2 + z_\Delta^2})}{q\sqrt{s_\Delta^2 + z_\Delta^2}}, \quad (3.24)$$

for which the θ_Δ integral can be immediately evaluated. Next let $r_\Delta = \sqrt{s_\Delta^2 + z_\Delta^2}$ and isolate the r_Δ -dependent factor on the right:

$$\bar{I}_\Omega^{\text{Ib}}(q) = \frac{2\pi}{q L_x L_y} \sum_{i \in \text{box}} b_i \int_{-\frac{L_z}{2} - z_i}^{\frac{L_z}{2} - z_i} dz_\Delta \beta_{\text{LA}}(z_i + z_\Delta) \int_{\sqrt{r_c^2 + z_\Delta^2}}^\infty dr_\Delta \sin(qr_\Delta), \quad (3.25)$$

The r_Δ integral poses a problem. When implemented practically, numerical integration will be used to compute this term of the scattering intensity. However, the r_Δ integrand (a sine function) is highly oscillatory and does not converge to zero as r_Δ grows large, causing standard numerical integration techniques to fail.

The numerical integration problem can be avoided through Fourier manipulation. The sine function can be integrated from zero to infinity if interpreted as a Fourier transform:

$$\int_0^\infty dr_\Delta \sin(qr_\Delta) = \int_{-\infty}^\infty dr_\Delta H(r_\Delta) \sin(qr_\Delta) = -\Im \left[\int_{-\infty}^\infty dr_\Delta H(r_\Delta) e^{-iqr_\Delta} \right], \quad (3.26)$$

where $H(x)$ is the Heaviside step function (defined by $H(x) = \int_{-\infty}^x dt \delta(t)$, i.e., the integral of the Dirac delta function) and $\Im[x]$ is the imaginary component of x . Evaluated from the inside out, it becomes

$$-\Im \left[\int_{-\infty}^\infty dr_\Delta H(r_\Delta) e^{-iqr_\Delta} \right] = -\Im \left[\frac{1}{iq} + \pi\delta(q) \right] = \frac{1}{q}. \quad (3.27)$$

With this new relation, the oscillatory behavior of the $\sin(qr_\Delta)$ integrand can be handled gracefully. The lower bound of the original integration domain was $\sqrt{r_c^2 + z_\Delta^2}$, not zero, so that difference needs to be addressed by subtracting an integral over the domain from zero to $\sqrt{r_c^2 + z_\Delta^2}$. With this manipulation, the computable form of term **Ib** is given by,

$$\bar{I}_\Omega^{\text{Ib}}(q) = \frac{2\pi}{qL_xL_y} \sum_{i \in \text{box}} b_i \int_{-\frac{L_z}{2}-z_i}^{\frac{L_z}{2}-z_i} dz_\Delta \beta_{\text{LA}}(z_i + z_\Delta) \left[\frac{1}{q} - \int_0^{\sqrt{r_c^2 + z_\Delta^2}} dr_\Delta \sin(qr_\Delta) \right], \quad (3.28)$$

where the replacement r_Δ integral is now viable for numerical integration techniques.

The remaining three terms are more straightforward. Term **II** is the contribution to the scattering intensity from a single simulation box and the infinite (in the lateral dimensions) solvent background, given by eq. (3.29), and term **III** is the contribution from the infinite bilayer model and a single simulation box of solvent background, given by eq. (3.30),

$$\bar{I}_\Omega^{\text{II}}(q) = -\frac{1}{L_xL_y} \int_{\mathbf{r}_1 \in \text{box}} d^3\mathbf{r}_1 \int_{\substack{x_\Delta \in (-\infty, \infty) \\ y_\Delta \in (-\infty, \infty) \\ z_1 + z_\Delta \in \text{box}}} d^3\mathbf{r}_\Delta \beta_w \beta(\mathbf{r}_1) \frac{\sin(q|\mathbf{r}_\Delta|)}{q|\mathbf{r}_\Delta|}, \quad (3.29)$$

$$\bar{I}_\Omega^{\text{III}}(q) = -\frac{1}{L_xL_y} \int_{\mathbf{r}_1 \in \text{box}} d^3\mathbf{r}_1 \int_{\substack{x_\Delta \in (-\infty, \infty) \\ y_\Delta \in (-\infty, \infty) \\ z_1 + z_\Delta \in \text{box}}} d^3\mathbf{r}_\Delta \beta_w \beta(\mathbf{r}_1 + \mathbf{r}_\Delta) \frac{\sin(q|\mathbf{r}_\Delta|)}{q|\mathbf{r}_\Delta|}. \quad (3.30)$$

For both terms, the particulate form can be used to introduce Dirac delta functions which reduce one of the integrals to a sum:

$$\bar{I}_\Omega^{\text{II}}(q) = -\frac{1}{L_xL_y} \beta_w \sum_{i \in \text{box}} b_i \int_{\substack{x_\Delta \in (-\infty, \infty) \\ y_\Delta \in (-\infty, \infty) \\ z_i + z_\Delta \in \text{box}}} d^3\mathbf{r}_\Delta \frac{\sin(q|\mathbf{r}_\Delta|)}{q|\mathbf{r}_\Delta|}, \quad (3.31)$$

$$\bar{I}_\Omega^{\text{III}}(q) = -\frac{1}{L_xL_y} \beta_w \sum_j b_j \int_{\mathbf{r}_1 \in \text{box}} d^3\mathbf{r}_1 \frac{\sin(q|\mathbf{r}_j - \mathbf{r}_1|)}{q|\mathbf{r}_j - \mathbf{r}_1|}. \quad (3.32)$$

Let the $\mathbf{r}_{\Delta'}$ label be reused to represent $\mathbf{r}_1 - \mathbf{r}_j$ in term **III**,

$$\bar{I}_{\Omega}^{\text{II}}(q) = -\frac{1}{L_x L_y} \beta_w \sum_{i \in \text{box}} b_i \int_{\substack{x_{\Delta} \in (-\infty, \infty) \\ y_{\Delta} \in (-\infty, \infty) \\ z_i + z_{\Delta} \in \text{box}}} d^3 \mathbf{r}_{\Delta} \frac{\sin(q|\mathbf{r}_{\Delta}|)}{q|\mathbf{r}_{\Delta}|}, \quad (3.33)$$

$$\bar{I}_{\Omega}^{\text{III}}(q) = -\frac{1}{L_x L_y} \beta_w \sum_j b_j \int_{\mathbf{r}_j + \mathbf{r}_{\Delta'} \in \text{box}} d^3 \mathbf{r}_{\Delta'} \frac{\sin(q|\mathbf{r}_{\Delta'}|)}{q|\mathbf{r}_{\Delta'}|}, \quad (3.34)$$

and the only visible difference between the terms is that in term **II**, the integral domain includes the entire x - y plane, while in term **III**, it is the sum which spans the entire x - y plane. The unconstrained sum and integral can be re-expressed as sums over all periodic images of a single simulation box (or box of solvent).

$$\bar{I}_{\Omega}^{\text{II}}(q) = -\frac{1}{L_x L_y} \beta_w \sum_{i \in \text{box}} b_i \sum_{\text{rep}} \int_{\substack{x_i + x_{\Delta} \in \text{box} \\ y_i + y_{\Delta} \in \text{box} \\ z_i + z_{\Delta} \in \text{box}}} d^3 \mathbf{r}_{\Delta} \frac{\sin(q|\mathbf{r}_{\Delta} + \mathbf{r}_{\text{rep}}|)}{q|\mathbf{r}_{\Delta} + \mathbf{r}_{\text{rep}}|}, \quad (3.35)$$

$$\bar{I}_{\Omega}^{\text{III}}(q) = -\frac{1}{L_x L_y} \beta_w \sum_{\text{rep}} \sum_{j \in \text{box}} b_j \int_{(\mathbf{r}_j + \mathbf{r}_{\text{rep}}) + \mathbf{r}_{\Delta'} \in \text{box}} d^3 \mathbf{r}_{\Delta'} \frac{\sin(q|\mathbf{r}_{\Delta'}|)}{q|\mathbf{r}_{\Delta'}|}, \quad (3.36)$$

where \mathbf{r}_{rep} is the displacement vector between each image box and the reference box.

Defining $\mathbf{r}_{\Delta''} = \mathbf{r}_{\Delta} + \mathbf{r}_{\text{rep}}$ reveals that terms **II** and **III** are equivalent:

$$\bar{I}_{\Omega}^{\text{II}}(q) = -\frac{1}{L_x L_y} \beta_w \sum_{\text{rep}} \sum_{i \in \text{box}} b_i \int_{\mathbf{r}_i + (\mathbf{r}_{\Delta''} - \mathbf{r}_{\text{rep}}) \in \text{box}} d^3 \mathbf{r}_{\Delta''} \frac{\sin(q|\mathbf{r}_{\Delta''}|)}{q|\mathbf{r}_{\Delta''}|}, \quad (3.37)$$

$$\bar{I}_{\Omega}^{\text{III}}(q) = -\frac{1}{L_x L_y} \beta_w \sum_{\text{rep}} \sum_{j \in \text{box}} b_j \int_{(\mathbf{r}_j + \mathbf{r}_{\text{rep}}) + \mathbf{r}_{\Delta'} \in \text{box}} d^3 \mathbf{r}_{\Delta'} \frac{\sin(q|\mathbf{r}_{\Delta'}|)}{q|\mathbf{r}_{\Delta'}|}, \quad (3.38)$$

where the difference in sign on \mathbf{r}_{rep} is irrelevant because both directions are included in the sum anyway.

To evaluate them, it is worthwhile to return to eq. (3.33) and express the \mathbf{r}_{Δ} integral in cylindrical polar coordinates,

$$\bar{I}_{\Omega}^{\text{II}}(q) = \bar{I}_{\Omega}^{\text{III}}(q) = \frac{-1}{L_x L_y} \beta_w \sum_{i \in \text{box}} b_i \int_0^{2\pi} d\theta_{\Delta} \int_{-\frac{L_z}{2} - z_i}^{\frac{L_z}{2} - z_i} dz_{\Delta} \int_0^{\infty} ds_{\Delta} \frac{s_{\Delta} \sin(q\sqrt{s_{\Delta}^2 + z_{\Delta}^2})}{q\sqrt{s_{\Delta}^2 + z_{\Delta}^2}}, \quad (3.39)$$

and then, like in term **Ib**, substitute $r_\Delta = \sqrt{s_\Delta^2 + z_\Delta^2}$:

$$\bar{I}_\Omega^{\text{II}}(q) = \bar{I}_\Omega^{\text{III}}(q) = -\frac{1}{qL_xL_y}\beta_w \sum_{i \in \text{box}} b_i \int_0^{2\pi} d\theta_\Delta \int_{-\frac{L_z}{2}-z_i}^{\frac{L_z}{2}-z_i} dz_\Delta \int_0^\infty dr_\Delta \sin(qr_\Delta). \quad (3.40)$$

The r_Δ integral was evaluated while investigating term **Ib**, and the θ_Δ and z_Δ integrals are trivial as well. The final result for terms **II** and **III** is

$$\bar{I}_\Omega^{\text{II}}(q) = \bar{I}_\Omega^{\text{III}}(q) = -\frac{2\pi L_z}{q^2 L_x L_y} \beta_w \sum_{i \in \text{box}} b_i. \quad (3.41)$$

Finally, term **IV** is the contribution from a single box of solvent background scattering against the laterally infinite slab of solvent background.

$$\bar{I}_\Omega^{\text{IV}}(q) = \frac{1}{L_x L_y} \int_{\mathbf{r}_1 \in \text{box}} d^3 \mathbf{r}_1 \int_{\substack{x_\Delta \in (-\infty, \infty) \\ y_\Delta \in (-\infty, \infty) \\ z_1 + z_\Delta \in \text{box}}} d^3 \mathbf{r}_\Delta \beta_w^2 \frac{\sin(q|\mathbf{r}_\Delta|)}{q|\mathbf{r}_\Delta|} \quad (3.42)$$

The lateral dimensions of the \mathbf{r}_1 integral contribute a factor of $L_x L_y$, and in cylindrical polar coordinates, the θ_Δ integral contributes a factor of 2π ,

$$\bar{I}_\Omega^{\text{IV}}(q) = 2\pi \beta_w^2 \int_{-\frac{L_z}{2}}^{\frac{L_z}{2}} dz_1 \int_{-\frac{L_z}{2}-z_1}^{\frac{L_z}{2}-z_1} dz_\Delta \int_0^\infty ds_\Delta \frac{s_\Delta \sin(q\sqrt{s_\Delta^2 + z_\Delta^2})}{q\sqrt{s_\Delta^2 + z_\Delta^2}}, \quad (3.43)$$

and then with the same r_Δ substitution as before, the s_Δ integral can be evaluated, and then the z_Δ and z_1 integrals, which yields

$$\bar{I}_\Omega^{\text{IV}}(q) = \frac{2\pi L_z^2}{q^2} \beta_w^2. \quad (3.44)$$

The full scattering intensity per unit area is thus given by summing the terms computed above:

$$\begin{aligned} \bar{I}_\Omega(q) = & \frac{1}{L_x L_y} \sum_{i \in \text{box}} \sum_{j \in \text{cyl}} b_i b_j \frac{\sin(qr_{ij})}{qr_{ij}} + \\ & \frac{2\pi}{qL_x L_y} \sum_{i \in \text{box}} b_i \int_{-\frac{L_z}{2}-z_i}^{\frac{L_z}{2}-z_i} dz_\Delta \beta_{\text{LA}}(z_i + z_\Delta) \left[\frac{1}{q} - \int_0^{\sqrt{r_c^2 + z_\Delta^2}} dr_\Delta \sin(qr_\Delta) \right] + \\ & 2 \left(-\frac{2\pi L_z}{q^2 L_x L_y} \beta_w \sum_{i \in \text{box}} b_i \right) + \frac{2\pi L_z^2}{q^2} \beta_w^2. \end{aligned} \quad (3.45)$$

The inclusion of short-range particulate scattering captures local lateral structure, but the use of long-range continuum scattering prevents anomalous periodicity artifacts, as demonstrated using systems described in the following section.

Chapter 4

PROOF OF CONCEPT¹

4.1 Construction of an example bilayer with lateral substructure

There are well-studied lipid systems that have nanometer-scale substructure. For example, mixtures of DSPC, DOPC, POPC, and cholesterol (see [figs. 1.1](#) and [1.2](#)) exhibit nanometer-scale domains over specific compositional ranges[36]. Additionally, simulations indicate that the liquid-ordered phase has nanometer-scale substructure defined by the clustering of saturated lipid chains[22]. Both the Dirac Brush and PFFT methods are designed to predict the scattering signature of such nanoscopic lateral structure in lipid mixtures. To show how lateral correlations are captured by the Dirac Brush and the PFFT methods, a simple lipid mixture is first considered, with lateral structure that is amenable to the simulated lengthscale and for which the lengthscale of the lipid domain is easily tunable, e.g., by changing the mole fraction of each lipid type.

Lateral spatial correlations are indicated by deviation from the predicted scattering obtained through lateral averaging. However, even a single component fluid membrane still has nanoscale spatial correlations, such as from thickness fluctuations[37]. To control for these, and to demonstrate the scattering signature of lateral inhomogeneity most effectively, the bilayers simulated here each have nearly equivalent laterally averaged scattering profiles, $\beta(z)$. This is accomplished by using Martini[21] lipids with a variety of bonding structures for simulation but then by reassigning their neutron scattering lengths to make them equivalent for scattering purposes (see [fig. 4.1](#)). To control for differing natural areas-per-lipid that would affect neutron scattering length

¹ Adapted with permission from Ref. [24]. Copyright 2020 American Chemical Society.

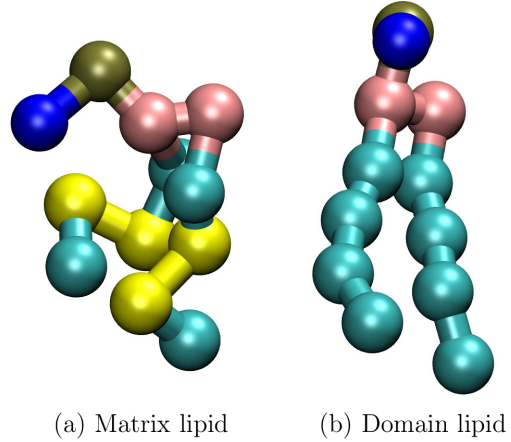


Figure 4.1: “Pseudo-Deuteration” Patterns for Martini Simulations. Yellow Martini “beads” are assigned scattering length 4.152 fm, while cyan tail beads are assigned -3.332 fm, providing contrast between the matrix and domain lipids. Choline (blue), phosphate (gold), and glycerol (pink) are assigned scattering lengths of -5.158 fm, 26.72 fm, and 18.8805 fm, respectively. These scattering length patterns are applied to the simulated lipids regardless of chemical identity, which keeps the laterally-averaged transverse scattering length density profiles consistent between different simulations.

density, the simulations are run under tension (to prevent buckling) with fixed total projected area.

Nanometer scale lateral inhomogeneity arises naturally in the Martini coarse grained model by mixing lipids with gradually increased unsaturation content in their two (chemically identical) tails: i.e., the Martini approximations of dipalmitoylphosphatidylcholine (DPPC), with no unsaturation beads, dioleoylphosphatidylcholine (DOPC), with one unsaturation bead per tail, dilinoleoylphosphatidylcholine (DIPC), with two unsaturation beads per tail, and dioctadecatrienoylphosphatidylcholine (DFPC), with three unsaturation beads per tail. These lipids are the *matrix* lipids; they are mixed with 25% DPPC, causing a small DPPC domain to form in the disordered matrix that surrounds it (when chain unsaturation differs enough to cause demixing). Regardless of its chain identity, the scattering lengths of the matrix lipid's sites are assigned equivalent values. This is referred to as a “pseudo-deuteration” scheme, analogous to the experimental strategy to control contrast in SANS. Two beads in each matrix lipid

chain are always pseudo-deuterated, as illustrated in [fig. 4.1](#). This pseudo-deuteration only affects the scattering length for the computation of scattering intensities; it does not affect any forcefield interactions during the simulation. Although real DPPC has 16 carbon atoms per tail, with this version of Martini, there is no difference between an 18-carbon and a 16-carbon chain; it is below the resolution of the coarse-graining. The lipid with no unsaturation beads could equivalently be labeled “DSPC,” which would be consistent with DOPC, DIPC, and DFPC (all would have 18 carbons per tail), but the official name for the Martini molecule is “DPPC,” so that convention is maintained in this work.

For convenience, each Martini system is named by its majority, matrix, lipid type (the minority lipid type is always DPPC). The first system is a special case, but the other three systems will be called “DOPC,” “DIPC,” and “DFPC.” Since the first system is a pure DPPC bilayer, 75% of the lipids are arbitrarily chosen to be labeled as the matrix lipids, although in this case the majority and minority types are equivalent. Consequently, the first system is identified as “DPPC.”

4.2 Simulation parameters

Simulations were performed using GROMACS version 5.1.4[[38](#)], with Martini lipids version 2.0[[21](#)], in the constant surface area ensemble at 323K, for one microsecond. Pressure was controlled with a Parinello-Rahman barostat with $\tau_p = 12.0$ and a compressibility of $3 \times 10^{-4} \text{ bar}^{-1}$ and a reference pressure of 1 bar. The timestep was 20 femtoseconds. Electrostatics were computed using the reaction-field method with $r_{\text{Coulomb}} = 1.1 \text{ nm}$. Van der waals forces were computed with the cutoff scheme ($r_{\text{vdW}} = 1.1 \text{ nm}$). Each simulation included 10,000 Martini water beads. Scattering lengths for computations are provided in [table 4.1](#).

Table 4.1: Martini Scattering Length Assignments. These scattering lengths are computed based on tabulated atomic scattering lengths[33] and an approximate mapping between Martini beads and lipid atoms. All beads are protonated for the purpose of computing their scattering lengths. The second and third beads of each tail in the matrix lipids are assigned the scattering length of an unsaturated carbon chain segment, in accordance with the pseudo-deuteration scheme, regardless of whether they represent saturated or unsaturated chain segments.

| Martini Bead | Scattering Length (fm) |
|-----------------------------|------------------------|
| Water | -6.72 |
| Choline | -5.518 |
| Phosphate | 26.72 |
| Glycerol | 18.8805 |
| Saturated 4x Carbon Chain | -3.332 |
| Unsaturated 4x Carbon Chain | 4.152 |

4.3 Results: PFFT and Dirac Brush methods predict the signature of nanoscopic heterogeneity

Figure 4.2 shows top-down views of the four bilayer mixtures described above, confirming that the Martini systems do exhibit the expected lateral inhomogeneities. Trivially, fig. 4.2a shows that the DPPC system has no lateral inhomogeneities. Importantly, the pseudo-deuteration scheme does not affect the forcefield parameterization, so the arbitrarily-assigned majority and minority lipid labels are uniformly mixed. However, even this trivial case includes the effect of spatially correlated pseudo-deuteration, because the atoms of a single pseudo-deuterated lipid are co-localized by chemical bonding.

Proceeding to the cases with gradually increased unsaturation, the DOPC, DIPC and DFPC systems show increasing segregation of the unsaturated minority lipids, i.e., figs. 4.2b and 4.2c. The extra unsaturation of DIPC increases the chain disorder to the point that DPPC lipids weakly prefer the local environment of other DPPC lipids. While some separation is clear from visual inspection, these small inhomogeneities do not coalesce or grow over time.

In the case of DFPC, with three double bonds per acyl chain, only then do the lipids exhibit full separation into a single two dimensional “droplet”. As expected, the

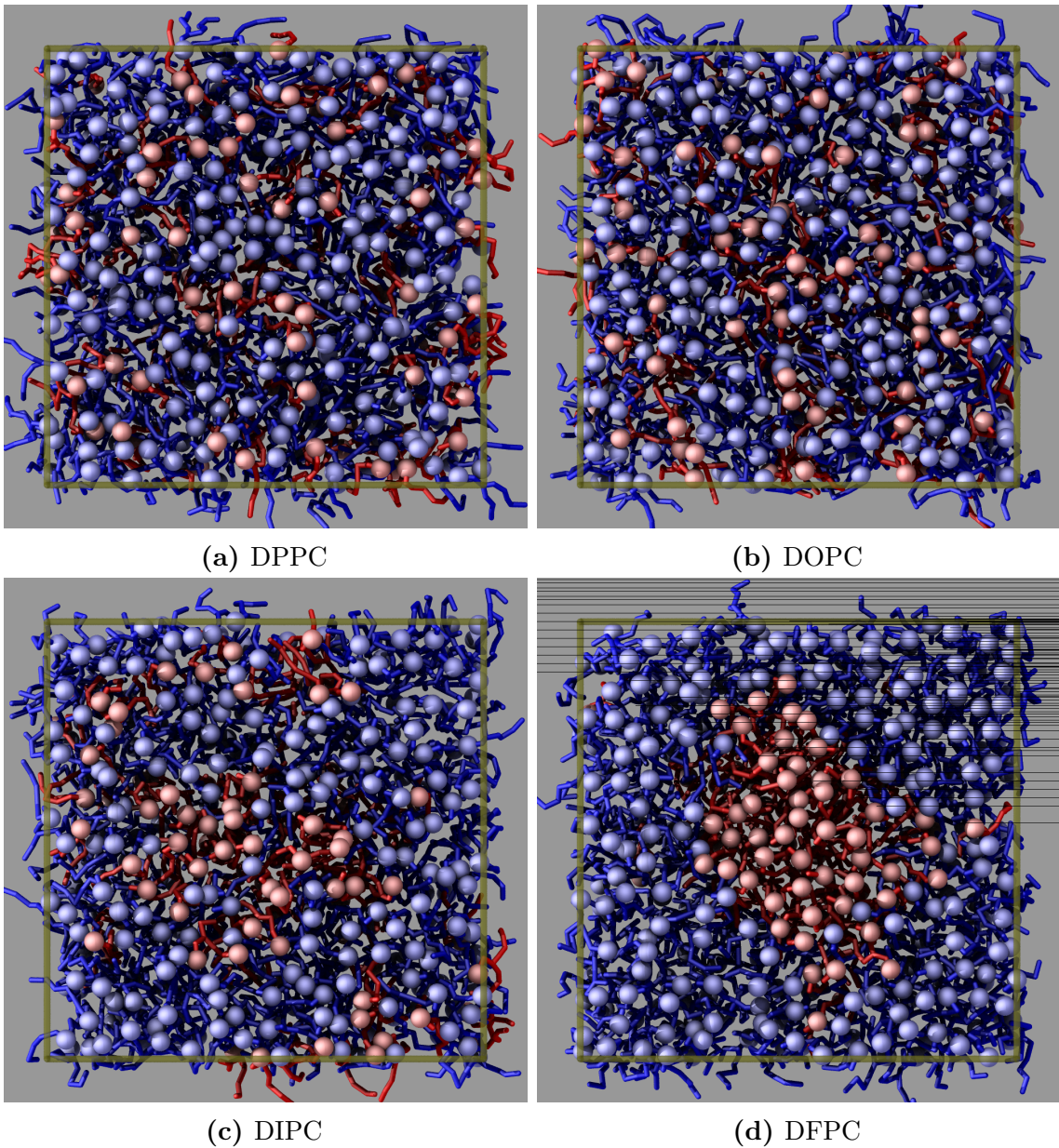


Figure 4.2: Top Views of the Four Martini Systems. The boundaries of the simulation box are drawn in transparent gold. The minority lipid is shown in red, and is always DPPC. The majority (matrix) lipid is shown in blue, with the lipid type indicated in the subfigure captions. In [fig. 4.2a](#), where all lipids are DPPC, a random subset is chosen to represent the matrix lipid for comparison with the other systems.

DPPC lipids strongly prefer the environment of other DPPC lipids, leading to significant demixing that is visible in [fig. 4.2d](#). The separation is much more significant than the DIPC system, with almost every DPPC lipid participating in the same cluster. The edge-on view in [fig. 2.1a](#) reveals measurable differences between the bilayer thickness inside and outside the cluster. Note that in a larger system with more lipids of each type the droplet would be larger—here, the nanoscopic size of the droplet is artificially enforced by the system size.

The range of Martini simulations are thus confirmed to exhibit differing degrees of lateral structure, including a single nanoscopic domain. The effect of the lateral structure on the scattering intensity for each simulation is demonstrated in [fig. 4.3](#), using three different methods for computing the scattering intensity.

By simulating all four systems at constant area, and by using the same pseudo-deuteration scheme for the matrix lipids, it is expected that each system will have approximately the same laterally-averaged scattering density. [Figure 4.3a](#) shows the results of computing the laterally-averaged scattering intensities for all four systems and specifically shows that the intensity patterns are nearly identical for all systems. Small differences between them can be attributed to differences between the simulations, such as in the transverse distributions of lipid density due to differing amounts of chain order, as well as suppressed height fluctuations due to differences in tension. Nevertheless, these systems are practically indistinguishable from each other.

The Dirac Brush method directly captures all lateral and transverse scattering via an analytical solution to the scattering intensity expression. [Figure 4.3b](#) shows the results of analyzing the Martini simulations with the Brush method. The DPPC, DOPC, and DIPC intensities are similar, but the DFPC curve differs substantially near $q = 0.14 \text{ \AA}^{-1}$, indicating excess scattering. The extent of this separation reflects the lateral structure known to exist in these simulations. The depth of the mid- q valley near $q = 0.14 \text{ \AA}^{-1}$ can be interpreted as follows: A shallower mid- q valley indicates the presence of lateral structure, while similar mid- q and high- q valleys indicate little or no lateral structure.

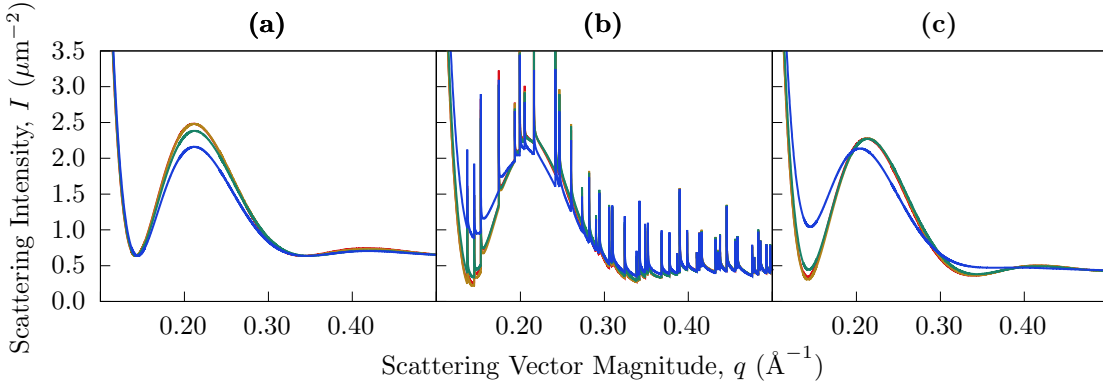


Figure 4.3: Scattering Intensity of the Inhomogeneous Systems, Using Lateral Averaging (a), the Dirac Brush Method (b), and the PFFT Method (c). In each panel, the red curves represent the pure DPPC system, the gold curves the DOPC/DPPC mixture, the green curves the DIPC/DOPC mixture, and the blue curves the DFPC/DOPC mixture. Notice that the red, gold and green curves are similar. The blue curve indicates significant lateral structure through the much shallower valley, a leftward-shifted local maximum, and the absence of the second local minimum near $q = 0.33 \text{ \AA}^{-1}$.

The sharp spike artifacts are Bragg peaks caused by the perfect periodicity of the simulated system (resulting from the periodic boundary conditions). To demonstrate this, the system dimensions (13 nm by 13 nm) are used to predict the locations of the Bragg peaks and compare them to the computed scattering intensity. Figure 4.4 shows the scattering intensity for the DFPC system (without pseudo-deuteration), showing the predicted low order Bragg peaks (marked with blue dots and their indices) and higher order Bragg peaks (grey dots) aligning exactly with the spikes in the data.

The Bragg artifacts can be avoided by using the PFFT method. PFFT has most of the same advantages as the Brush method, but avoids long-range periodic correlations. For demonstration purposes, the cutoff used within this work was chosen to be 30 Å. Figure 4.3c shows the scattering intensities of each Martini simulation, computed using the PFFT method. Comparing figs. 4.3b and 4.3c it is clear that the same conclusions can be drawn using the two different methods, but PFFT does not distract the eye with physically irrelevant Bragg peaks. Although present in the Dirac Brush data, PFFT improves the noticeability of an additional difference between the curves. Specifically, the crest of the DFPC curve is shifted to a lower q magnitude. A

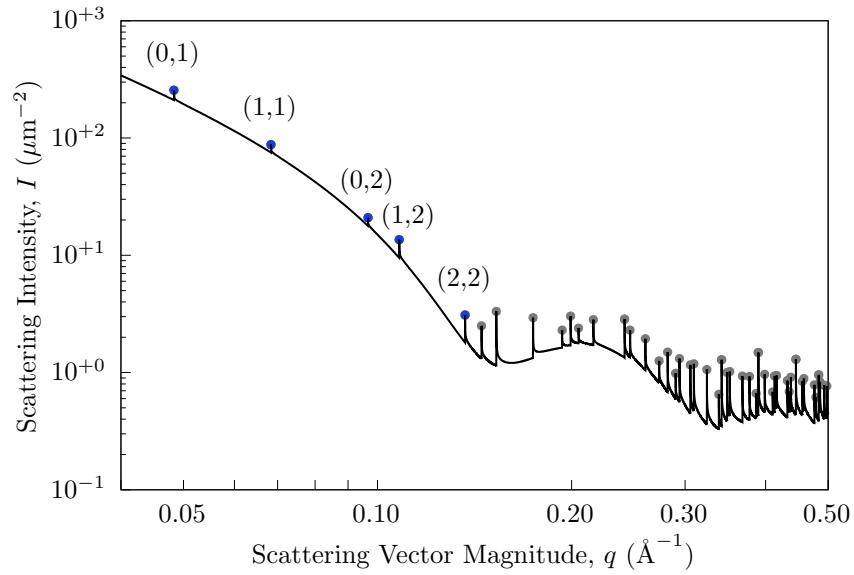


Figure 4.4: Identification of Dirac Brush Spikes. Spurious peaks due to periodic boundary conditions arise from the fully correlated scattering between simulation box images when using the Dirac Brush method. Blue and grey dots indicate the predicted locations of Bragg peaks. The horizontal positions of the markers are computed analytically from the simulation dimensions, while the vertical positions are arbitrarily chosen to visually fall on the curve. A selection of peaks (blue dots) have been labeled with the periodicity indices from which the peaks originate. Bragg peaks are infinitely tall, but are shown here with finite heights due to numerical sampling limitations.

range of alternative cutoff choices are shown in fig. 4.5, where cutoffs greater than 30 Å are shown to be nearly equivalent.

4.4 Discussion

Described were two methods for computing the contribution of spatially correlated *lateral* scattering from a surface to the neutron scattering intensity. Previous works laterally averaged the scattering, and in doing so, removed all in-plane correlations but reduced the data to a single one dimensional Fourier transform. Although this provides a convenient way to determine bilayer transverse structure, it neglects all lateral structural information.

Two different methods were presented to account for lateral contributions to the scattering signal. The first, the Dirac Brush method, is an exact computation of the intensity. However, by making use of the periodically replicated simulation boxes to simulate planar bilayers, the method introduces spurious artifacts that complicate comparison to experiment. The second method, PFFT uses the Debye scattering formalism to separate pairs between a particle-particle contribution and a particle-continuum contribution in the far-field. By doing so, long range correlations are neglected and no periodic artifacts are introduced.

The methods were applied to bilayer simulations of the coarse-grained Martini forcefield, which allowed for convenient simulation of artificially nanoscale domains. By mixing saturated DPPC lipids in a matrix of lipids whose tails gradually became more unsaturated, a range of degrees of lateral inhomogeneity were explored. By tuning the scattering length of the coarse-grained matrix lipids (pseudo-deuteration), the laterally averaged scattering behavior of each simulation was made to be nearly equivalent. This allowed the lateral scattering contribution to be isolated and compared. The signal increased dramatically when the DPPC coalesced into a single domain.

The methods share a similar goal with a simpler approach applied recently to bilayers with lateral structure[39, 40]. In these works, the *in-plane* (two-dimensional) structure factor $S(q) \propto |\sum_i e^{i\mathbf{q} \cdot \mathbf{r}}|^2$ is computed by projecting all structure into the bilayer

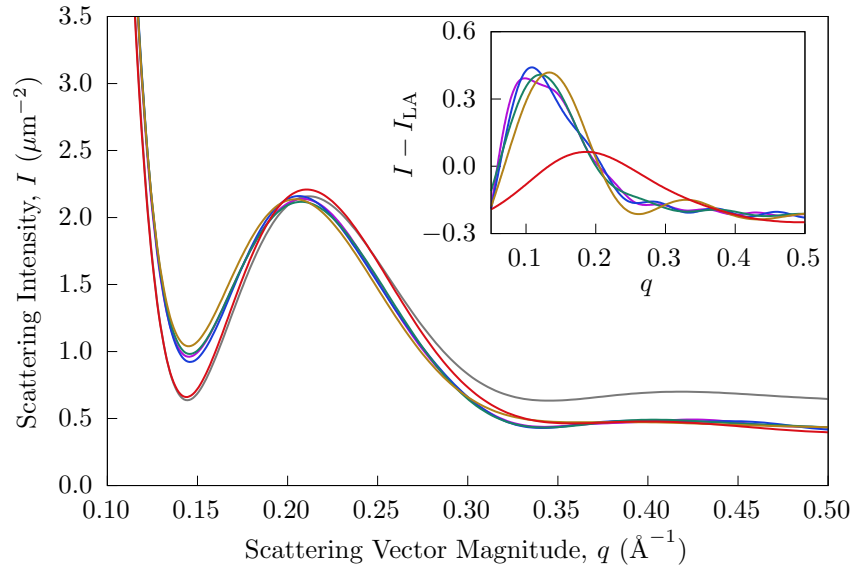


Figure 4.5: Dependence of PFFT Scattering on Cutoff Cylinder Size. Scattering signal varies according to the choice of PFFT cutoff. The black curve represents the intensity resulting from traditional the lateral averaging technique. The red curve uses a cutoff of 10 Å. The gold, teal, blue, and purple curves use increasing cutoffs of 30 Å, 50 Å, 70 Å, and 90 Å, respectively. The inset chart shows the intensity difference obtained by subtracting the laterally averaged curve from each of the colored PFFT curves, illustrating the lateral contributions to the intensity which are captured by PFFT but absent from the lateral averaging technique. Note how increasing the cutoff shifts the first local maximum to lower q in the inset to the figure.

plane. Equivalently, q_z is set to zero. Upon this dimensional reduction, orientational averaging comprises only rotation in the plane of the bilayer. The issue of the special orientation ($q_z = 0$) contributing dramatically to scattering never arises because all orientations have $q_z = 0$. Thus, the spurious artifacts at \mathbf{q} orientations that are both compatible with the periodic boundary conditions and have $q_z = 0$ do not arise. While the in-plane $S(q)$ does report lateral substructure, it does not report the full three-dimensional, orientationally averaged intensity. This approach will be most successful when the scattering density is uniform across the bilayer, a chemically challenging problem. However, Heberle et al were able to match the scattering length density of the headgroup, acyl chain, and solvent regions of a quaternary mixture such that a well-mixed system (high temperature) had minimal scattering[32]. Even in this case, upon demixing, this property may no longer hold for the demixed regions independently (at lower temperature). Alternatively, if a multilamellar bilayer stack can be properly oriented with the neutron beam, scattering can be restricted to those orientations with $q_z = 0$ [41].

With even more highly coarse-grained forcefields it is possible to simulate large lipidic objects (like vesicles) without periodic boundary conditions[42]. This simulation paradigm offers the opportunity to probe both short and long correlation lengths. The PFFT and Dirac Brush methods can be applied to all-atom or coarse-grain resolution simulations of planar bilayers, which can then be compared to such a large length-scale model.

The methods described here can also be applied to complex mixtures of lipids mimicking the plasma and organelle membranes of cells. Although few direct cases of macroscopic lipid phase separation have been observed in living cells[43, 44], nanoscopic complexes of lipids are expected to have unique mechanical properties[45, 46]. Molecular dynamics simulations, in combination with SANS and the data simulation methods presented here, offer a way to model the intensity of complex bilayers to determine their difficult-to-observe nanometer scale structure.

Chapter 5

A HYBRID CONTINUUM APPROACH TO SCATTERING OF CURVED MEMBRANES¹

5.1 Introduction

Over a significant range of composition and temperature, mixing saturated and unsaturated lipids together with cholesterol leads to two-dimensional liquid-liquid coexistence [5, 48]. The physics of line tension leads to perimeter-minimizing circular domains. However, additional physical mechanisms may promote modulated phases [49] that have non-circular equilibrium structure and that arrange on sub-optical lengthscales. This work develops a new tool that combines molecular and continuum modeling to predict the scattering from sub-micron scale structures. The motivation is the hypothesis that liquid ordered (L_o) and disordered (L_d) phases have disparate curvature preferences, leading to non-circular patterning as the compositional variation couples to the wavelength of energetically favorable undulations [50]. As discussed below, continuum modeling can access a much larger range of length- and time-scales than all-atom simulation, while all-atom simulations are able to accurately predict both the strong transverse scattering from lipid bilayers and the spontaneous curvature of lipids. The combination of the two, in the framework presented here, holds the potential to describe the scattering from complex mixtures featuring strong undulations leading to modulated phases [50]. The critical first test in this work is to model the scattering from the extreme curvature of a small vesicle.

The work of Feigenson et al. [36] describes such modulation in lipid bilayers with non-circular equilibrium structure and nanoscopic size. In the quaternary mixtures of

¹ Adapted with permission from Ref. [47]. Copyright 2020 Elsevier.

Ref. [36], modulation occurs when the unsaturated component contains both di-oleoyl and 1-palmitoyl-2-oleoyl phosphatidylcholines (DOPC and POPC, respectively). Förster resonance energy transfer (FRET), a technique that reports nanometer-scale contacts between fluorophores, indicates that di-stearoyl phosphatidylcholine (DSPC), POPC, and cholesterol mixtures are also phase-separated, even though the domains may not be visible by optical spectroscopy [51, 52]. While FRET indicates inhomogeneity, it does not provide direct information on structure; it only indicates the co-localization of probes.

A section of the bilayer must be asymmetric to manifest a curvature preference, otherwise the stresses in the leaflets cancel. In a phase separated bilayer, the L_o and L_d phases can appear out of register such that the opposite phase is on the opposite leaflet. This may be driven by hydrophobic mismatch; the L_o phase is significantly thicker and so by arranging the phases out of register the thickness of adjoining regions match [53, 54, 55]. Coarse-grained simulations have attributed registration effects to curvature [56, 54]. Yet the plasma membrane is known to be highly asymmetric [57]. In Ref. [58], Lorent et al. show that a third of the lipids in the outer leaflet of the plasma membrane have completely saturated acyl chains, while this is true of only a tenth of the lipids in the inner leaflet. Combined with the substantial enrichment of highly curvature-sensitive phosphatidylethanolamine (PE) on the inner leaflet, the ingredients for coupling to curvature are in place. Shlomovitz and Schick point out that while the inner leaflet of the plasma membrane does not have lipids compatible with phase separation, PE may support modulation by curvature-mediated trans-leaflet coupling [59]. Their hypothesis is supported by the instability predicted by Leibler for mixtures of curvature sensitive lipids [60], where dynamic redistribution in the leaflets supports large deformations.

Besides curvature-mediated coupling, a significant out-of-plane dipole in one phase can prohibit large-scale domains [61, 62, 63, 64, 65, 66, 67, 68]. The collective energy increases with the area of the domain (rather than its perimeter) disfavoring

large domains. Amazon et al. [69, 70] employed a combined line-tension/continuum-mechanical model, similar to that of Ref. [71], to demonstrate that differences in bending energy and dipole potential can limit domains at the nanometer-scale.

The main goal of this work is to model small-angle neutron scattering (SANS) from a particular lipid composition as the bilayer responds to lipid curvature stress. SANS operates below the spectroscopic optical limit and gives correlated positions at the nanometer scale. With selective deuteration, the signal from specific lipids can be amplified relative to the background scattering of the environment. The technique has implied the existence of 40-nm diameter membrane features in gram-positive bacteria, where selective deuteration of a targeted membrane is feasible [44]. SANS techniques have been applied to measure the thickness of isolated membrane regions to probe trans-leaflet coupling. For example, Heberle et al. demonstrated that trans-leaflet coupling reduced the thickness of a gel domain in the outer leaflet of a large unilamellar vesicle (LUV) [72]. Similarly, Eicher et al. found that the asymmetric distribution of curvature-sensitive lipids could influence trans-leaflet coupling of the melting transition, with scattering techniques reporting the transverse structure of the phases [73].

The SANS intensity reflects large bilayer structures, including curving undulations of the bilayer. In general for a complex sample with SANS, spatial correlations are entangled and require an accurate model for interpretation. Molecular simulations provide such a model, with complete resolution in time and space. Yet computational resources limit both the duration and size of simulations; this is especially prohibitive when modeling lipid bilayer curvature. Periodic boundary conditions suppress undulations incompatible with the simulation box shape. Yet when the simulation size is extended to the tens of nanometers, simulation times must be also be extended well into the microsecond range to allow for lipid lateral redistribution. Relatively large simulations are necessary so that domains are able to take their preferred shape and size.

Continuum models are a computationally feasible approach to extend modeling well into the regime necessary to model modulated phases. The energetics of membrane

shape is modeled by employing the Helfrich/Canham [74, 75] Hamiltonian. The most straightforward way to model compositional fluctuations is through a two state model built on line tension. This approach is able to reproduce the temperature-dependent dynamics and fluctuations in the size of domains [76, 77]. With these basic elements the challenge is to add to the continuum model additional physical effects leading to size and shape modulation in more complex mixtures.

The nanometer-scale hexagonal packing of L_o phases observed in the simulations of Ref. [78] approaches the range of feasible lipid spontaneous curvature where the local shape of the leaflet and composition could strongly couple. A key compositional factor is cholesterol. Not only does cholesterol partition between the two phases, but simulations predict that curvature stresses arising from cholesterol in the two phases are very different [46]. This interpretation stands in contrast to the axiom that spontaneous curvature is an intrinsic property of lipids, rather than that of domains of a particular composition. The difference is stark; given the high cholesterol content of ordered phases, and the high negative spontaneous curvature of cholesterol both from simulation and experiment, the ordered phase should itself have significant negative spontaneous curvature [79]. However, the CHARMM forcefield (which shows cholesterol's negative spontaneous curvature in disordered phases) indicates ordered domains have *positive* spontaneous curvature [46]. This difference in spontaneous curvature supports the hypothesis that curvature preferences are a factor in modulation.

This work addresses the need for simulation methodology to assist in the interpretation of SANS experiments of inhomogeneous bilayers, emphasizing how inhomogeneity couples to high curvature. An additional use is to predict the magnitude of coupling effects to see how they will be visible to SANS. This includes whether they will be distinguishable from competing signals, such as the distribution of vesicle sizes and composition that are inherent in any experiment. The approach is based on taking data from simulations of manageable size, i.e., small bilayer patches and, through continuum modeling, translate these into the full scattering from vesicles, including predictions of how lipid redistribution will couple to curvature.

The work here is based on previous similar efforts to compute scattering from inhomogeneous systems. Carrillo et al. applied highly coarse-grained, implicit solvent molecular modeling to model the scattering from small vesicles [42]. They point out that the scattering can be computed from the Debye formula, in which pairs of scatterers are summed over, or by using a three dimensional fast Fourier transform (FFT), the cost of which depends on the FFT grid density. With this explicit particle approach, they were able to determine the time-dependent correlation of the scattering intensity, enabling comparison to spin-echo experiments. This framework is attractive in that the underlying molecular model naturally has the full set of elastic deformations, which otherwise must be added explicitly to continuum models. However, to accurately predict the complete scattering of a vesicle at high q where molecular scale features are represented, the detail of an all-atom model is likely necessary. The reference calculation we perform here for the scattering of a Martini vesicle uses the same approach as in Ref. [42].

Vesicle scattering has been approximated by separating the vesicle form from the transverse component (the scattering length density variation along the bilayer normal). See, for example, Ref. [80] that develops a model that combines the scattering form of polydisperse distribution of vesicle sizes with an approximation for the transverse structure. Significant insights into the structure of bilayers are gained from simple forms for the transverse structure, including fitting with “three-level” or “top hat” functions [81, 82, 83], Gaussian functions [84, 85, 86], or other simple forms used to represent variations in the density. Henderson used a Monte Carlo model to sample the scattering from multiple aggregates [87]. Heberle [88] et al. developed a general theory to predict the scattering from vesicles containing phase-separated circular domains, extending Henderson’s Monte Carlo sampling to verify their theory. The scattering modeled in Ref. [88] reflects both vesicle shape as well as lateral correlations due to phase separation. The hexagonal substructure observed for the L_o phase in Ref. [78] belongs in a separate class of lateral heterogeneity not apparently driven by line tension, but by the molecular scale interactions of individual lipids. To model this very fine

structure, two of the present authors designed an algorithm that separates close-ranged correlations from long range correlations to mitigate finite size effects when applied to modestly-sized simulations [24].

The approach of this work is to develop a method capable of taking information from a small patch of Martini bilayer and employing a continuum model to predict the full scattering. Small vesicles are used as a testing ground, not simply because they are convenient to simulate, but also because strong curvature, as they exhibit, is hypothesized to contribute to the nanometer-scale modulation of domain shapes in complex mixtures. A related challenge is to characterize the stresses present in those small vesicles and parameterize that stress into the continuum model. It is unclear if the highly curved leaflets of a small vesicle can be interpreted in terms of the mechanical parameters of planar simulations. The method developed here parameterizes leaflet lateral strains so that the scattering of vesicles with strained leaflets can be predicted.

5.2 Methods

5.2.1 Coarse-grain Martini modeling

All simulations were run in GROMACS [38]. The temperature was equilibrated at 310.15 K using a combination velocity rescaling/stochastic algorithm [89]. A timestep of 20 femtoseconds was employed, as is appropriate for the soft Martini potential. The standard dielectric constant for Martini, 15, was used.

Vesicle systems were built using the Vesicle Builder component of the CHARMM-GUI Martini Maker online tool [90]. The CHARMM-GUI system is a widely used scheme for constructing all-atom and coarse-grained simulations, especially those containing bilayers [91]. The Vesicle Builder module was built recognizing the difficulty of constructing a vesicle with the correct lipid and osmotic-stress balance and takes special measures to prevent these stresses. These measures are reviewed here but originally appeared in Refs. [92, 93].

Six pores, aligned on the Cartesian poles, are formed in the vesicle by temporarily applying collective potentials that prevent lipid tails from entering the region. During

this equilibration period, exceeding a microsecond, lipids are able to move between the leaflets, in some part relieving lipid imbalances. Just as importantly for achieving zero tension, water moves between the inside and the outside of the vesicle. With too much water, the vesicle bilayer will be under positive tension, expanding the bilayer area and limiting fluctuations. With too little water, the bilayer will contract or pucker inward. The external potential is then slowly removed and equilibration continues. The vesicles were built entirely of POPC, following which 10% of the inner leaflet lipids were mutated to POPE.

Two vesicles, consisting of POPC on the outer leaflet and a 90:10 POPC:POPE ratio on the inner leaflet, were simulated for two microseconds. A large vesicle had a diameter of approximately 18 nm shown in [fig. 5.1](#), while a smaller one had diameter approximately 13 nm (measured at the bilayer midplane). Configurations were sampled every nanosecond. The scattering lengths for the groups were set to -0.5158 for NC3, -0.2649 for NH3, 2.672 for P04, 1.888 for the GL beads, -0.3332 for the saturated acyl groups, and 0.4152 for the unsaturated sites (see [fig. 5.2](#)). The scattering length density was computed on a 2 Å grid and the FFT was computed and squared. The intensity was averaged over the 2000 frames of simulation data.

Planar systems were built and simulated with GROMACS to compute the transverse neutron scattering length density (NSLD), $\beta(z)$. The CHARMM-GUI bilayer builder was used [\[91\]](#). The standard CHARMM-GUI equilibration procedure was used, followed by 200 nanoseconds of production dynamics. The NSLD of the asymmetric POPC/POPE mixture was computed from a small planar simulation with 100 lipids per leaflet (100% POPC in the top leaflet, 90:10 POPC:POPE in the lower leaflet). The laterally-averaged scattering length density was computed by performing a histogram in the z dimension (with length approximately 80 Å) with 250 bins.

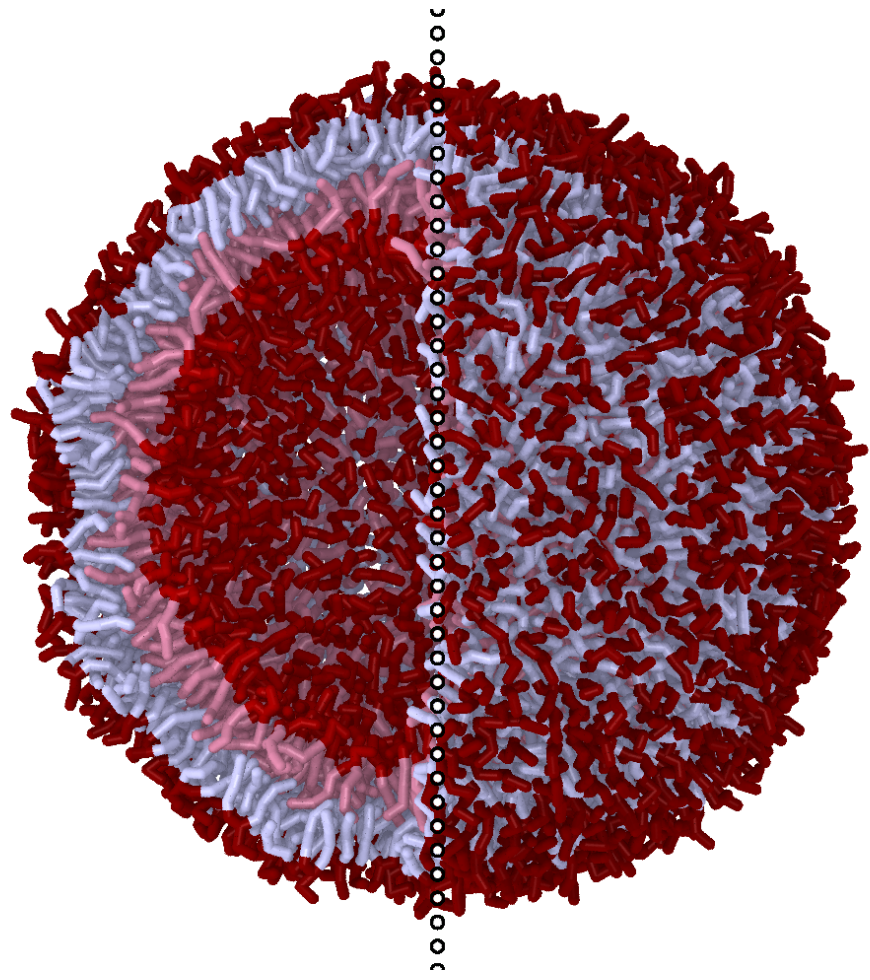


Figure 5.1: Rendering of a Ca. 18 nm Diameter POPC/POPE MARTINI Vesicle, the scattering from which that of the hybrid continuum/planar-molecular modeling is compared. To the left of the vertical dotted line the near lipids are hidden to show the vesicle interior. Tail interaction sites are light while surface sites are dark. The inner and outer leaflet lipids are tinted separately.

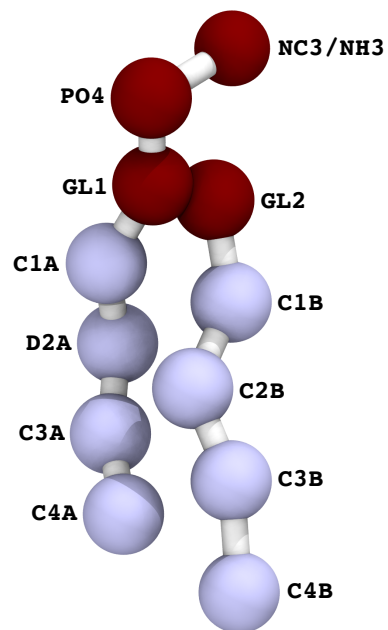


Figure 5.2: Illustration of MARTINI POPC/POPE with Bead Names. The POPC (with NC3) and POPE (with NH3) lipids used in the study are illustrated above. The interaction site names (e.g., C2B) are referred to in the text regarding the pivotal plane of bending.

5.2.2 Material deformation of a planar scattering length density to model curvature

The approach here to modeling the complete scattering from a vesicle consisting of a single liquid-ordered bilayer is to combine continuum modeling of large dynamic structures with the laterally averaged scattering length density β_{LA} computed from molecular simulation. [Figure 5.3](#) illustrates the method for computing the contribution of shape and dynamical fluctuations to the scattering intensity. The fluctuations of the sphere are computed using a spherical harmonic representation of the (two dimensional) surface. The three-dimensional scattering length density is evaluated using the $\beta_{\text{LA}}(z)$ distribution computed from a planar simulation. At a given point on the surface, here in general $\{u, v\}$ coordinates, the position is $\mathbf{r}(u, v)$ and the normal is $\mathbf{n}(u, v)$. The lipid density at a point is computed using the square root of the metric tensor, g_{uv} . The normal, metric tensor, and curvature are computed using standard techniques of differential geometry, based on the first and second derivatives of $\mathbf{r}(u, v)$ with respect to u and v [\[94\]](#).

The basis of the continuum model is to use the bilayer midplane to evaluate the Helfrich/Canham [\[74, 75\]](#) curvature energy of the fluctuating bilayer:

$$E = \int_A \frac{\kappa}{2} (c - c_0)^2, \quad (5.1)$$

where c is the curvature and c_0 is the spontaneous curvature. The distribution of scatterers *off* the midplane is then computed based on $\beta_{\text{LA}}(z)$, itself computed from a simulation of a flat bilayer. The methodology here corrects for the change in the scattering length density of a curved bilayer according to the assumption that the area at the neutral surface is constant, and that the volume of the bilayer is conserved everywhere up to second order in the curvature. The constant volume assumption is strongly indicated by simulations and experiment [\[95\]](#). For a positively curved bilayer, for example, that of the outer leaflet of a vesicle, there is more surface area near the neutral surface ($4\pi[R + z_{\text{ns}}]^2$) than there is at the bilayer midplane ($4\pi R^2$). For this example, the ratio of these two areas is $1 + 2z_{\text{ns}}R^{-1} = 1 + z_{\text{ns}}J$ to first order in J , where

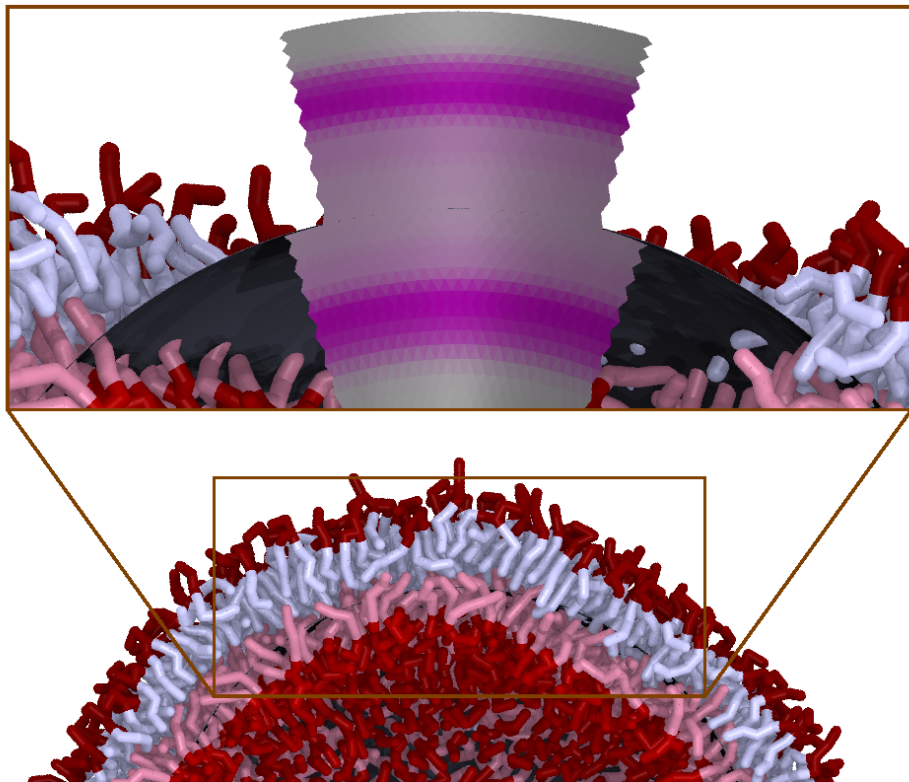


Figure 5.3: Illustration of Surface Continuum Model with Scattering Length Density Profile from Molecular Simulation. The scattering length density profile, $\beta_{LA}(z)$, is used to compute the scattering from a dynamically fluctuating vesicle of a particular size. A frame of a simulation of a Martini vesicle is shown (water is removed from the image for clarity). In the inset, a portion of the lipids are removed and the continuum model is shown. The underlying continuum model is shown in dark grey while the deformed NSLD is shown for both the outer and inner leaflets. The shapes of the inner and outer leaflets are discontinuous because, in this model, the leaflets deform semi-independently (they share the same midplane). The Martini model for the inner and outer leaflets are tinted differently.

J is the sum of the two principal curvatures, here $R^{-1} + R^{-1} = 2R^{-1}$ for a perfect sphere. At constant volume, the change in area is compensated for by a change in thickness, described below.

Given J computed at $\{u, v\}$, the area of lipid material occupied $A(z)$ a distance $\Delta z = z - z_{\text{ns}}$ from a patch of the leaflet at its neutral surface z_{ns} (with area A_0) is

$$A(\Delta z) = A_0 + A_0 J \Delta z, \quad (5.2)$$

where the lateral strain is

$$\epsilon_{\text{lateral}}(\Delta z) = J \Delta z \quad (5.3)$$

and $z = 0$ is the bilayer midplane. To preserve volume at first order in J , the leaflet deforms along the bilayer normal with transverse strain $\epsilon_{\text{transverse}}$ to cancel $\epsilon_{\text{lateral}}$:

$$\epsilon_{\text{transverse}}(\Delta z) = -J \Delta z \quad (5.4)$$

For convenience the material transverse coordinate, z' of the deformed bilayer is defined in terms of the undeformed resting coordinate z as

$$\begin{aligned} z' &= \int_0^z dt [1 + \epsilon_{\text{transverse}}(t - z_{\text{ns}})] \\ &= z [1 + J(z_{\text{ns}} - \frac{1}{2}z)] \end{aligned} \quad (5.5)$$

The two leaflets of a bilayer have local curvature with sign opposite to that of the other. For a particular point at the bilayer midplane, there will be a greater local density of lipids on the positive curvature side of the bilayer, as opposed to the negative side. Consider an arbitrary point z , the transverse coordinate of the leaflet. The scattering length of the continuum element is $\beta_{\text{LA}}(z)$. The coordinate of the scatterer is then computed as

$$\mathbf{r}(u, v, z) = \mathbf{r}(u, v) + z'(z) \mathbf{n}(u, v) \quad (5.6)$$

where z' is computed from eq. (5.5). Equation (5.5) is modified depending on which leaflet is being sampled; to switch the orientation of the leaflet, the sign of J and the normal must be reversed.

After selecting a position at the midplane by $\{u, v\}$, the *number* of lipids in a particular leaflet must then be adjusted for curvature. In general, a point on a surface will not be specified by a Cartesian system $\{x, y\}$, where the area element of a patch of tiny patch is $dx dy$ and the units are unambiguous (e.g., meters). Rather, a generalization is employed, with coordinates labeled with $\{u, v\}$. The area element in the vicinity is computed via the *metric*, the map between the arbitrary coordinates and real space. For example, in a spherical coordinate system ($\{\theta, \phi\}$), this factor is $r^2 \sin(\phi)$, where ϕ is the azimuthal angle. The factor is computed using the general formula $|\mathbf{r}_u \times \mathbf{r}_v|$, where \mathbf{r}_u and \mathbf{r}_v are the derivatives of the surface position with respect to the general coordinates. To randomly select a set of scattering elements from the continuum surface, a random point $\{u, v\}$ is multiplied by

$$w = |\mathbf{r}_u \times \mathbf{r}_v| \quad (5.7)$$

The area of the lipid is constant with curvature not at the bilayer midplane, but at z_{ns} . To account for this, the weight is modified on a per-leaflet basis according to curvature.

$$w' = w(1 + Jz_{ns}) \quad (5.8)$$

where the sign of J depends on the leaflet considered.

Lateral strain can be introduced into a leaflet using the simple volume preserving transformation

$$\begin{aligned} x' &= x(1 + \frac{1}{2}\epsilon_{lateral}) \\ y' &= y(1 + \frac{1}{2}\epsilon_{lateral}) \\ z' &= z(1 - \epsilon_{lateral}) \end{aligned} \quad (5.9)$$

This strain alters the number of lipids in the continuum-modeled leaflet as:

$$w'' = w'(1 - \epsilon_{lateral}). \quad (5.10)$$

For example, if the area of the lipid is increased, fewer lipids are required to cover the surface.

The weight of the scatterer, equivalent to its probability, w'' , which accounts for the change in density with curvature and strain. The transverse and lateral strains of the leaflet are zero at the neutral surface. This applies both to the inner (negative) and outer (positive) leaflets. For the positively curved leaflet, the strain at the midplane is *negative*; it has been compressed. For the negatively curved leaflet, the strain at the midplane is positive. Therefore, *per unit midplane area*, the positively curved leaflet has more lipids, by a factor of $\frac{1+Jz_{ns}}{1-Jz_{ns}}$.

5.2.3 Continuum modeling

The dynamics of the membrane are propagated using Brownian dynamics (see for example Ref. [96]), where the dynamical variable is the amplitude of the $n = 2$ to $n = 6$ spherical harmonic of the vesicle. The surface is evaluated using the subdivision limit surface (SLS) algorithm [97]. The SLS component of the software package is not necessary for the vesicle calculation here; the calculation could be done analytically for these simple spherical deformations. However, the SLS allows for modeling arbitrary topology surfaces, so that, for example, lipidic cubic phases, pores, and other special structures can be simulated. The mesh for the SLS consists of 162 mesh points formed by applying Loop subdivision [98, 99] twice to an icosahedron. The curvature energy ([eq. \(5.1\)](#)) of the mesh is evaluated using three point integration on each face. For faces containing an irregular mesh point (with five neighbors), a 16 point Gaussian-quadrature rule is applied to increase accuracy. With the SLS, the spherical harmonic deformations should not be applied directly to the mesh vertices, because the surface itself is a linear transformation of the those vertices. Instead, the mesh displacements for a spherical harmonic deformation are determined by solving for the linear transformation of the mesh points that best yields a particular spherical harmonic (evaluated at the integration points). The dynamics of the spherical-harmonic amplitudes evolve under the influence of the energy in [eq. \(5.1\)](#). The bending modulus was set to 25 kcal/mol. Fluctuations in thickness beyond those controlled by curvature were not modeled.

5.2.4 Evaluating $I(q)$

The coherent SANS intensity $I(\mathbf{q})$ a distance r_D from the detector is determined by

$$\psi(\mathbf{q}) \propto r_D^{-1} \sum_i b_i e^{i\mathbf{q} \cdot \mathbf{r}_i} \quad (5.11)$$

$$I(\mathbf{q}) = |\psi(\mathbf{q})|^2 \quad (5.12)$$

where b_i is the neutron scattering length of atom i at position \mathbf{r}_i , and \mathbf{q} is the scattering vector determined by the detector position relative to the sample and neutron beam. The static (large) factor r_D is irrelevant and will be dropped for convenience. There is a one-to-one correspondence of scattering vectors \mathbf{q} and detector positions. The absolute-squared-sum can be expanded to yield:

$$I(\mathbf{q}) = \sum_i \sum_j b_i b_j e^{i\mathbf{q} \cdot (\mathbf{r}_i - \mathbf{r}_j)} = \sum_{ij} b_i b_j e^{i\mathbf{q} \cdot \mathbf{r}_{ij}} \quad (5.13)$$

where the negative sign on \mathbf{r}_j is a result of complex conjugation when computing the absolute magnitude squared, and $\mathbf{r}_{ij} = \mathbf{r}_i - \mathbf{r}_j$.

Whereas with eq. (5.12) the wavefunction ψ must be computed for the complete system before squaring (the sum is inside the square), with eq. (5.13) many incomplete sums of scattering pairs can be computed and averaged over time.

The use of eq. (5.13) also makes orientational averaging convenient. Orientational averaging of a configuration can be accomplished by averaging over each orientation of \mathbf{r}_{ij} , or alternatively, over each orientation of \mathbf{q} :

$$I_\Omega(q) = \sum_{ij} b_i b_j (4\pi)^{-1} \int_0^{2\pi} d\theta_q \int_0^\pi d\phi_q e^{i\mathbf{q} \cdot \mathbf{r}_{ij}} \quad (5.14)$$

where $\mathbf{q} = q\{\sin(\theta_q) \sin(\phi_q), \cos(\theta_q) \sin(\phi_q), \cos(\phi_q)\}$. For convenience the integration can be performed by aligning \mathbf{r}_{ij} with the q_z axis ($\phi_q = 0$) such that $\mathbf{q} \cdot \mathbf{r}_{ij} = qr_{ij} \cos(\phi_q)$:

$$\begin{aligned} I_\Omega(q) &= \sum_{ij} (4\pi)^{-1} \int_0^{2\pi} d\theta_q \int_0^\pi d\phi_q \sin(\phi_q) e^{iqr_{ij} \cos(\phi_q)} \\ &= b_i b_j \frac{\sin(qr_{ij})}{qr_{ij}} \end{aligned} \quad (5.15)$$

The SANS intensity of the continuum model was determined by evaluating the following procedure for each of 5000 configurations of the simulation. One thousand randomly sampled points (u, v) were chosen from the bilayer midplane of the sphere. At each of these points, twenty points along the *planar* z coordinate were drawn. By drawing points from the distribution of NSLD in the planar simulation, it is assured that points in the material are sampled evenly. The final position of the scattering element in three dimensions is determined by first applying the lateral deformation (eq. (5.9)) to z , then using eq. (5.5). The weight w'' is determined from eqs. (5.7), (5.8) and (5.10). From this set of points, 10^5 pairs are drawn and are used to sample eq. (5.15), with each pair multiplied by the product of each points' weight, w'' . The Fourier transform method yielded equivalent results, with the sampled points put onto a fine grid.

5.3 Results & Discussion

5.3.1 Deformation of the small-vesicle leaflets

The deformation predicted by eq. (5.5) is predicated on pointwise conservation of volume as the material deforms. This is justified on a longer lengthscale by the area compressibility modulus (per unit height) compared to the bulk modulus of the material [100, 95] and is borne out in analysis of molecular simulation [95]. However, it is not clear that the mechanical parameters of the lipid, determined for the planar system (see, for example Ref. [101]) will be applicable to highly curved leaflets. For the inner leaflet, all-atom simulations have shown consistency in the spontaneous curvature with hexagonal phase simulations [102]. Furthermore, the Martini model may display different behavior at high curvature than all-atom models.

To determine the values of z_{ns} and $\epsilon_{\text{lateral}}$ applicable, the density of coarse-grain Martini sites is examined. The area-per-lipid of the 18 nm diameter vesicle, broken down by Martini interaction site, is plotted in fig. 5.4. The data are plotted against the height above the bilayer midplane for a planar simulation on the horizontal axis. The area-per-lipid of the planar system is plotted as a horizontal line in the same plot. The

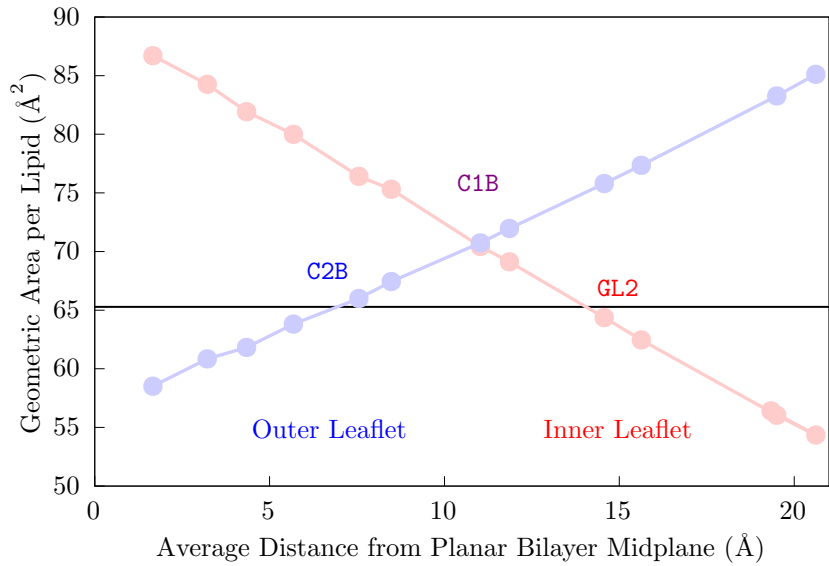


Figure 5.4: Geometric Area-Per-Lipids of Martini Sites. The area-per-lipid ($4\pi R^2$ divided by the number of lipids) of a Martini site in a ca. 18 nm diameter vesicle is plotted against the same site's height above the bilayer midplane in a planar simulation. The form is expected to be linear, as per eq. (5.2). The area-per-lipid for the planar system, plotted as a horizontal line, is the projected area of the bilayer. The inner leaflet curve (red) plots both the NH3 sites of POPE as well as the NC3 sites of POPC. The outer leaflet curve (blue) has only POPC.

pivotal plane, defined by the position in a curved leaflet for which the area-per-lipid is constant, is determined by the intersection of the data with the horizontal line. However, if the leaflet is strongly deformed, for example, by an area strain due to external tension (or that applied by the opposite leaflet and/or osmotic stress), the intersection will shift. The blue data corresponds to the outer leaflet. For the outer leaflet, the area-per-lipid matches that of the planar system at the Martini C2B site.

The pivotal plane and neutral surface are closely related. The pivotal plane reflects the fact that lipid spontaneous curvature acts to strain the leaflet as curvature energy is balanced against lateral tension. For example, lipids with extreme negative spontaneous curvature may prefer to be strained such that their radius is decreased. As shown by Leikin et al. [103], the difference is on the order of 1-2 Å for high spontaneous curvature lipids. Given this, the two are treated as equivalent within the uncertainties at play in this work.

The parameters of the mechanical transformation (eqs. (5.5) and (5.9)) cannot strongly differentiate between a shift in the neutral surface and a latent area/thickness strain. A shift in the neutral surface would arise from, for example, a highly curved outer leaflet being unable to accommodate the thickening of the acyl chain region due to fundamental limits on molecular flexibility. In this case, the neutral surface would shift toward the middle of the bilayer. This is effectively indistinguishable from a leaflet-number imbalance between the inner and outer leaflets.

5.3.2 Comparison of the continuum and coarse-grain modeled intensity

The SANS intensities of the coarse-grained model and the continuum model (with mechanical parameters matched to fit) of the 13 nm and 18 nm diameter vesicles are shown in figs. 5.5 and 5.6, respectively. The strains ($\epsilon_{\text{lateral}}$) and neutral surface positions (z_{ns}) of the inner and outer leaflet, as well as the radius of the vesicle itself, have been optimized over a rough scan of parameter space to match the average radial scattering length density. The final intensity is determined by optimizing a scaling factor

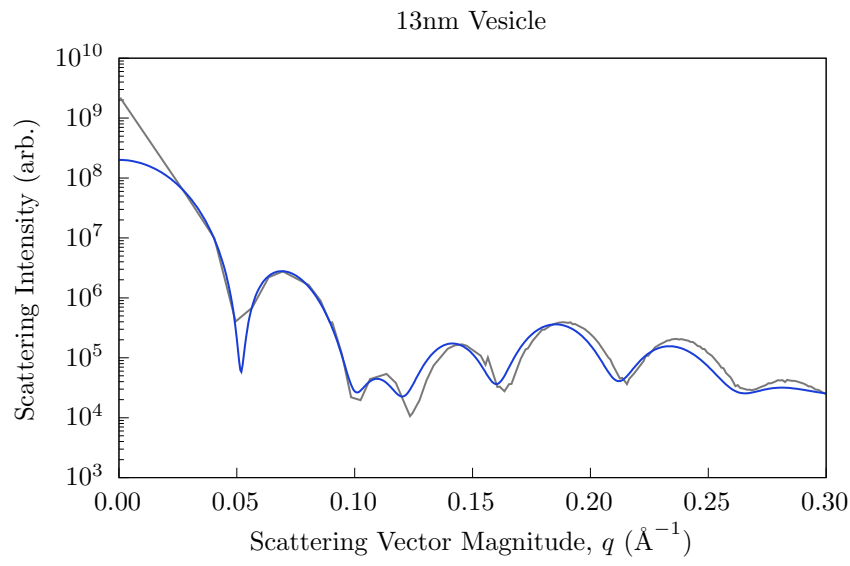


Figure 5.5: Scattering Intensity of a 13nm Diameter Vesicle Vs. the Hybrid Model. The scattering computed directly from that of a ca. 13 nm diameter Martini vesicle (grey) and that of a hybrid continuum/planar-molecular simulation of the same system (blue).

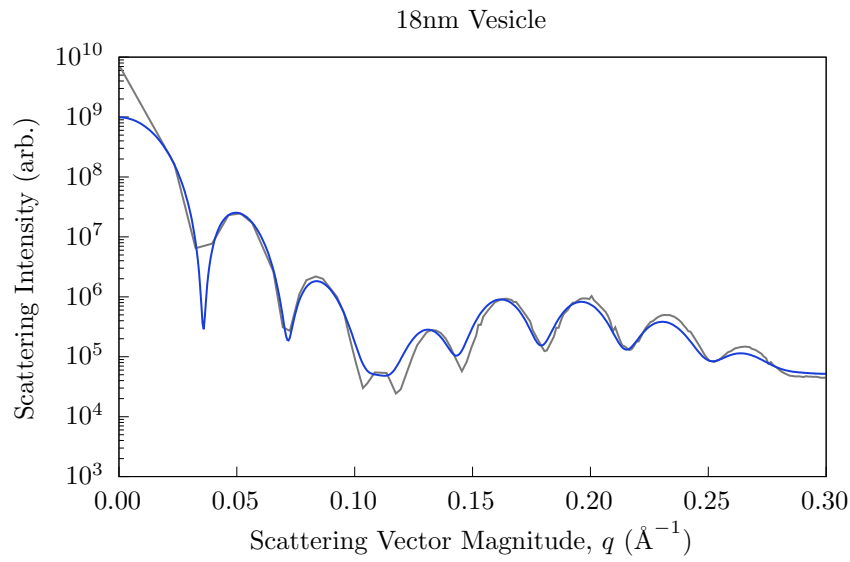


Figure 5.6: Scattering Intensity of an 18nm Diameter Vesicle Vs. the Hybrid Model. The scattering computed directly from that of ca. 18 nm diameter Martini vesicle (grey) and that of a hybrid continuum/planar-molecular simulation of the same system (blue).

and constant to the continuum intensity. The constant represents the contribution due to the finite scattering length of the Martini interaction site.

The best fit scattering intensities have separate neutral surfaces for the inner and outer leaflet, with $z_{ns} = 9 \text{ \AA}$ for the outer leaflet and $z_{ns} = 15 \text{ \AA}$ for the outer leaflet. These are consistent with the plotted area-per-lipid as a function of atom type in fig. 5.4. The optimal parameter set included a 10% strain in the outer leaflet in the 18 nm vesicle, although this was not differentiated from a shift in the neutral surface. The same strains and neutral surface positions were applied to both the 13 nm diameter vesicle simulations, but with an additional 10% strain to the inner leaflet. A bending modulus of 25 kcal/mol produced the best agreement of the scattering intensity. If the bending modulus is reduced to 15, the magnitude of the shape oscillations at high q are reduced by half, and are washed away for smaller values.

The accuracy of the match was most sensitive to the thickness of the bilayer (which most closely determined the transverse correlation) and the overall size of the vesicle (which determined the “beat” of oscillations at the vesicle size). Thus, the quality of the fit can be viewed as using continuum modeling to verify the overall transverse structure of the bilayer in a highly curved system. Experimentally, vesicle samples will have a distribution of size, likely making comparison with models challenging. However, the accuracy here is important for precision comparisons, including with hypotheses regarding the structure of modulated phases [50].

5.4 Conclusions

A methodological framework, along with accompanying software, is presented to compute the scattering of high curvature regions of leaflets. The primary targets for testing were coarse-grained (Martini) simulations of very small (13-18 nm diameter) vesicles. Although the vesicles were equilibrated in such a way as to remove osmotic and lipid-number stresses, apparent strains were observed. The accuracy of the model was excellent, where given the radius and thickness of the vesicle, a nearly quantitative model of the scattering could be determined.

Extension to all-atom simulations of lipid bilayers is warranted, considering that the observed neutral surface for highly curved Martini lipids appears to be very different from that obtained from a buckled planar bilayer [104, 105]. Maintaining the same elastic coefficients (neutral surface location) appears unbearable for the outer leaflet of small vesicles; the acyl chains must extend and narrow too far. For example, in Risselada et al. [92], the authors observed that highly flexible lipids in the outer leaflet would “backfold”, lifting a disordered tail up out of the compressed midplane space. Considering the limited resolution of the Martini forcefield, this suggests that all-atom models could be quite different, in terms of interdigitation.

Recently, Hossein and Deserno [106] pointed out that a membrane with a strong spontaneous curvature imbalance (as is apparent from the asymmetric lipid distribution of PE) should spontaneously tubulate, and that an imbalance in lipid number could counteract this. Characterization of differential stress is challenging because it must be resolved on the *leaflet* level, as opposed to the total bilayer tension. Scattering offers the possibility of distinguishing leaflet properties. A drawback is that the intensity of asymmetric bilayers does not typically go to zero at characteristic locations, making interpretation more challenging. The intent of this work is that precision modeling will enable the interpretation of such complex systems.

The natural extension of this continuum modeling approach is to combine line tension energetics that yield domain formation with spontaneous curvature and NSLD information computed from simulation [24, 46]. Many of the elements are already present in the work of Hu et al. [71] and Amazon et al. [69, 70], in which membrane deformation couples to the line tension.

Chapter 6

INDICATIONS OF NANOMETER-SCALE HETEROGENEITY IN LIQUID-ORDERED BILAYERS

6.1 Introduction

The lipid composition of the outer leaflet of the plasma membrane is enriched in sphingolipids [58] and cholesterol shown to form liquid ordered (L_o) phases [107] below physiological temperature. In addition to these basic ordered-phase elements (sphingomyelin and cholesterol), transmembrane proteins in the membrane have large footprints and will influence phase behavior [108]. Clusters of B-cell receptors and ordered-phase dyes were recently established in both living and fixed cells [109], demonstrating the functional consequences of lipid phase behavior. However, the molecular structure of ordered phases has yet to be adequately characterized experimentally. Unlike the molecular structure of proteins, which often permit high-resolution structure determination, bilayer patches are dynamic liquid structures, which necessitates different kinds of experimental techniques, better suited to soft matter condensed phases. The problem is complicated by the observation of nanoscale patches of hexagonally packed chains in mixtures of saturated hydrocarbon and cholesterol in molecular dynamics simulations [78, 23]. This work applies small-angle neutron scattering and molecular simulation to demonstrate that ordered phases indeed have nanometer-structure beyond lipid-lipid contacts. The experimental detection of nanoscale structure in ordered membrane phases has important implications for how L_o phases influence protein conformational change and how these lipids determine the mechanical properties of membrane superstructures.

The miscibility phase diagrams of lipid cholesterol mixtures have been studied for decades [110, 111, 112, 107, 113]. Of particular importance to the present work is

the existence of two fluid phases which differ in composition and chain order. The L_o phase (introduced above) is marked by enrichment of cholesterol and phospholipids with saturated acyl chains. Simulations and nuclear magnetic resonance spectroscopy (NMR) studies of the L_o phase indicate that these saturated acyl chains are close to all-*trans* [78].

Recent lipidomes, determined separately for the inner and outer leaflet of the human red blood cell membrane, found a stark asymmetry in lipid tail saturation, with a plurality of outer leaflet plasma membrane lipids possessing two saturated tails. While the balance of cholesterol between the two leaflets is still an open question, the outer leaflet has a composition similar to L_o .

While the diffusion constant of lipids in the L_o phase is slower than that of lipids in the L_d phase, they remain fluid, unlike the gel phase of saturated lipids, L_β , which also has nearly all-*trans* acyl chains, albeit tilted [114]. Molecular dynamics simulations of the L_o phase [78] using the CHARMM all-atom forcefield [10] suggest a resolution of this: saturated lipids are sequestered into nanometer-scale domains where they appear as a small patch with mostly *trans*, hexagonally packed tails. The hexagonal regions are bordered by rigid cholesterol, to which it presents a relatively smooth surface. The remaining space defines an interstitial zone populated by more disordered, unsaturated lipids. Saturated lipids exchange between the hexagonal nanometer-scale domains, leading to fast diffusion relative to the L_β .

Transmembrane proteins function with the bilayer acting as the solvent for their hydrophobic regions, and yet the bilayer presents more than just a fluid oily surface [115] as the protein changes its shape to perform its function. Unlike a simple fluid in three dimensions, a bilayer is anisotropic; creating space for protein side chains changing conformation near the lipid head-groups requires a deformation across the entire leaflet. Even without proteins, a bilayer experiences a balance of stresses: an interface between water and the hydrophobic tails is unfavorable, yet the disordered acyl tails favor lateral space. This is often manifest as a propensity to curve, or bend. When a leaflet experiences negative curvature, the space at the head-group region shrinks while that

of the tail region expands. Verifying the structure of the ordered phase is essential for revealing both the material and solvent properties of ordered phases.

Techniques that show nanometer-scale structure of dynamic phases are limited. Chemical cross-linking of biological-lipid mimics can determine the relative populations of nearest neighbors, and thus the interaction strength [116]. NMR can identify preferential interactions from the magnetization transfer between nearby lipids [117]. The advantage of scattering techniques is that they report correlations of nuclei beyond nearest neighbors, including at the nanometer scale. Furthermore, they do not require dyes or lipid modifications (beyond, perhaps, deuteration), and are not complicated by slowly interconverting populations, as is the case with NMR.

6.1.1 Low- q scattering is most sensitive to overall vesicle composition, which determines scattering contrast with solvent

Before providing a general estimate in the change in scattering due to a nanometer-scale inhomogeneity, the scattering of a general lipid vesicle will be broadly described. A key parameter is the average contrast between lipid and solvent, defined as \bar{b} below. For a bilayer without macroscopic phase separation but with nanoscale inhomogeneity, the concept of an average bilayer scattering length is relevant for q below the lengthscale, l , of the inhomogeneity, i.e., $q < \frac{2\pi}{l}$.

Consider a lipid system with solvent-adjusted neutron scattering density

$$\beta(\mathbf{r}) = \sum_i b_i \delta(\mathbf{r}_i) - \beta_s \quad (6.1)$$

where b_i is the neutron scattering length of atom i , $\delta(\mathbf{r})$ is the Dirac delta function, and β_s is the scattering length density of the solvent. For a flat patch of the bilayer, choose the bilayer normal to be oriented along z , with midplane at $z = 0$. Define the quantity \bar{b} by

$$\bar{b} = A_{\text{patch}}^{-1} \int_{\text{patch}} dA \int_{-\infty}^{\infty} dz \beta(\mathbf{r}). \quad (6.2)$$

The lower and upper bounds of the integral, here set as $-\infty/+∞$, need only extend into the region of bulk solvent before the integrand is zero. The value of \bar{b} for highly

curved regions, relevant for small vesicles, will be estimated below. For the immediate interest of a rough estimate of scattering from a large vesicle, the effect of curvature is small.

The quantity \bar{b} is readily available from a small molecular simulation of a planar bilayer, where the patch size is the periodically-replicated simulation cell. In this case, the integral over the patch is equivalent to *laterally-averaging* the scattering density. The quantity $\beta_{\text{LA}}(z)$, denoting the laterally-averaged solvent-subtracted scattering density along the bilayer normal, is defined in these terms. The value of \bar{b} can then be computed by integrating over z .

At low q , a vesicle scatters with intensity [24]

$$\bar{I}(q) = 2\pi\bar{b}^2 q^{-2} \sin(qR)^2 \quad (6.3)$$

where $\bar{I}(q)$ is the intensity per unit surface area and R is the radius of the vesicle. Here $\sin(qR)$ is the signature of the vesicle's size. Near $q = 0$ the vesicle scatters with constant intensity, like any finite scatterer. As q increases, but before $2\pi q^{-1}$ is comparable to the bilayer thickness, the magnitude of the oscillating signal decays as q^{-2} . This q^{-2} trend is a signature of the nearly two-dimensional surface.

6.1.2 High- q scattering is most sensitive to transverse structure

As $2\pi q^{-1}$ approaches the scale of the bilayer thickness, h , (i.e., $q > 0.2 \text{\AA}^{-1}$), a pattern emerges that predominantly shows the effect of scattering contrast across the normal of the bilayer, referred to here as the transverse direction. Compared with a single object with volume h^3 , the magnitude of the transverse scattering is enhanced by the geometry of the bilayer. The bilayer is flat over a lengthscale that is long relative to h , meaning that laterally spaced pairs of atoms scatter coherently over an area that goes as q^{-2} — their correlation adds constructively at the detector. With increasing q , the magnitude of the scattering intensity continues to scale as $\bar{b}^2 q^{-2}$.

6.1.3 The lateral signal is small compared to that of transverse structure

Lateral correlations do not benefit from the same dimensional enhancement as the transverse scattering. Each nanometer scale domain is essentially its own molecular species — with scattering that increases proportionally to the number of domains, without the benefit of the q^{-2} prefactor. Rather, the intensity is limited by the area of the domain itself, and unlike the transverse signal, fails to grow at q lower than L_{domain}^{-1} , where L_{domain} is the diameter of the nanoscale structure. At low q , the scattering from the nanoscale domain blends in with the overall bilayer scattering. That is, q is sufficiently low that neutrons view the bilayer as having a single scattering density, and the intensity takes on simply the asymptotic scattering in [eq. \(6.3\)](#).

In summary, the scattering from nanometer-scale structure of the bilayer is expected to display in intermediate ranges of q . The magnitude of the scattering is proportional to its area as well as the domain's contrast with solvent. In terms of signal-to-noise, it must compete with the scattering from the transverse structure, which scales as $\bar{b}^2 q^{-2}$. A key approach of this work is to vary the deuterated composition within the liquid-ordered phase to minimize \bar{b} , and thus enhance the relative intensity of the predicted nanometer-scale structure.

6.1.4 Precise modeling of both transverse and lateral scattering is critical

The SANS intensity is a combination of many different spatial correlations. The problem may be viewed as fitting the scattered intensity in terms of a parameterized scattering density. A challenge arises: the intensity is a squared function of the scattering density — sign information is lost. There does not exist a one-to-one mapping between structure and signal. Moreover, for vesicles and other freely rotating structures, the structure is orientationally averaged. For a model, this work uses all-atom molecular modeling, described in [chapter 3](#), in conjunction with the continuum model of vesicle shape, described in [chapter 5](#). Briefly, scattering is modeled at high q using a fully correlated treatment of pairs from the all-atom simulation. At low q , a continuum model is employed that deforms the molecularly-modeled neutron scattering length

density into the shape of a fluctuating vesicle. The two methods are stitched together, with loss of coupling of vesicle shape to fine molecular features.

6.2 Methods

6.2.1 Deuteration scheme and composition selection

The sample providing the most direct evidence for lateral structure was developed according to three criteria. First, it should be a single macroscopic phase; it should not contain a mixture of both the L_o and L_d phases. Such a mixture would appear to have massive lateral correlations due to the size of the domains themselves, and the transverse signal would not approach zero under any deuteration conditions. Second, there should be sufficient scattering contrast between the nanometer-scale inhomogeneities such that the lateral signal is detectable. Third, the overall scattering density of the bilayer should be close to contrast-matched with the solvent itself, to reduce the transverse intensity relative to the lateral intensity.

For the first criterion, five samples were prepared starting with 63% DPPC and 37% cholesterol, a liquid-ordered mixture. By gradually adding increasing amounts of DOPC to four of the samples, composition was scanned across what would eventually be a tie-line of the liquid-liquid coexistence region of DPPC/DOPC/chol. The five compositions tested are listed in [table 6.1](#) and plotted in [fig. 6.1](#). By identifying the emergence of a macroscopic disordered phase enriched in DOPC, and only considering samples outside the region, selection of a pure- L_o phase can be guaranteed. Small-angle

Table 6.1: Compositions Used to Determine L_o Tie-Line Endpoint, corresponding to the markers in [fig. 6.1](#).

| | DPPC | DOPC | Chol. |
|---|-------|-------|-------|
| A | 63.1% | 0.0% | 36.9% |
| B | 61.0% | 3.7% | 35.3% |
| C | 58.9% | 7.4% | 33.7% |
| D | 56.8% | 11.1% | 32.1% |
| E | 54.7% | 14.8% | 30.5% |

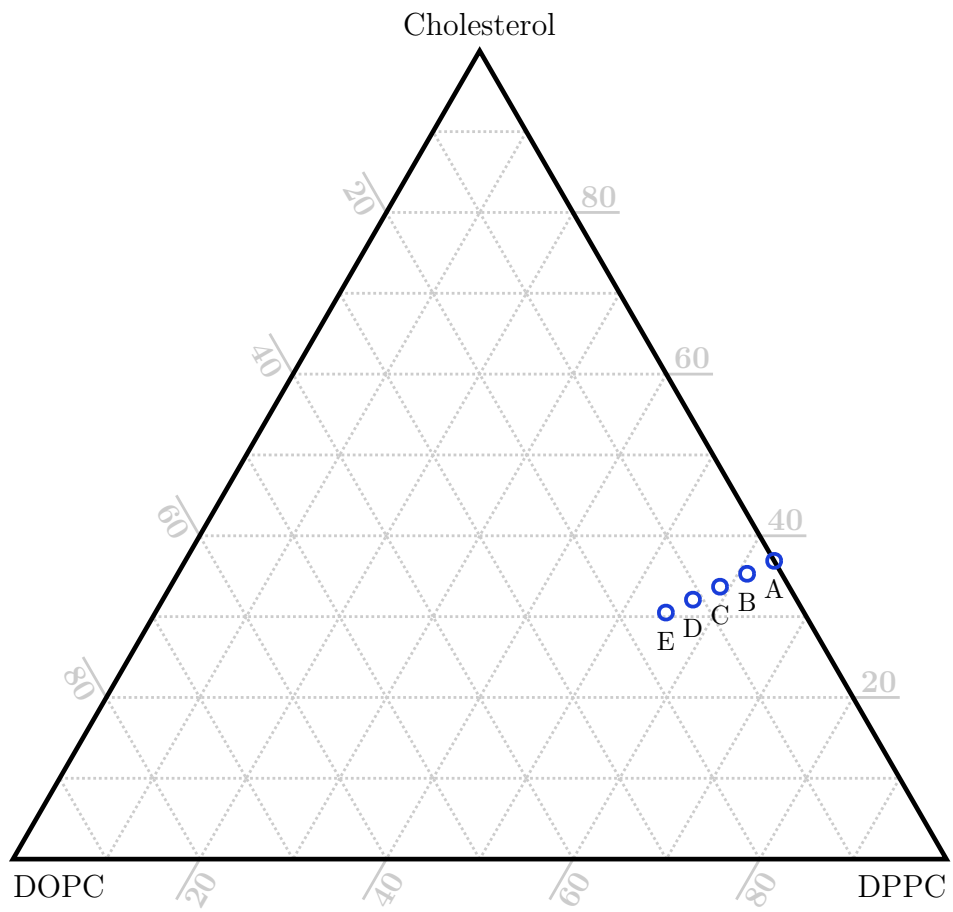


Figure 6.1: Small-Angle X-Ray Scattering Indicates the Boundary Between L_o and L_o/L_d Coexistence. The precise compositions are listed in [table 6.1](#).

X-ray scattering was used to localize the position of the tie-line endpoint to between 7.4% and 11.1% DOPC. The optimal composition for evidence of lateral structure will thus have less than 7.4% DOPC.

For the second and third criteria, nine additional samples of ca. 100nm diameter vesicles were prepared, spanning similar compositions to the previous five. The nine compositions are listed in [table 6.2](#) and plotted in [fig. 6.2](#). For these samples, DPPCd62 and chol.d41 were used with protiated DOPC to optimize lateral contrast. In this notation, “DPPCd62” indicates tail-deuterated DPPC, and “chol.d41” indicates cholesterol where, on average, 40 random hydrogen sites are deuterated, and where the hydroxyl site matches the deuteration percentage of the solvent. The solvent was 90% D₂O/10% H₂O. With the interstitial region enriched in the protiated DOPC, there should be high contrast between the hexagonally packed DPPC region, fulfilling the second criterion. Simulation models indicated that the solvent contrast matching condition would be achieved between the initial DPPC/cholesterol composition and the coexistence region, satisfying the third criterion.

Shown in [fig. 6.3](#) is the small-angle neutron scattering intensity, starting in the ordered phase, resulting from the nine steps in composition phase toward liquid-liquid coexistence. Structural features (i.e., dips in the intensity) are clear between $q = 0.01$ and $q = 0.1$ in the first four samples. Beyond these samples, the intensity takes on the characteristic q^{-2} of a thin surface. This simplicity of form is a natural consequence of the superposition of signals where structural features are canceled by scattering from a separate phase. On the basis of this, the optimal composition for evidence of lateral structure would be between the third (C) and fourth (D) samples, which contain more protiated DOPC expected to fill the interstitial zones of the L_o phase. Combined with the former constraint from the small-angle X-ray scattering results, a composition of 60.2% DPPC, 5.0% DOPC, and 34.8% cholesterol (composition C) was selected.

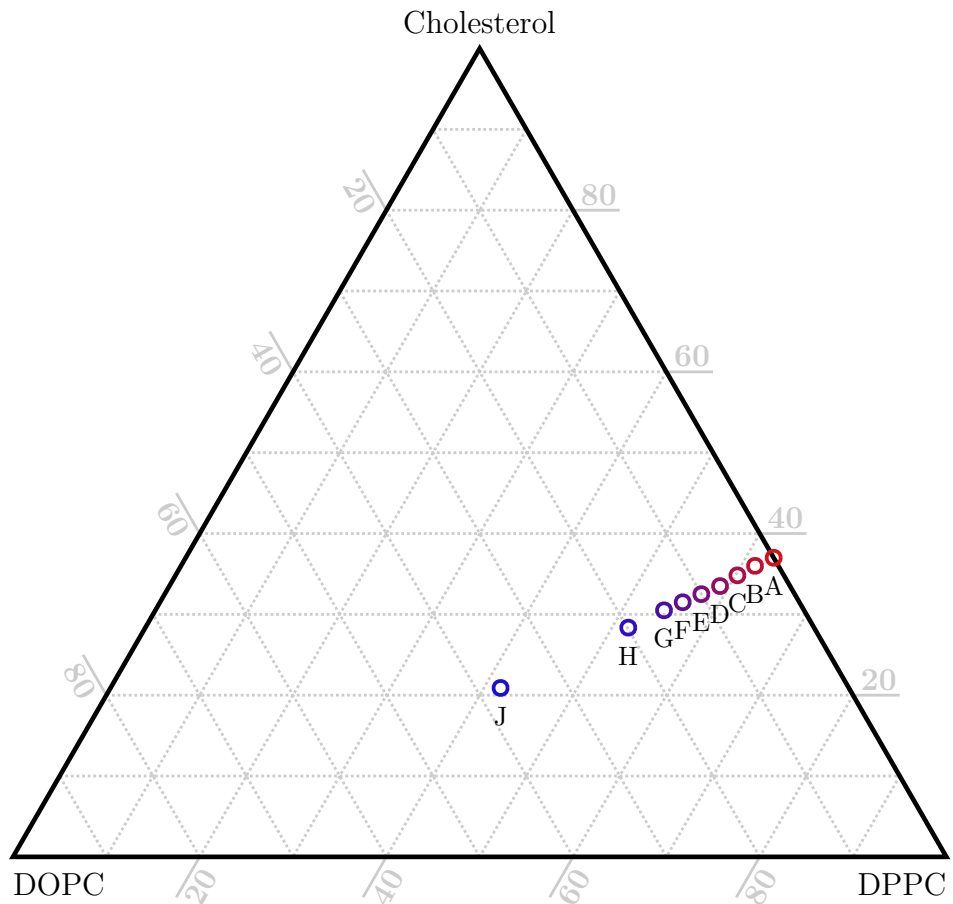


Figure 6.2: SANS Compositions Used to Determine Optimal L_o Composition. Colors have been chosen to correspond to the curves in [fig. 6.3](#). The precise compositions are listed in [table 6.2](#).

Table 6.2: SANS Compositions Used to Determine Optimal L_o Composition, corresponding to the markers in [fig. 6.2](#) and curves in [fig. 6.3](#). Composition labels do not match those in [table 6.1](#).

| | DPPC | DOPC | Chol. |
|---|-------|-------|-------|
| A | 63.0% | 0.0% | 37.0% |
| B | 61.5% | 2.5% | 36.0% |
| C | 60.2% | 5.0% | 34.8% |
| D | 59.0% | 7.5% | 33.5% |
| E | 57.5% | 10.0% | 32.5% |
| F | 56.0% | 12.5% | 31.5% |
| G | 54.5% | 15.0% | 30.5% |
| H | 51.7% | 19.9% | 28.4% |
| J | 41.8% | 37.3% | 20.9% |

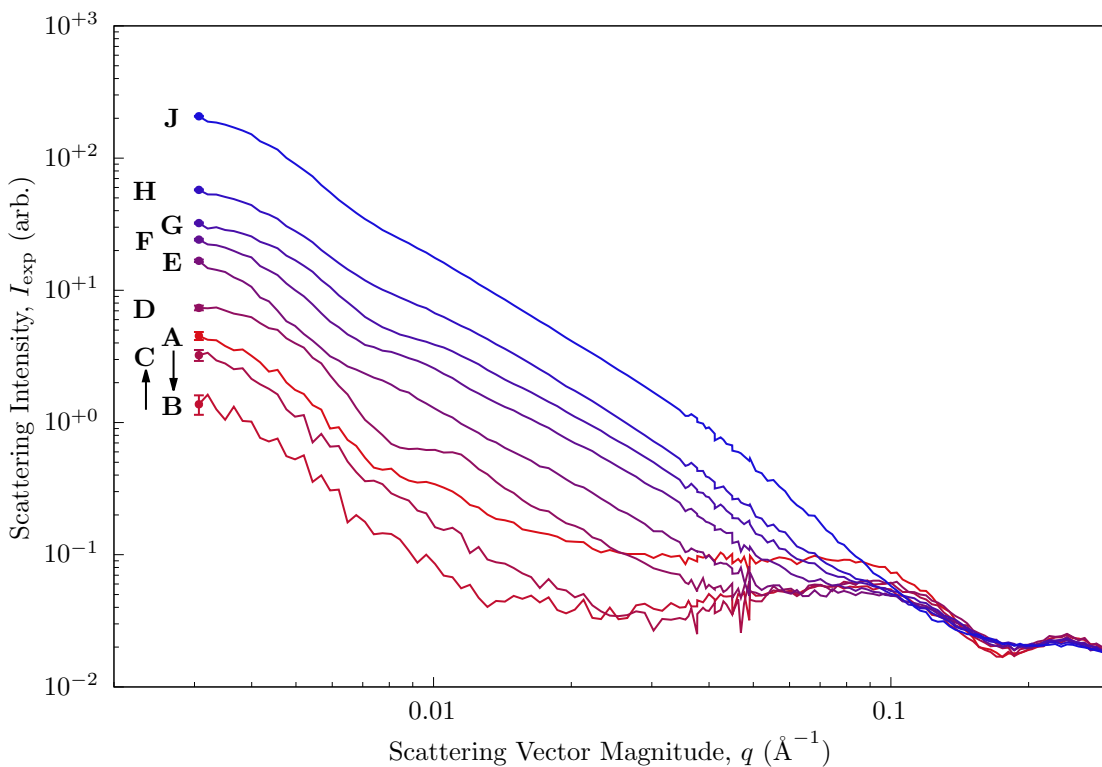


Figure 6.3: Experimental SANS Intensities, measured from the range of samples beginning from the DPPC/chol sample (**A**) and extending well into the L_o/L_d coexistence region (e.g., **J**). Colors have been chosen to correspond to the markers in [fig. 6.2](#). The compositions for each curve are listed in [table 6.2](#).

6.2.2 All-atom simulation

Equivalent systems were built and simulated using the CHARMM all-atom forcefield (C36) with approximately 200 lipids per leaflet and run for approximately 700 nanoseconds. These simulations were meant to directly target the experimental composition of the vesicle assuming each vesicle of the sample had the target lipid composition. Additionally, shorter (ca. 100 nanosecond) simulations were run over a very wide range of 57 total compositions, with DPPC ranging from 75% to 57.5%, DOPC from zero to 16.5%, and cholesterol ranging from 18.5% to 40% in lipid-per-leaflet increments of three. The specific compositions used are listed in [table 6.3](#) and plotted in [fig. 6.4](#). These simulations are combined to model a distribution of compositions in the experimental sample of vesicles.

6.3 Results: The SANS vesicle signal is reconstructed from combined molecular and continuum models

We model the complete scattering from a vesicle by combining molecular simulations with a continuum model. The laterally averaged scattering density β_{LA} is computed from all-atom simulation and is used to model long-range correlations where molecular details are not critical. The PFFT method is used to compute the scattering from the nanometer-scale inhomogeneity. Both contributions are required to model the whole scattering, such that the nanometer-scale features can be isolated.

PFFT is introduced as a correction to the laterally averaged scattering, $\bar{I}_{LA}(q)$ for planar systems:

$$\Delta\bar{I}_{PFFT}(q) = \bar{I}_{PFFT}(q) - \bar{I}_{LA}(q), \quad (6.4)$$

where $\bar{I}_{PFFT}(q)$ is the scattering, per bilayer unit area, computed from PFFT. This correction is then added to the scattering of the dynamically fluctuating vesicle that lacks nanometer-scale structure, $I_{DS,LA}(q)$ (where here ‘DS’ stands for dynamic structure, while ‘LA’ refers to the use of the laterally-averaged scattering for transverse structure). This framework currently is unable to provide correlations from vesicle shape with the structure of the nanometer-scale inhomogeneity. However, these two effects are not

Table 6.3: Compositions Used for Compositional Fitting. TODO: Caption here

| DPPC | DOPC | Chol. | DPPC | DOPC | Chol. | DPPC | DOPC | Chol. |
|-------|-------|-------|-------|-------|-------|-------|-------|-------|
| 57.5% | 0.0% | 42.5% | 62.5% | 4.5% | 33.0% | 67.5% | 3.0% | 29.5% |
| 57.5% | 1.5% | 41.0% | 62.5% | 6.0% | 31.5% | 67.5% | 4.5% | 28.0% |
| 57.5% | 3.0% | 39.5% | 62.5% | 7.5% | 30.0% | 67.5% | 6.0% | 26.5% |
| 57.5% | 4.5% | 38.0% | 62.5% | 9.0% | 28.5% | 67.5% | 7.5% | 25.0% |
| 57.5% | 6.0% | 36.5% | 62.5% | 10.5% | 27.0% | 67.5% | 9.0% | 23.5% |
| 57.5% | 7.5% | 35.0% | 65.0% | 0.0% | 35.0% | 67.5% | 10.5% | 22.0% |
| 57.5% | 9.0% | 33.5% | 65.0% | 1.5% | 33.5% | 67.5% | 12.0% | 20.5% |
| 57.5% | 10.5% | 32.0% | 65.0% | 3.0% | 32.0% | 67.5% | 13.5% | 19.0% |
| 60.0% | 0.0% | 40.0% | 65.0% | 4.5% | 30.5% | 67.5% | 15.0% | 17.5% |
| 60.0% | 1.5% | 38.5% | 65.0% | 6.0% | 29.0% | 67.5% | 16.5% | 16.0% |
| 60.0% | 3.0% | 37.0% | 65.0% | 7.5% | 27.5% | 70.0% | 0.0% | 30.0% |
| 60.0% | 4.5% | 35.5% | 65.0% | 9.0% | 26.0% | 70.0% | 1.5% | 28.5% |
| 60.0% | 6.0% | 34.0% | 65.0% | 10.5% | 24.5% | 70.0% | 3.0% | 27.0% |
| 60.0% | 7.5% | 32.5% | 65.0% | 12.0% | 23.0% | 72.5% | 0.0% | 27.5% |
| 60.0% | 9.0% | 31.0% | 65.0% | 13.5% | 21.5% | 72.5% | 1.5% | 26.0% |
| 60.0% | 10.5% | 29.5% | 65.0% | 15.0% | 20.0% | 72.5% | 3.0% | 24.5% |
| 62.5% | 0.0% | 37.5% | 65.0% | 16.5% | 18.5% | 75.0% | 0.0% | 25.0% |
| 62.5% | 1.5% | 36.0% | 67.5% | 0.0% | 32.5% | 75.0% | 1.5% | 23.5% |
| 62.5% | 3.0% | 34.5% | 67.5% | 1.5% | 31.0% | 75.0% | 3.0% | 22.0% |

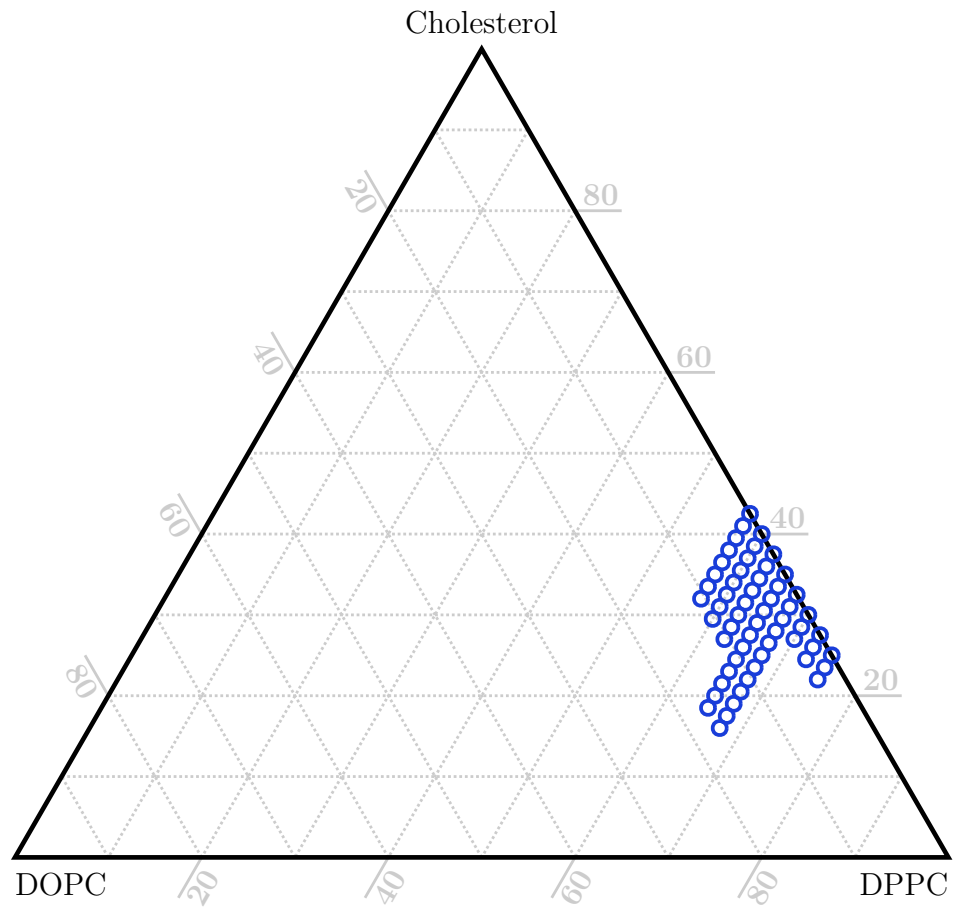


Figure 6.4: Compositions Used for Compositional Fitting. TODO: add another caption

expected to couple strongly to the intensity given the large separation of length-scales. The approach is largely equivalent to subtracting $I_{\text{DS,LA}}(q)$ from $I_{\text{exp}}(q)$ and comparing to $\Delta \bar{I}_{\text{PFFT}}(q)$. $I_{\text{DS,LA}}(q)$ is computed using the method developed in Ref. [47].

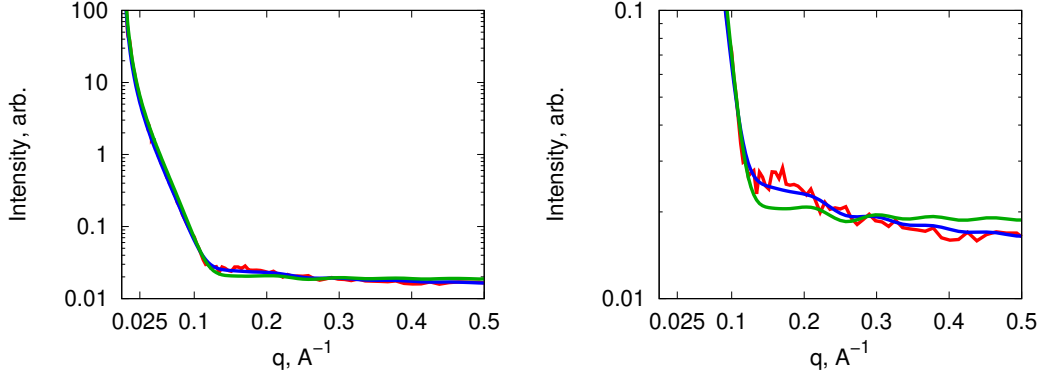
6.4 Intramolecular correlations of deuteration contribute to scattering

A simple bilayer composed of equal parts acyl-chain deuterated and acyl-chain protiated DPPC will exhibit apparent scattering in excess of the laterally averaged approximation. For the most part, this is due to spatial correlations created by the chemical correlations of deuterium and protium. That is, if at one position on a chain there is a deuterium, the rest of the *laterally nearby* chain will be deuterated as well. This intramolecular correlation is not taken into account when laterally averaging, in which this information is lost. The difference between the two intensities is shown in fig. 6.5. The PFFT method produces a qualitatively better match to the experimental intensity.

6.4.1 Experimental distributions of the L_o phase composition and size

If the mixing of lipids of extruded vesicles were ideal the variation of composition would be purely stochastic. If the area per lipid is on the order of 65 \AA^2 , there are approximately $N = 10^5$ lipids in the vesicle. For a lipid-type with fraction f , the binomial distribution indicates the lipid-counts on a *per-vesicle* basis will have variance $Nf(1-f)$. For this 100 nm diameter vesicle, with a minority lipid nominally at 5%, this will result in $\pm 0.1\%$ expected deviation. Clearly, perfectly ideal mixing is inconsistent with the overall hypothesis of this work. Ibarguren et al. found that for many mixtures the extruded cholesterol content was lower than intended (pre-hydration), although with moderate cholesterol levels the incorporation was within a few percent [118]. Given the possibility of a variation in compositional distribution, the sensitivity of the conclusions to variations and distributions in the composition are tested here.

Extrusion through a particularly sized pore results in a distribution of vesicle sizes; they are polydisperse. Kunding et al. have developed a fluorescence-based assay



(a) Zooming out to show the complete (b) Zooming into the relevant intensity range of intensity. range for comparison.

Figure 6.5: Comparison of Experimental Scattering with PFFT and Lateral Averaging.

for vesicle size distribution that compares well with precision electron microscopy. They found that extrusion through 100 nm and 200 nm eliminated large vesicles, but naturally left large populations of small vesicles. In this work we use the distribution

$$G(R) = \left(\frac{z+1}{R_m} \right)^{z+1} \frac{R^z}{\Gamma(z+1)} e^{-\frac{R(z+1)}{R_m}}, \quad (6.5)$$

where R_m is the average vesicle radius, and z represents the width of the distribution. This includes the contribution from small vesicles. The distribution $G(R)$ has standard deviation $\frac{R_m}{\sqrt{1+z}}$.

6.4.2 The best-fit match to molecular simulation indicates nanometer-scale structure

In fig. 6.6, the intensity of the laterally-averaged and PFFT methods is compared with experiment. For comparison, the simulated intensities were fit by a scalar and shifted by a constant to represent the unknown total amount of material and incoherent scattering, respectively.

In fig. 6.7, the intensity is computed as a linear superposition of the PFFT or laterally-averaged intensity from a range of the 57 lipid compositions mentioned above. Additionally, a constant is added to the intensity to represent incoherent scattering. The weights of the simulations are determined from a non-negative least squares fitting

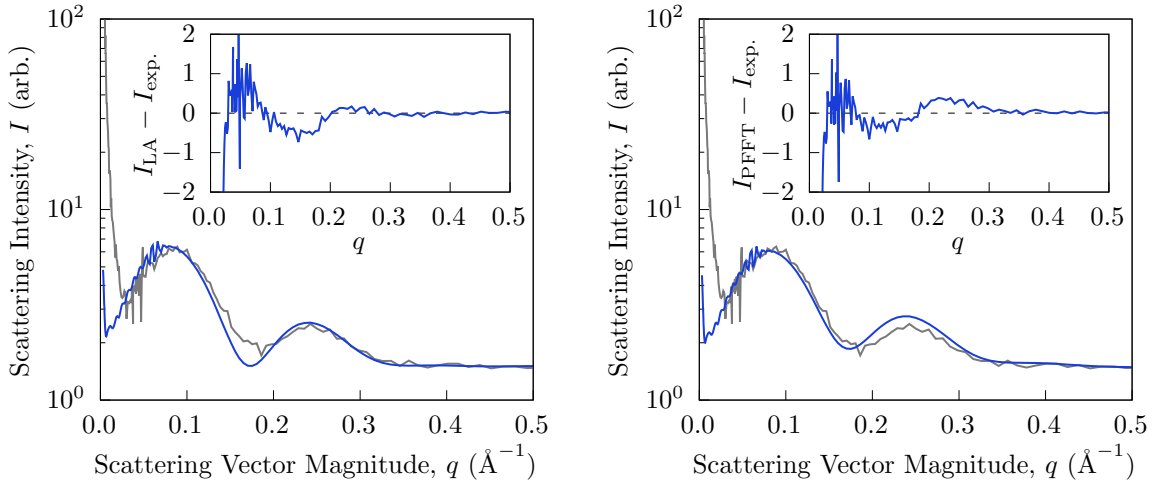


Figure 6.6: Comparison of Experimental Liquid-Ordered Scattering with Single-Composition PFFT and Lateral Averaging. The experimental data is plotted in grey, while the model is plotted in blue.

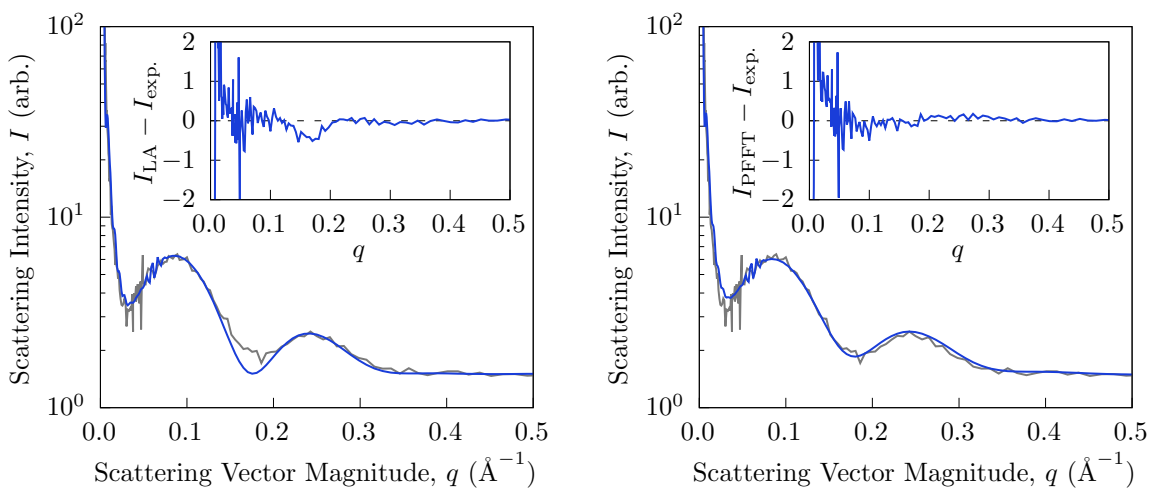


Figure 6.7: Comparison of Experimental Liquid-Ordered Scattering with Multi-Composition PFFT and Lateral Averaging. The experimental data is plotted in grey, while the model is plotted in blue.

algorithm. Typical of such fits, all but three (laterally-averaged) or four (PFFT) of the 57 weights are set to zero.

For these simulations, which we seek to build as the gold-standard for matching all-atom simulations to experiment, we employed a Helfrich continuum model of a vesicle fluctuation. To evaluate the three-dimensional scattering length density, we use the laterally-averaged $\beta(z)$ where z is the distance along the normal from the surface. To include an estimate from PFFT, we added to the continuum model the difference between PFFT and laterally averaged for a planar system. This method includes the near-field particle correlations of PFFT while employing the laterally-averaged scattering density to evaluate the shape effects of the vesicle.

For the liquid-ordered phase, the PFFT method produces a qualitatively better match to the experimental intensity.

6.5 Discussion and conclusions

The outer leaflet of the plasma membrane of mammalian cells is enriched in sphingolipids and cholesterol[58], in a ratio that forms a liquid ordered phase in model systems. Simulations of these mixtures have shown the L_o phase to be itself inhomogeneous, with nanoscale domains of mostly trans, hexagonally packed acyl chains interspersed with regions enriched in unsaturated chains and cholesterol [78, 23]. If verified experimentally, the heterogeneous structure of the L_o phase has significant implications for the biophysical properties of the outer leaflet, including partitioning and organization of membrane proteins and membrane curvature [46].

In this work the hexagonal substructure of the L_o phase is confirmed by integrated analysis of all-atom simulations and small-angle neutron scattering. A recently developed method for prediction of SANS intensity from simulation data [24] was used to discriminate the signal of the substructure from the (typically much stronger) transverse signal. Guided by the simulations, a carefully selected deuteration scheme optimized the signal from the lateral substructure, and comparison of the simulated and measured intensity confirmed the presence of hexagonally packed chains in the

L_o phase. In addition, the quantitative comparison of the scattering and simulation data led to the discovery that previously published boundaries of the miscibility loop required revision, which was confirmed by small-angle x-ray scattering. The integrated approach developed here should be useful for other problems for which cases lateral organization of a membrane sample is of interest, especially when the detection of the lateral signal is confounded by transverse scattering, and when the signal appears at q values corresponding to only a few molecular diameters. It remains an open question whether the outer leaflet of the plasma membrane is L_o -like. However, the model of the L_o phase put forth previously [78, 23] and confirmed here posits that there is more to the L_o phase than chain order and fluidity — the nanoscale hexagonal packing of saturated hydrocarbon is an essential feature of the L_o phase. Determining the presence or absence of substructure in more physiological mixtures will be an important step in the biophysical characterization of living membranes.

Chapter 7

CONCLUSION

The developments described in [chapters 3 to 6](#) can be summarized into three main advancements. First, two new computational methods were created to retain lateral contributions when computing neutron scattering intensities from simulated lipid bilayers. Second, a technique was developed which adapts planar simulation data to model high-curvature systems. And third, these advancements were used to probe for a previously undetected nanoscale structure within experimental systems of the liquid-ordered phase.

7.1 Lateral scattering contributions to neutron scattering intensity

Prior to this work, the status quo for comparing molecular dynamics simulations to experimental neutron scattering intensities was to laterally average the simulation data. The primary contributions to the scattering intensity often arise from transverse scattering length density variations. In systems where lateral structure is not expected at the lengthscales of interest, an adequate approximation can be achieved by laterally averaging the simulation, such that only the transverse structure is modeled. However, this approximation does not hold for systems where lateral structures form significant contributions to the scattering intensity.

Two new methods were described in [chapter 3](#) to rectify this issue. The Dirac Brush method is a mathematical approach which fully models the lateral periodic boundary conditions present in molecular dynamics simulations. The second method, PFFT, makes a mean-field approximation by including full 3D scattering contributions within a tunable cutoff distance, outside of which a laterally-averaged continuum model is used to prevent spurious contributions from the simulation's periodic images.

Both methods were validated against a set of coarse-grained molecular dynamics simulations ([chapter 4](#)) which were constructed to be indistinguishable to existing lateral averaging techniques. For a system without lateral structures, the scattering intensities produced by the Dirac Brush method and PFFT agree with those from the existing laterally averaged methods. Furthermore, both methods successfully distinguished between the coarse-grained simulations by including contributions from lateral structure.

The mathematically exact nature of the Dirac Brush method, and particularly the lack of any computational distinction between transverse and lateral scattering contributions, suggests that the Dirac Brush method should be equally accurate modeling any such quasi-two-dimensional system. The validation against existing techniques, using a system without lateral structure, then strongly supports the overall accuracy of the technique. However, modelling a molecular dynamic simulation's periodic boundaries establishes a periodicity which is not representative of experimental systems. This numerically-exact periodicity produces very narrow Bragg artifacts in the scattering intensity. These artifacts are narrow enough to insignificantly affect some quantitative fitting strategies, but they are visually distracting and may qualitatively obscure finer details of the scattering intensity.

PFFT avoids the artifacts by modeling only the transverse contributions at distances greater than the chosen cutoff, while modeling full 3D contributions at the shorter distances. It is successfully validated against the existing laterally-averaged techniques for systems without lateral structure and against the Dirac Brush method for systems with lateral structure, establishing overall accuracy for these systems. However, the appropriate cutoff distance must be chosen carefully to be large enough to include contributions from the desired lateral structures while also small enough to avoid spurious contributions from the simulation's periodic boundaries. It is necessary to consider the expected size of lateral features when designing the molecular dynamic simulation itself, so requiring these same considerations for tuning PFFT should not be a significant burden upon users.

For either technique, there are a few directions future endeavors might take, which build upon the new ability to model systems with significant lateral contributions. The new methods may be directly applied to all-atom simulations for comparison to experimental bilayers. Simulations of more complex lipid mixtures which model biological membrane compositions can then be used to probe for nanoscale structural features inaccessible to traditional fluorescence microscopy techniques. Both techniques might also be reworked to model systems with a different dimensionality, such as quasi-one-dimensional thread-like structures which are periodic in only one direction. In general, the techniques as-presented can be used to validate simulations against any experimental planar or low-curvature membrane system. The curvature limitation might be explored through simulations of entire coarse-grained vesicles of various sizes. Comparisons between the scattering intensities from these simulations to that of an infinite planar system would yield insights regarding the minimum vesicle size for which a planar system is still a good approximation.

7.2 Adjusting for high curvature

For experimental samples consisting of very small vesicles, the technique described in [chapter 5](#) is needed to adjust the physical properties of a planar system to better match the high-curvature geometry. In this technique, the transverse scattering length density is distorted to maintain a constant bilayer volume. The head groups of lipids in the outer leaflet are laterally expanded and transversely compressed, and vice versa for the tail groups of the same lipids. These expansions and compressions affect the scattering length density, and can be modeled geometrically. The geometric model is combined with a transverse scattering length density profile, as measured from a planar molecular dynamics simulation, and mapped over an arbitrary surface to define the scattering length density at all points in 3D space.

The high-curvature adjustments were validated using coarse-grained models. Two coarse-grained vesicles were simulated at diameters of 13nm and 18nm, and the full 3D scattering intensity was computed for each of these vesicles. A planar coarse-grained

simulation was then used to build the high-curvature models for comparison to these intensities. The accuracy of the model was excellent in both cases, but it indicated unexpected tension in the outer leaflets of the vesicles.

The preparation of the coarse-grained vesicles used a stage in which the membrane was perforated in six places to both alleviate osmotic pressure and equalize tension between the two leaflets. Future comparisons with larger coarse-grained vesicles might confirm that the observed outer leaflet tension is an artifact of this construction procedure. Alternatively, the number of pores might be varied to see if this affects the outer leaflet tension. Directly measuring the tension of each leaflet is nontrivial, but comparing the scattering characteristics of various constructions against the planar-simulation-derived geometric model might help to refine those procedures to more reliably relax the leaflets.

Another avenue of future work may be to reintroduce lateral structures to the geometric model. One approach might adapt PFFT by mapping the full 3D scattering length density (including lateral variations) over a small region of the high-curvature surface, using similar geometric adjustments based on local curvature. The rest of the surface would receive the continuum model of the scattering length density as already demonstrated. If computed such that the full-3D region is a moving window centered on each sampled point on the surface, as is described in the planar PFFT method, the topological issues of mapping a rectangular patch onto a closed surface will be avoided.

For comparison to experiment, the high-curvature vesicle model can be applied to an all-atom planar simulation. All-atom simulations more closely reproduce the physical characteristics of experimental systems, facilitating a more direct fit to the experimental scattering intensity.

7.3 Putting it together: searching for substructure

The liquid-ordered phase of model membranes is an ideal candidate for demonstrating the utility of the aforementioned techniques. Simulations of the liquid-ordered

phase indicated regions of hexagonally packed saturated hydrocarbon chains and cholesterol. This lateral structure prevents prior laterally-averaged techniques from accurately modeling the scattering intensity. Furthermore, the experiments were conducted on solutions of vesicles. All-atom vesicle simulations are impractical with current computing resources, and coarse-grained simulations may not reproduce the nuanced molecular interactions responsible for the lateral substructure observed in the all-atom simulations.

As described in [chapter 6](#), PFFT was used to model the lateral scattering contributions to the scattering intensity. While not truly independent, the transverse contributions were subtracted from PFFT to isolate the lateral contributions. The high-curvature technique was used to model the transverse contributions, while accounting for the curvature of the vesicle and local transient curvature induced by dynamic fluctuations of the vesicle shape. The curvature-adjusted transverse contributions were then combined with the PFFT-derived lateral contributions to produce a cohesive scattering intensity model for comparison to the experimental data. As a control, the transverse contributions alone (without PFFT) were also compared to the experimental data.

The model with lateral contributions matched the experimental data better than the model without lateral contributions, supporting the existence of lateral structure. The close agreement between simulation and experiment strongly implies the existence of the hexagonal substructures within experimental vesicles of the liquid-ordered phase.

The composition of biological membranes is much more complex than the liquid-ordered phase studied here. However, similarities in composition to the liquid-ordered phase imply that similar nanoscale substructures are possible. Through all-atom planar simulations of more complex mixtures and scattering intensity computations using PFFT with the high-curvature adjustments, the signature of such hexagonally-packed substructures may be investigated in experimental vesicles. The same procedure may be extended to other forms of substructure, in that they may be directly observed in simulation and then probed experimentally via neutron scattering. The ultimate objective of this entire work is to establish integrated techniques to help develop a

more complete understanding of the complex lipid mixtures in biological membranes, including the presence or absence of nanoscale substructures.

BIBLIOGRAPHY

- [1] Bruce Albert. Molecular biology of the cell, 2008.
- [2] Julio L Sampaio, Mathias J Gerl, Christian Klose, Christer S Ejsing, Hartmut Beug, Kai Simons, and Andrej Shevchenko. Membrane lipidome of an epithelial cell line. *Proceedings of the National Academy of Sciences*, 108(5):1903–1907, 2011.
- [3] Gerrit Van Meer, Dennis R Voelker, and Gerald W Feigenson. Membrane lipids: where they are and how they behave. *Nature reviews Molecular cell biology*, 9(2):112–124, 2008.
- [4] Frederick A Heberle and Gerald W Feigenson. Phase separation in lipid membranes. *Cold Spring Harbor perspectives in biology*, 3(4):a004630, 2011.
- [5] Sarah L. Veatch and Sarah L. Keller. Separation of Liquid Phases in Giant Vesicles of Ternary Mixtures of Phospholipids and Cholesterol. *Biophysical Journal*, 85(5):3074–3083, 2003.
- [6] T Parasassi, G De Stasio, A d’Ubaldo, and E Gratton. Phase fluctuation in phospholipid membranes revealed by Laurdan fluorescence. *Biophysical journal*, 57(6):1179–1186, 1990.
- [7] Margus R Vist and James H Davis. Phase equilibria of cholesterol/dipalmitoylphosphatidylcholine mixtures: deuterium nuclear magnetic resonance and differential scanning calorimetry. *Biochemistry*, 29(2):451–464, 1990.
- [8] J Hjort Ipsen, G Karlström, OG Mourtisen, H Wennerström, and MJ Zuckermann. Phase equilibria in the phosphatidylcholine-cholesterol system. *Biochimica et Biophysica Acta (BBA)-Biomembranes*, 905(1):162–172, 1987.
- [9] Sarah L Veatch and Sarah L Keller. Seeing spots: complex phase behavior in simple membranes. *Biochimica et Biophysica Acta (BBA)-Molecular Cell Research*, 1746(3):172–185, 2005.
- [10] Jeffery B. Klauda, Richard M. Venable, J. Alfredo Freites, Joseph W. O’Connor, Douglas J. Tobias, Carlos Mondragon-Ramirez, Igor Vorobyov, Alexander D. MacKerell, and Richard W. Pastor. Update of the CHARMM All-Atom Additive Force Field for Lipids: Validation on Six Lipid Types. *Journal of Physical Chemistry B*, 114(23):7830–7843, 2010.

- [11] Jay W Ponder and David A Case. Force fields for protein simulations. In *Advances in protein chemistry*, volume 66, pages 27–85. Elsevier, 2003.
- [12] Maria M Reif, Philippe H Hünenberger, and Chris Oostenbrink. New interaction parameters for charged amino acid side chains in the GROMOS force field. *Journal of chemical theory and computation*, 8(10):3705–3723, 2012.
- [13] E Egberts and HJC Berendsen. Molecular dynamics simulation of a smectic liquid crystal with atomic detail. *The Journal of chemical physics*, 89(6):3718–3732, 1988.
- [14] Max L Berkowitz and K Raghavan. Computer simulation of a water/membrane interface. *Langmuir*, 7(6):1042–1044, 1991.
- [15] Howard E Alper, Donna Bassolino, and Terry R Stouch. Computer simulation of a phospholipid monolayer-water system: The influence of long range forces on water structure and dynamics. *The Journal of chemical physics*, 98(12):9798–9807, 1993.
- [16] Siewert Jan Marrink, Max Berkowitz, and Herman JC Berendsen. Molecular dynamics simulation of a membrane/water interface: the ordering of water and its relation to the hydration force. *Langmuir*, 9(11):3122–3131, 1993.
- [17] Erik Lindahl and Olle Edholm. Mesoscopic undulations and thickness fluctuations in lipid bilayers from molecular dynamics simulations. *Biophysical journal*, 79(1):426–433, 2000.
- [18] Alexander M Smolyrev and Max L Berkowitz. Structure of dipalmitoylphosphatidylcholine/cholesterol bilayer at low and high cholesterol concentrations: molecular dynamics simulation. *Biophysical Journal*, 77(4):2075–2089, 1999.
- [19] Edward Lyman and Sandeep Patel. Molecular Dynamics of Lipid Bilayers. *Liposomes, Lipid Bilayers and Model Membranes: From Basic Research to Application*, page 69, 2014.
- [20] Ira R Cooke, Kurt Kremer, and Markus Deserno. Tunable generic model for fluid bilayer membranes. *Physical Review E*, 72(1):011506, 2005.
- [21] Siewert J Marrink, H Jelger Risselada, Serge Yefimov, D Peter Tieleman, and Alex H De Vries. The MARTINI force field: coarse grained model for biomolecular simulations. *The journal of physical chemistry B*, 111(27):7812–7824, 2007.
- [22] Alexander J Sodt, Michael Logan Sandar, Klaus Gawrisch, Richard W Pastor, and Edward Lyman. The molecular structure of the liquid-ordered phase of lipid bilayers. *Journal of the American Chemical Society*, 136(2):725–732, 2014.

- [23] Alexander J Sodt, Richard W Pastor, and Edward Lyman. Hexagonal substructure and hydrogen bonding in liquid-ordered phases containing palmitoyl sphingomyelin. *Biophysical journal*, 109(5):948–955, 2015.
- [24] M. W. Dorrell, F. A. Heberle, J. Katsaras, L. Maibaum, E. Lyman, and A. J. Sodt. Laterally resolved small-angle scattering intensity from lipid bilayer simulations: an exact and a limited-range treatment. under review, 2020.
- [25] Walter Friedrich, Paul Knipping, and Max Laue. Interferenzerscheinungen bei roentgenstrahlen. *Annalen der Physik*, 346(10):971–988, 1913.
- [26] CG Shull and EO Wollan. X-ray, electron, and neutron diffraction. *Science*, 108(2795):69–75, 1948.
- [27] Bernard Dennis Cullity. *Elements of X-ray Diffraction*. Addison-Wesley Publishing, 1956.
- [28] Frederick A Heberle, Jianjun Pan, Robert F Standaert, Paul Drazba, Norbert Kučerka, and John Katsaras. Model-based approaches for the determination of lipid bilayer structure from small-angle neutron and X-ray scattering data. *European Biophysics Journal*, 41(10):875–890, 2012.
- [29] Deviderjit Singh Sivia. *Elementary scattering theory: for X-ray and neutron users*. Oxford University Press, 2011.
- [30] PB Moore, DM Engelman, and BP Schoenborn. Asymmetry in the 50S ribosomal subunit of Escherichia coli. *Proceedings of the National Academy of Sciences*, 71(1):172–176, 1974.
- [31] William T Heller, Volker S Urban, Gary W Lynn, Kevin L Weiss, Hugh M O'Neill, Sai Venkatesh Pingali, Shuo Qian, Kenneth C Littrell, Yuri B Melnichenko, Michelle V Buchanan, et al. The Bio-SANS instrument at the high flux isotope reactor of Oak Ridge National Laboratory. *Journal of Applied Crystallography*, 47(4):1238–1246, 2014.
- [32] Frederick A Heberle, Robin S Petruzielo, Jianjun Pan, Paul Drazba, Norbert Kučerka, Robert F Standaert, Gerald W Feigenson, and John Katsaras. Bilayer thickness mismatch controls domain size in model membranes. *Journal of the American Chemical Society*, 135(18):6853–6859, 2013.
- [33] Varley F Sears. Neutron scattering lengths and cross sections. *Neutron news*, 3(3):26–37, 1992.
- [34] Yongtian Luo and Lutz Maibaum. Relating the structure factors of two-dimensional materials in planar and spherical geometries. *Soft matter*, 14(27):5686–5692, 2018.

- [35] Mitchell Dorrell and Alexander J. Sodt. Source code for PFFT and Brush software. https://github.com/alexsdot/PFFT_Brush, 2020.
- [36] Tatyana M Konyakhina, Shih Lin Goh, Jonathan Amazon, Frederick A Heberle, Jing Wu, and Gerald W Feigenson. Control of a nanoscopic-to-macroscopic transition: modulated phases in four-component DSPC/DOPC/POPC/Chol giant unilamellar vesicles. *Biophysical journal*, 101(2):L8–L10, 2011.
- [37] Clare L Armstrong, MA Barrett, L Toppozini, N Kučerka, Z Yamani, John Katsaras, Giovanna Fragneto, and Maikel C Rheinstädter. Co-existence of gel and fluid lipid domains in single-component phospholipid membranes. *Soft Matter*, 8(17):4687–4694, 2012.
- [38] Mark James Abraham, Teemu Murtola, Roland Schulz, Szilárd Pál, Jeremy C Smith, Berk Hess, and Erik Lindahl. GROMACS: High performance molecular simulations through multi-level parallelism from laptops to supercomputers. *SoftwareX*, 1:19–25, 2015.
- [39] Svetlana Baoukina, Dmitri Rozmanov, and D Peter Tieleman. Composition fluctuations in lipid bilayers. *Biophysical journal*, 113(12):2750–2761, 2017.
- [40] Shushan He and Lutz Maibaum. Identifying the onset of phase separation in quaternary lipid bilayer systems from coarse-grained simulations. *The Journal of Physical Chemistry B*, 122(14):3961–3973, 2018.
- [41] Clare L Armstrong, Drew Marquardt, Hannah Dies, Norbert Kučerka, Zahra Yamani, Thad A Harroun, John Katsaras, An-Chang Shi, and Maikel C Rheinstädter. The observation of highly ordered domains in membranes with cholesterol. *PLoS One*, 8(6), 2013.
- [42] Jan-Michael Y Carrillo, John Katsaras, Bobby G Sumpter, and Rana Ashkar. A computational approach for modeling neutron scattering data from lipid bilayers. *Journal of chemical theory and computation*, 13(2):916–925, 2017.
- [43] Scott P Rayermann, Glennis E Rayermann, Caitlin E Cornell, Alexey J Merz, and Sarah L Keller. Hallmarks of reversible separation of living, unperturbed cell membranes into two liquid phases. *Biophysical journal*, 113(11):2425–2432, 2017.
- [44] Jonathan D Nickels, Sneha Chatterjee, Christopher B Stanley, Shuo Qian, Xiaolin Cheng, Dean AA Myles, Robert F Standaert, James G Elkins, and John Katsaras. The in vivo structure of biological membranes and evidence for lipid domains. *PLoS biology*, 15(5):e2002214, 2017.
- [45] Jonathan D Nickels, Xiaolin Cheng, Barmak Mostofian, Christopher Stanley, Benjamin Lindner, Frederick A Heberle, Stefania Perticaroli, Mikhail Feygenson, Takeshi Egami, Robert F Standaert, et al. Mechanical properties of nanoscopic

- lipid domains. *Journal of the American Chemical Society*, 137(50):15772–15780, 2015.
- [46] AJ Sodt, RM Venable, E Lyman, and RW Pastor. Nonadditive compositional curvature energetics of lipid bilayers. *Physical review letters*, 117(13):138104, 2016.
- [47] M. W. Dorrell, A. H. Beaven, and A. J. Sodt. A combined molecular/continuum-modeling approach to predict the small-angle neutron scattering of curved membranes. under review, 2020.
- [48] Harden M. McConnell and Marija Vrljic. Liquid-liquid immiscibility in membranes. *Annual Review of Biophysics and Biomolecular Structure*, 32(1):469–492, 2003.
- [49] Michael Seul and David Andelman. Domain shapes and patterns: The phenomenology of modulated phases. *Science*, 267(5197):476–483, 1995.
- [50] P. B. Sunil Kumar, G. Gompper, and R. Lipowsky. Modulated phases in multi-component fluid membranes. *Physical Review E - Statistical Physics, Plasmas, Fluids, and Related Interdisciplinary Topics*, 1999.
- [51] Jiang Zhao, Jing Wu, Frederick A. Heberle, Thalia T. Mills, Paul Klawitter, Grace Huang, Greg Costanza, and Gerald W. Feigenson. Phase studies of model biomembranes: Complex behavior of DSPC/DOPC/Cholesterol. *Biochimica et Biophysica Acta - Biomembranes*, 1768(11):2764–2776, 2007.
- [52] Frederick A. Heberle, Jing Wu, Shih Lin Goh, Robin S. Petruzielo, and Gerald W. Feigenson. Comparison of three ternary lipid bilayer mixtures: FRET and ESR reveal nanodomains. *Biophysical Journal*, 99(10):3309–3318, 2010.
- [53] Jianbing Zhang, Bingwen Jing, Nobuya Tokutake, and Steven L. Regen. Transbilayer complementarity of phospholipids. A look beyond the fluid mosaic model. *Journal of the American Chemical Society*, 126(35):10856–10857, 2004.
- [54] Jason D. Perlmutter and Jonathan N. Sachs. Interleaflet interaction and asymmetry in phase separated lipid bilayers: Molecular dynamics simulations. *Journal of the American Chemical Society*, 133(17):6563–6577, 2011.
- [55] Philip W. Fowler, John J. Williamson, Mark S.P. Sansom, and Peter D. Olmsted. Roles of Interleaflet Coupling and Hydrophobic Mismatch in Lipid Membrane Phase-Separation Kinetics. *Journal of the American Chemical Society*, 138(36):11633–11642, 2016.
- [56] Diego A. Pantano, Preston B. Moore, Michael L. Klein, and Dennis E. Discher. Raft registration across bilayers in a molecularly detailed model. *Soft Matter*, 7(18):8182–8191, 2011.

- [57] A. J. Verkleij, R. F.A. Zwaal, B. Roelofsen, P. Comfurius, D. Kastelijn, and L. L.M. van Deenen. The asymmetric distribution of phospholipids in the human red cell membrane. A combined study using phospholipases and freeze-etch electron microscopy. *BBA - Biomembranes*, 323(2):178–193, 1973.
- [58] J. H. Lorent, K. R. Levental, L. Ganesan, G. Rivera-Longsworth, E. Sezgin, M. Doktorova, E. Lyman, and I. Levental. Plasma membranes are asymmetric in lipid unsaturation, packing and protein shape. *Nature Chemical Biology*, 16:644–652, may 2020.
- [59] Roie Shlomovitz and M. Schick. Model of a raft in both leaves of an asymmetric lipid bilayer. *Biophysical Journal*, 105(6):1406–1413, 2013.
- [60] S. Leibler. Curvature instability in membranes. *Journal de Physique*, 47(3):507–516, 1986.
- [61] D. J. Keller, H. M. McConnell, and V. T. Moy. Theory of superstructures in lipid monolayer phase transitions. *The Journal of Physical Chemistry(R)*, 90(11):2311–2315, 1986.
- [62] D. J. Keller, J. P. Korb, and H. M. McConnell. Theory of shape transitions in two-dimensional phospholipid domains. *Journal of Physical Chemistry*, 91(25):6417–6422, 1987.
- [63] Harden M. McConnell and Vincent T. Moy. Shapes of finite two-dimensional lipid domains. *Journal of Physical Chemistry*, 92(15):4520–4525, 1988.
- [64] H M McConnell. Structures and Transitions in Lipid Monolayers at the Air-Water Interface. *Annual Review of Physical Chemistry*, 42(1):171–195, 1991.
- [65] Sarah L. Keller and Harden M. Mc Connell. Stripe phases in lipid monolayers near a miscibility critical point. *Physical Review Letters*, 82(7):1602–1605, 1999.
- [66] Steffen Härtel, María Laura Fanani, and Bruno Maggio. Shape transitions and lattice structuring of ceramide-enriched domains generated by sphingomyelinase in lipid monolayers. *Biophysical Journal*, 88(1):287–304, 2005.
- [67] A. Travesset. Effect of dipolar moments in domain sizes of lipid bilayers and monolayers. *Journal of Chemical Physics*, 125(8):084905, 2006.
- [68] Elena Rufeil-Fiori, Natalia Wilke, and Adolfo J. Banchio. Dipolar interactions between domains in lipid monolayers at the air-water interface. *Soft Matter*, 12(21):4769–4777, 2016.
- [69] Jonathan J. Amazon, Shih Lin Goh, and Gerald W. Feigenson. Competition between line tension and curvature stabilizes modulated phase patterns on the surface of giant unilamellar vesicles: A simulation study. *Physical Review E - Statistical, Nonlinear, and Soft Matter Physics*, 87(2):022708, 2013.

- [70] Jonathan J. Amazon and Gerald W. Feigenson. Lattice simulations of phase morphology on lipid bilayers: Renormalization, membrane shape, and electrostatic dipole interactions. *Physical Review E - Statistical, Nonlinear, and Soft Matter Physics*, 89(2):022702, 2014.
- [71] Jinglei Hu, Thomas Weikl, and Reinhard Lipowsky. Vesicles with multiple membrane domains. *Soft Matter*, 7(13):6092–6102, 2011.
- [72] Frederick A. Heberle, Drew Marquardt, Milka Doktorova, Barbara Geier, Robert F. Standaert, Peter Heftberger, Benjamin Kollmitzer, Jonathan D. Nickels, Robert A. Dick, Gerald W. Feigenson, John Katsaras, Erwin London, and Georg Pabst. Sub-nanometer Structure of an Asymmetric Model Membrane: Interleaflet Coupling Influences Domain Properties. *Langmuir*, 32(20):5195–5200, 2016.
- [73] Barbara Eicher, Drew Marquardt, Frederick A. Heberle, Ilse Letofsky-Papst, Gerald N. Rechberger, Marie Sousai Appavou, John Katsaras, and Georg Pabst. Intrinsic Curvature-Mediated Transbilayer Coupling in Asymmetric Lipid Vesicles. *Biophysical Journal*, 114(1):146–157, 2018.
- [74] P. B. Canham. The minimum energy of bending as a possible explanation of the biconcave shape of the human red blood cell. *Journal of Theoretical Biology*, 26(1):61–76, 1970.
- [75] W. Helfrich. Elastic Properties of Lipid Bilayers: Theory and Possible Experiments. *Zeitschrift fur Naturforschung - Section C Journal of Biosciences*, 28(11-12):693–703, 1973.
- [76] Aurelia R. Honerkamp-Smith, Pietro Cicuta, Marcus D. Collins, Sarah L. Veatch, Marcel Den Nijs, M. Schick, and Sarah L. Keller. Line tensions, correlation lengths, and critical exponents in lipid membranes near critical points. *Biophysical Journal*, 95(1):236–246, 2008.
- [77] Aurelia R. Honerkamp-Smith, Benjamin B. MacHta, and Sarah L. Keller. Experimental observations of dynamic critical phenomena in a lipid membrane. *Physical Review Letters*, 108(26), 2012.
- [78] Alexander J. Sodt, Michael Logan Sandar, Klaus Gawrisch, Richard W. Pastor, and Edward Lyman. The molecular structure of the liquid-ordered phase of lipid bilayers. *Journal of the American Chemical Society*, 136(2):725–732, 2014.
- [79] Benjamin Kollmitzer, Peter Heftberger, Michael Rappolt, and Georg Pabst. Monolayer spontaneous curvature of raft-forming membrane lipids. *Soft Matter*, 9(45):10877–10884, 2013.
- [80] Jeremy Pencer, Susan Krueger, Carl P. Adams, and John Katsaras. Method of separated form factors for polydisperse vesicles. *Journal of Applied Crystallography*, 39(3):293–303, 2006.

- [81] J. Pencer and F. R. Hallett. Small-angle neutron scattering from large unilamellar vesicles: An improved method for membrane thickness determination. *Physical Review E - Statistical Physics, Plasmas, Fluids, and Related Interdisciplinary Topics*, 61(3):3003–3008, 2000.
- [82] Karin A. Riske, Lia Q. Amaral, and M. Teresa Lamy-Freund. Thermal transitions of DMPG bilayers in aqueous solution: SAXS structural studies. *Biochimica et Biophysica Acta - Biomembranes*, 1511(2):297–308, 2001.
- [83] Herbert Schmiedel, Peter Jörchel, Mikael Kiselev, and Gotthard Klose. Determination of structural parameters and hydration of unilamellar POPC/C 12E 4 vesicles at high water excess from neutron scattering curves using a novel method of evaluation. *Journal of Physical Chemistry B*, 105(1):111–117, 2001.
- [84] M. C. Wiener and S. H. White. Structure of a fluid dioleoylphosphatidylcholine bilayer determined by joint refinement of x-ray and neutron diffraction data. III. Complete structure. *Biophysical Journal*, 61(2):434–447, 1992.
- [85] Georg Pabst, Richard Koschuch, Beatriz Pozo-Navas, Michael Rappolt, Karl Lohner, and Peter Laggner. Structural analysis of weakly ordered membrane stacks. *Journal of Applied Crystallography*, 36(6):1378–1388, 2003.
- [86] Michael R. Brzustowicz and Axel T. Brunger. X-ray scattering from unilamellar lipid vesicles. *Journal of Applied Crystallography*, 38(1):126–131, 2005.
- [87] Stephen J. Henderson. Monte Carlo modeling of small-angle scattering data from non-interacting homogeneous and heterogeneous particles in solution. *Biophysical Journal*, 70(4):1618–1627, 1996.
- [88] Frederick A. Heberle, Vinicius N.P. Anghel, and John Katsaras. Scattering from phase-separated vesicles. I. An analytical form factor for multiple static domains. *Journal of Applied Crystallography*, 48:1391–1404, 2015.
- [89] Giovanni Bussi, Davide Donadio, and Michele Parrinello. Canonical sampling through velocity rescaling. *Journal of Chemical Physics*, 126(1):014101, 2007.
- [90] Yifei Qi, Helgi I. Ingólfsson, Xi Cheng, Jumin Lee, Siewert J. Marrink, and Wonpil Im. CHARMM-GUI Martini Maker for Coarse-Grained Simulations with the Martini Force Field. *Journal of Chemical Theory and Computation*, 11(9):4486–4494, 2015.
- [91] Sunhwan Jo, Taehoon Kim, Vidyashankara G. Iyer, and Wonpil Im. CHARMM-GUI: A web-based graphical user interface for CHARMM. *Journal of Computational Chemistry*, 29(11):1859–1865, 2008.

- [92] H. Jelger Risselada, Alan E. Mark, and Siewert J. Marrink. Application of mean field boundary potentials in simulations of lipid vesicles. *Journal of Physical Chemistry B*, 112(25):7438–7447, 2008.
- [93] H. Jelger Risselada and Siewert J. Marrink. Curvature effects on lipid packing and dynamics in liposomes revealed by coarse grained molecular dynamics simulations. *Physical Chemistry Chemical Physics*, 11(12):2056–2067, 2009.
- [94] E. Kreyszig. *Differential Geometry*. Dover Publications Inc., New York, 1991.
- [95] M. Mert Terzi, Markus Deserno, and John F. Nagle. Mechanical properties of lipid bilayers: A note on the Poisson ratio. *Soft Matter*, 15(44):9085–9092, 2019.
- [96] K. Sapp, L. Maibaum, and A. J. Sodt. Simple differences in the protein-membrane attachment mechanism have functional consequences for surface mechanics. *Journal of Chemical Physics*, 151(16):164116, 2019.
- [97] Feng Feng and William S. Klug. Finite element modeling of lipid bilayer membranes. *Journal of Computational Physics*, 220(1):394–408, 2006.
- [98] Charles Loop. *Smooth Subdivision Surfaces Based on Triangles*. PhD thesis, 1987.
- [99] Fehmi Cirak, Michael Ortiz, and Peter Schröder. Subdivision surfaces: A new paradigm for thin-shell finite-element analysis. *International Journal for Numerical Methods in Engineering*, 47(12):2039–2072, 2000.
- [100] Felix Campelo, Harvey T. McMahon, and Michael M. Kozlov. The hydrophobic insertion mechanism of membrane curvature generation by proteins. *Biophysical Journal*, 95(5):2325–2339, 2008.
- [101] Richard M. Venable, Frank L.H. Brown, and Richard W. Pastor. Mechanical properties of lipid bilayers from molecular dynamics simulation. *Chemistry and Physics of Lipids*, 192:60–74, 2015.
- [102] Alexander J. Sodt and Richard W. Pastor. Bending free energy from simulation: Correspondence of planar and inverse hexagonal lipid phases. *Biophysical Journal*, 104(10):2202–2211, 2013.
- [103] S Leikin, M M Kozlov, N L Fuller, and R P Rand. Measured effects of diacylglycerol on structural and elastic properties of phospholipid membranes. *Biophysical journal*, 71(5):2623–2632, nov 1996.
- [104] Xin Wang and Markus Deserno. Determining the pivotal plane of fluid lipid membranes in simulations. *Journal of Chemical Physics*, 143(16):164109, 2015.
- [105] Xin Wang and Markus Deserno. Determining the lipid tilt modulus by simulating membrane buckles. *Journal of Physical Chemistry B*, 120(26):6061–6073, 2016.

- [106] Amirali Hossein and Markus Deserno. Spontaneous Curvature, Differential Stress, and Bending Modulus of Asymmetric Lipid Membranes. *Biophysical Journal*, 118(3):624–642, 2020.
- [107] Tim Bartels, Ravi S. Lankalapalli, Robert Bittman, Klaus Beyer, and Michael F. Brown. Raftlike mixtures of sphingomyelin and cholesterol investigated by solid-state ^2H NMR spectroscopy. *Journal of the American Chemical Society*, 130(44):14521–14532, 2008.
- [108] Ofer Kimchi, Sarah L. Veatch, and Benjamin B. Machta. Ion channels can be allosterically regulated by membrane domains near a de-mixing critical point. *Journal of General Physiology*, 2018.
- [109] Matthew B. Stone, Sarah A. Shelby, Marcos F. Núñez, Kathleen Wisser, and Sarah L. Veatch. Protein sorting by lipid phase-like domains supports emergent signaling function in b lymphocyte plasma membranes. *eLife*, 6, 2017.
- [110] Edward J. Shimshick and Harden M. McConnell. Lateral Phase Separation in Phospholipid Membranes. *Biochemistry*, 12(12):2351–2360, 1973.
- [111] Sarah L. Veatch and Sarah L. Keller. Organization in Lipid Membranes Containing Cholesterol. *Physical Review Letters*, 89(26), 2002.
- [112] Tobias Baumgart, Samuel T. Hess, and Watt W. Webb. Imaging coexisting fluid domains in biomembrane models coupling curvature and line tension. *Nature*, 425(6960):821–824, 2003.
- [113] Wade F. Zeno, Kaitlin E. Johnson, Darryl Y. Sasaki, Subhash H. Risbud, and Marjorie L. Longo. Dynamics of Crowding-Induced Mixing in Phase Separated Lipid Bilayers. *Journal of Physical Chemistry B*, 120(43):11180–11190, 2016.
- [114] S. Tristram-Nagle, R. Zhang, R. M. Suter, C. R. Worthington, W. J. Sun, and J. F. Nagle. Measurement of chain tilt angle in fully hydrated bilayers of gel phase lecithins. *Biophysical Journal*, 1993.
- [115] Sayan Mondal, George Khelashvili, and Harel Weinstein. Not just an oil slick: How the energetics of protein-membrane interactions impacts the function and organization of transmembrane proteins. *Biophysical Journal*, 106(11):2305–2316, 2014.
- [116] Jianbing Zhang, Honghua Cao, Bingwen Jing, Paulo F. Almeida, and Steven L. Regen. Cholesterol-phospholipid association in fluid bilayers: A thermodynamic analysis from nearest-neighbor recognition measurements. *Biophysical Journal*, 91(4):1402–1406, 2006.

- [117] Daniel Huster, Klaus Arnold, and Klaus Gawrisch. Investigation of lipid organization in biological membranes by two-dimensional nuclear overhauser enhancement spectroscopy. *Journal of Physical Chemistry B*, 103(1):243–251, 1999.
- [118] Maitane Ibarguren, Alicia Alonso, Boris G. Tenchov, and Felix M. Goñi. Quantitation of cholesterol incorporation into extruded lipid bilayers. *Biochimica et Biophysica Acta - Biomembranes*, 1798(9):1735–1738, 2010.